The Dissertation Committee for Cong Liu Certifies that this is the approved version of the following dissertation:

SINGLE-MOLECULE TRACKING AND ITS APPLICATION IN BIOMOLECULAR BINDING DETECTION

Committee:

Hsin-Chih Yeh, Supervisor

Andrew Dunn

Jeanne Stachowiak

R. Malcolm Brown

Yaguo Wang

SINGLE-MOLECULE TRACKING AND ITS APPLICATION IN BIOMOLECULAR BINDING DETECTION

by

Cong Liu, B.E.

Dissertation

Presented to the Faculty of the Graduate School of

The University of Texas at Austin

in Partial Fulfillment

of the Requirements

for the Degree of

Doctor of Philosophy

The University of Texas at Austin

May 2017

Acknowledgements

There is a long list of people whom I am grateful to, but this section is only dedicated to those who may actually read the following paragraphs. My acknowledgments will not make any difference to the others anyway.

I would like to thank the 2012 BME PhD students recruitment committee. They picked up my resume from tons of applications, and gave me an interview and an offer during the Spring Festival.

Tim Yeh has been an amazing adviser in many aspects. He has made an excellent demonstration of “how to survive as an assistant professor in a top 15 engineering school”. He sets a benchmark for any future students who want to pursue an academic career. He is always enthusiastic about new ideas and supportive of my exploratory (often a synonym for doomed-to-fail) experiments.

I feel very fortunate to have Allen Liu, Yu-An Chen, and Judy Obliosca as lab mates. Allen and Judy taught me a lot of basic biology and wet lab practices. Yu-An and Judy taught me how to troubleshoot the DNA related problems. They genuinely care about each other and are willing to help whenever I need it.

In the end, I would like to thank our collaborators – Prof. Andrew Dunn and Prof. Jeanne Stachowiak, and the graduate students in their labs who have helped me in the experiments: Evan, Avi, Wilton and Zach. I would also like to thank Amy and Chengyi (Dr. Zoldan lab).

Single-molecule tracking and its application in biomolecular binding detection

Cong Liu, PhD

The University of Texas at Austin, 2017

Supervisor: Hsin-Chih Yeh

In the past two decades significant advances have been made in single-molecule detection, which enables the direct observation of single biomolecules at work in real time under physiological conditions. In particular, the development of single-molecule tracking (SMT) microscopy allows us to monitor the motion paths of individual biomolecules in living systems, unveiling the localization dynamics and transport modalities of the biomolecules that support the development of life. While 3D-SMT is probably the most suitable method for determining whether tracked molecules (can be any biomolecule such as DNA, membrane receptors, and transcription factors) form dimers or complexes with other molecules, great technical challenges remain to be overcome before the potential of 3D-SMT in biomolecular binding detection can be realized. This dissertation describes my work on recent methodology development to overcome these challenges, and new applications of the 3D-SMT technology in rare molecular species quantification.

First, we provide an overview of current SMT technologies, with an emphasis on three-dimensional feedback controlled SMT. Advantages and drawbacks of each SMT method are outlined.

Second, we describe the theoretical modeling and instrumentation of our confocal tracking microscope. Its multi-dimensional sensing capability (3D position, diffusion

coefficient, fluorescence lifetime) is experimentally characterized. In order to maximize the tracking duration, we have also developed strategies to effectively slow-down fast diffusing molecule, and optimized the buffer conditions.

Third, we show that our 3D-SMT microscope can detect biomolecular association/disassociated by two types of contrast mechanisms: diffusion rate and lifetime FRET signal. DNA transient binding is used as a model system because of ease of fluorescent labeling and tunable binding kinetics. Both of the two mechanisms involve tracking a fluorescent-labeled single-stranded DNA (ssDNA), but the second approach also requires its complementary strand to be labeled by a dark quencher. A combined analysis of multiple single-molecule trajectories allow us to measure the kinetics that is even beyond the physical bandwidth of the tracking system.

In the end, we introduce the application of SMT in rare single-molecule species quantification. The theory for predicting the sensitivity and fidelity is established. Our work highlights the fundamental limitations that we are facing in precise single-molecule identification and quantification without amplification.

Table of Contents

List of Tables

List of Figures

Chapter 1: Introduction

1.1 Overview of single-molecule tracking techniques

Single-molecule detection has revolutionized the way we study biological systems. It allows us to see stochastic processes or minor reaction pathways that would otherwise be masked in ensemble measurements. The direct observation of individual biomolecules has shed light on the most fundamental molecular processes, including enzymatic turnovers[1-2], gene expression[3-4], protein folding[5-6], ligand-receptor interaction[7-8], and virus infection[9-10]. In particular, single-molecule detections have successfully unveiled intermediates during protein folding[11] and subpopulations of molecules in a mixture[12], which could not be observed by conventional ensemble measurement techniques.

The key to single-molecule detection lies in an extremely small detection volume. This is due to the fact that the signal-to-background ratio (SBR) is significantly improved when the detection volume is less than one femtoliter[13]. Two original techniques that provide small detection volumes for single-molecule detection are confocal and total-internal-reflection fluorescence (TIRF) microscopy. Having an effective detection volume about 0.2 femtoliter[14], confocal microscopy detects one molecule at a time as the molecule is flowing through or diffusing in-and-out of the detection volume in an aqueous solution, generating burst signals in the single-photon-counting devices. Such photon bursts can be analyzed for their intensity[15], spectrum[16], anisotropy[17], and fluorescence lifetime[18], thereby providing information on molecular size, conformation, and stoichiometry. However, as the average time for a diffusive molecule to traverse the detection volume of a confocal system is on the order of 1 ms, the resulting short burst signals cannot describe any underlying slow dynamic processes. Besides, the data throughput is low (one molecule at a time). TIRF microscopy, on the other hand, offers a higher data throughput by employing a wide-field illumination scheme, thus hundreds of single molecules can be imaged at the

same time. But due to the shallow penetration depth of evanescent wave field (~150 nm), single molecules have to be tethered to the surface for observation. Although the observation time of single molecules can be as long as minutes (only limited by photobleaching[19-20]), immobilization is not a physiologically relevant condition. Perturbation caused by surface interaction can lead to artifacts in single-molecule measurements[21]. TIRF is particularly useful for the cell-free, in vitro observation of single-molecule behaviors on surface. For instance, conformation change of enzymes[22] and Holiday junction structure dynamics[23] have been well characterized by TIRF microscopy at the single-molecule level.

Unlike the traditional single-molecule detection methods described above, single-molecule tracking (SMT), or single particle tracking (SPT) techniques, allow researchers to follow the molecules of interest and record their motion paths. The 1st generation SMT methods are simply based on TIRF, with the additional capability to perform frame-by-frame video analysis. Single-molecule trajectories are obtained through the identification of the same single molecules in each frame and the calculation of displacements of these molecules in consecutive frames. While this frame-by-frame analysis can certainly reveal the 2D motion patterns of single molecules within the evanescent wave field[24-27], the 1st generation tracking methods can only investigate in vitro processes[28] or cellular processes on the membrane[29]. Besides, whenever the frame-by-frame analysis is used for trajectory analysis, the temporal resolution is defined by the camera's frame rate.

To be able to track hundreds of single molecules at a time in mammalian cells, a thin optical sectioning plane that can go tens of microns into specimens is required. Two methods to generate a thin optical sectioning plane are pseudo TIRF (HILO[30]) and light sheet microscopy[31], which we collectively term the 2nd generation SMT methods. Whereas the 2nd generation methods enable the investigation of single-molecule trajectories inside

mammalian cells, they are still 2D tracking techniques. In other words, the 2nd generation methods require a time-consuming z-scan to observe molecular motion in the third dimension inside a mammalian cell[32].

Generation	Design	Feature	References
1st	TIRF and image-based tracking, non-feedback	2D, only can track single molecules on cellular membranes or in *in-vitro* systems	22-23, 26, 33-35
2nd	Light-sheet microscopy and image-based tracking, non-feedback	Can track single molecules in mammalian cells, but requires a time-consuming z-scan to build 3D trajectories	4, 31, 36-43
3rd	3D, z-position encoded in the 2D image, non-feedback	Enable z-position characterization within the imaging depth of objective (~±1 μm)	44-49
4th	Feedback-control 3D tracking microscopy	Enable high-resolution 3D tracking and a large z-tracking range. Can measure fluorescence lifetime. Multiple detectors often required.	50-61
5th	Feedback-control, multicolor and deep 3D tracking microscopy	Use one detector. Image depth up to 200 μm. Easy for multicolor detection.	62-64

Table 1: Overview of SMT Techniques

To track single molecules directly in the 3D space without any optical scanning, the 3rd generation tracking methods have been proposed that can encode the z-position of the single molecules in their 2D images. The most straightforward way to do this is to create multiple imaging planes (*e.g.* using multiple cameras) and estimate the z-position based on the out-of-focus spot size at each imaging plane[65-66]. Alternatively, the z-position can be encoded as the shape of the out-of-focus spot by taking advantage of astigmatism, where only one camera is needed[67]. The most notable effort in the development of 3rd generation tracking methods is the point-spread-function (PSF) engineering, in which the

single emitter no longer appears as a single round spot at the imaging plane. For instance, a single emitter can appear as two spots in the double-helix PSF microscopy, in which the z-position of the emitter is derived from the orientation and the separation distance of the two resulting PSF spots[68].

From the 1st to the 3rd generation methods, the detection volume is either fixed or is passively scanned. If the molecules of interest diffuse far away from the detection volume, they are lost and their recorded trajectories terminate. In the 4th generation tracking methods, microscopes were designed to actively track a single emitter[54]. In fact Howard C. Berg first described a feedback-control system to track the motion of single bacteria in solution in 1971[69]. The key idea behind feedback tracking is to employ an actuation mechanism that can keep the diffusing singe molecule in the center of the focused beam. This can be done by either constantly bringing the diffusing molecule back to the center of the focused laser beam (*i.e.* via moving the whole sample using a xyz piezo stage) or steering the laser beam to lock on the diffusing molecule. Trajectories of the tracked particles are thus plotted based on the motion history of the piezo stage or the galvo mirrors[54]. At first glance the 4th generation feedback tracking methods share similarities with the particle trapping methods (*e.g.* optical tweezers[70] and electrophoretic trap[71-72]) in that they both try to keep the molecule of interest in the center of laser focus for long-term observation. But practically they are different techniques: in the 4th generation tracking methods the molecule of interest is free to diffuse in the 3D space, while in particle trapping methods the molecule is captured and spatially confined. As a result, optical traps cannot be used to monitor the native movements of single biomolecules inside live cells. We call the 1st, 2nd and 3rd generation tracking microscopes non-feedback SMT systems, and the 4th generation tracking microscopes and later development the feedback SMT systems.

Although the non-feedback SMT microscopy shares similarities with single-molecule-based super-resolution microscopy[73] (PALM[74], STORM[75] and their variants[76-77]) in design concepts and instrumentation, the non-feedback systems need additional efforts to establish correspondence between molecules in consecutive image frames[78]. Establishing unambiguous molecular correspondence is not straightforward and can be complicated by a number of factors (*e.g.* high molecular density and disappearance of molecules over time). Recently Saxton and others initiated the first community experiment comparing the performance of analysis methods for SMT data[79]. Whereas no single method performed best across all scenarios, the results revealed clear differences between the various approaches of which users of these tracking analysis methods should be aware [79-82].

One of the key differences between the non-feedback and the feedback tracking systems lies in that the latter can be built based on single-pixel, single-photon-counting detectors, for instance APD (avalanche photodiode) and PMT (photomultiplier tubes), rather than cameras[50-51]. The use of single-pixel detectors for SMT not only drastically improves the temporal resolution but also allows additional information, for instance fluorescence lifetime, to be simultaneously acquired while tracking the particle. Although the capability to perform time-correlated single-photon counting (TCSPC) analysis while tracking the molecules can provide information beyond the motion paths of the tracked molecules, the data throughput of the feedback systems is low as only one molecule is actively tracked at a time.

1.2 NON-FEEDBACK TRACKING MICROSCOPES

As mentioned in the previous section, the key to successful single-molecule detection lies in a sufficient SBR. Here background refers to out-of-focus fluorescence,

fluorescent impurities, Rayleigh scattering (elastic scattering) and Raman scattering (inelastic scattering)[13]. An effective way to suppress the background is to use TIRF (the 1st generation SMT systems), where the decay length of evanescent wave generated by total internal reflection is about 150 nm. In other words, only the molecules within this decay length can be illuminated and imaged. Microscopes equipped with high-N.A. (> 1.4) objectives are the most commonly adopted TIRF configurations which allow for easy switching between TIRF and the standard epi-fluorescence imaging mode (Figure 1 1(a) left). Whereas the shallow illumination depth of TIRF reduces background signals and also minimizes premature photobleaching, TIRF is not suitable for tracking molecules inside mammalian cells. Therefore, researchers mainly used TIRF for tracking molecules on cell membranes[7, 35, 83-85] or inside bacteria[86]. To bring intracellular molecules (*e.g.* spliceosome in mammalian nucleus) into the evanescent field of TIRF, whole cell extract has been used [87-89].

1.2.1 Selective plane illumination microscopy

To accommodate SMT inside mammalian cells, highly inclined thin illumination optical sheet (HILO) microscopy[30] and advanced light-sheet microscopy (LSM)[43, 90] were developed (the 2nd generation SMT systems). In HILO microscopy (Fig. 1(a)), the lateral position of the incident laser beam is somewhere in between the TIRF mode and the epifluorescence mode, allowing an inclined and laminated light sheet to penetrate into specimen[30]. The incident angle (ϕ) of the laser beam needs to be carefully adjusted in order to compensate the spherical aberration caused by the refractive index mismatch between the specimen and the coverslip[91-92]. Besides, the reduction of the light-sheet thickness is accompanied by the decrease of the illumination area ($dz = R/\tan\theta$, Figure 1(a) right panel). Moreover, HILO also suffers from fringing and shading artifacts[93]. Although out-

of-focus fluorescence excitation due to the inclined nature of the illumination laser beam reduces SBR in detection[94], HILO microscopy has been used to track the active cargo transport along microtubules[39] and study surface dynamics of embryo with 200 nm-thick eggshell[41].

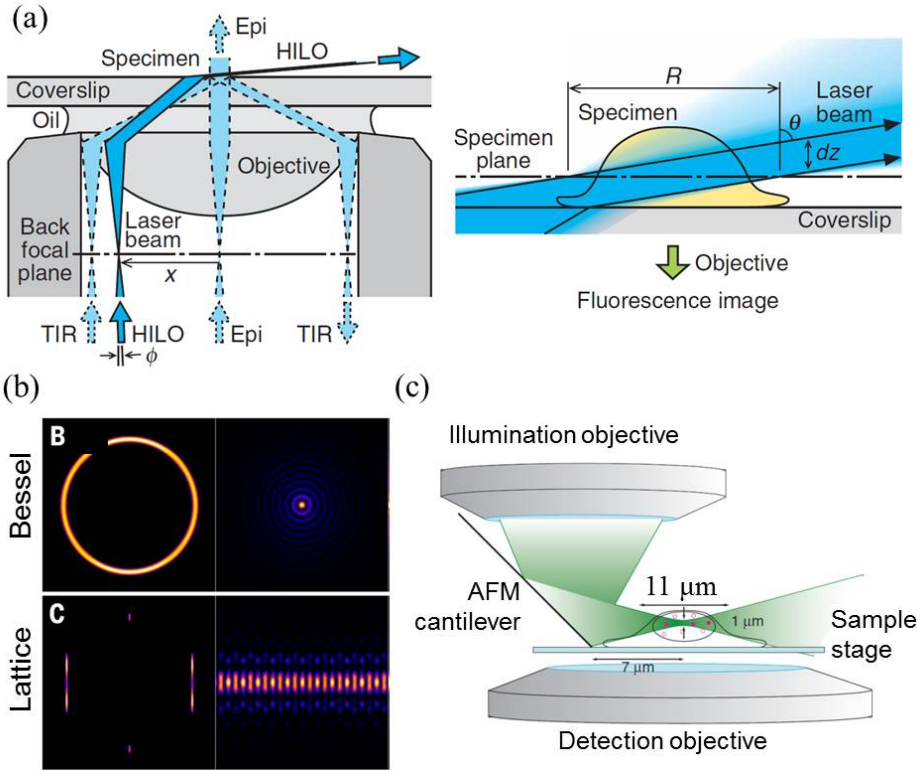

Figure 1. Generation of thin illumination field (**a**) Highly inclined thin illumination optical sheet (HILO) microscopy[30]. The incident beam is highly inclined and laminated as a thin light sheet in the specimen. TIR: totally internal reflection; Epi: epifluorescence. (**b**) Bessel beam and lattice light-sheeting microscopy[90]. Left column: the intensity pattern at the rear pupil plane of the excitation objective. Right column: the cross-sectional intensity of the pattern in the xy plane at the focus of the excitation objective. (**c**) Reflected light sheet microscopy (RLSM)[94]. A disposable mirror reflects the light sheet into a horizontal plane close to the sample surface. Because of the shape of the light sheet, a small gap between the surface and the light sheet cannot be illuminated.

Other than HILO microscopy, advanced LSM provides an optical sectioning plane thin enough for SMT. The light sheet can be generated either by focusing the excitation laser one dimensionally using a cylindrical lens[38, 42, 95-98], or by scanning a long Gaussian beam across a plane[36, 99-101]. In both schemes, there is a fundamental trade-off between the length and thickness of the light sheet due to the diffraction: the depth of focus ($2z_0$) of Gaussian beam (which decides the length of the light sheet) is directly proportional to the square of beam waist radius (W_0), $2z_0=2\pi W_0^2/\lambda_{\mathrm{exc}}$[102], which decides the thickness of the light sheet.

To overcome this trade-off, Betzig's group turned to the Bessel-beam illumination and built the Bessel-beam light sheet microscopy (Bessel LSM)[31, 43]. An ideal Bessel beam is diffraction free; it propagates indefinitely without change in cross-sectional intensity profile. In the implementation, a Bessel beam (actually a Bessel-Gaussian beam) is created by projecting an annular illumination pattern at the rear pupil of the excitation objective (Figure 1(b)). The key advantage of the Bessel beam lies in that the thickness of the generated light sheet can be decoupled from the length of the light sheet. Consequently, the Bessel LSM provides a field of view as large as 50 μm×50 μm with the illumination plane thickness as small as 500 nm, as compared to the 2–10 μm sheet thickness in the traditional Gaussian LSM[31]. Unfortunately, substantial energy of the Bessel beam resides in side lobes that surround the center peak, which excites the out-of-focus molecules and deteriorates the axial resolution.

A promising platform that eliminates the side-lobe issue and offers further gains in SBR is the lattice light sheet microscopy (lattice LSM)[90]. Optical lattice are periodic interference patterns (Figure 1(b)) created by the coherent superposition of a finite number of plane waves. Like an ideal Bessel beam, an ideal 2D optical lattice is non-diffracting. In the implementation, the 2D lattice is generated by a spatial light modulator that is

conjugated to the back focal plane of the objective. The high speed dithering of the lattice enabled by galvo mirrors creates a uniform light sheet. Without any side-lobe excitation, lattice LSM delivers a much lower peak intensity to the specimen than the conventional Gaussian/Bessel LSM (although total light dose delivered is similar), which is critical for cell health during the imaging[103]. The resolution of lattice LSM is comparable to that of a confocal microscope, but the recording speed and imaging duration are significantly improved[104].

One problem in LSM is the spatial constraints imposed by the two orthogonally arranged objectives—it is difficult to position the light sheet within 10 μm from the sample surface[94], making selective illumination of typical mammalian cell nuclei challenging. To overcome this limitation, reflected light sheet microscopy (RLSM)[94] and single-objective LSM[105] have been developed, which use a 45° micromirror or an atomic force microscopy cantilever to turn the vertical light sheet into the horizontal light sheet (Figure 1(c)). Using RLSM, Xie's group has tracked individual transcription factor GR (glucocorticoid receptor) in MCF-7 cells and observed their binding to DNA in nuclei[94].

The superior optical sectioning capabilities of TIRF, HILO and advanced LSM make them ideal for 2D single-molecule imaging and tracking. However, without a z-scan these tools cannot provide information about the molecule's axial movement. Considering that most intracellular are inherently three dimensional, a true 3D SMT technique is highly desired.

1.2.2 Multifocus microscopy

One way to achieve 3D SMT is through multifocal plane imaging[65-66, 106-108]. Recently, a multifocus microscopy (MFM) that can produce an instant focal stack of nine images on a single camera has been reported[109]. In this scheme, a specially designed

diffractive grating splits and shifts the focus of the sample emission light to form an instant focal series. Due to its fast 3D imaging capability, MFM has been used to study transcription dynamics[110-111], gene editing[112] and other cell biology processes[113-114].

1.2.3 Microscopes with engineered point spread function

An alternative approach to achieve 3D SMT is to encode molecule's z position in the microscope's 2D image. This can be done by an approach termed point-spread-function (PSF) engineering, where the PSF of the microscope is modified by using additional optical components (cylindrical lens, prism, spatial light modulator) in the detection path. After modification, the PSF is no longer symmetrical with respect to the focal plane[115] and the molecule's z position can be discerned from the asymmetric PSF with a position uncertainty even smaller than the diffraction limit of light[67].

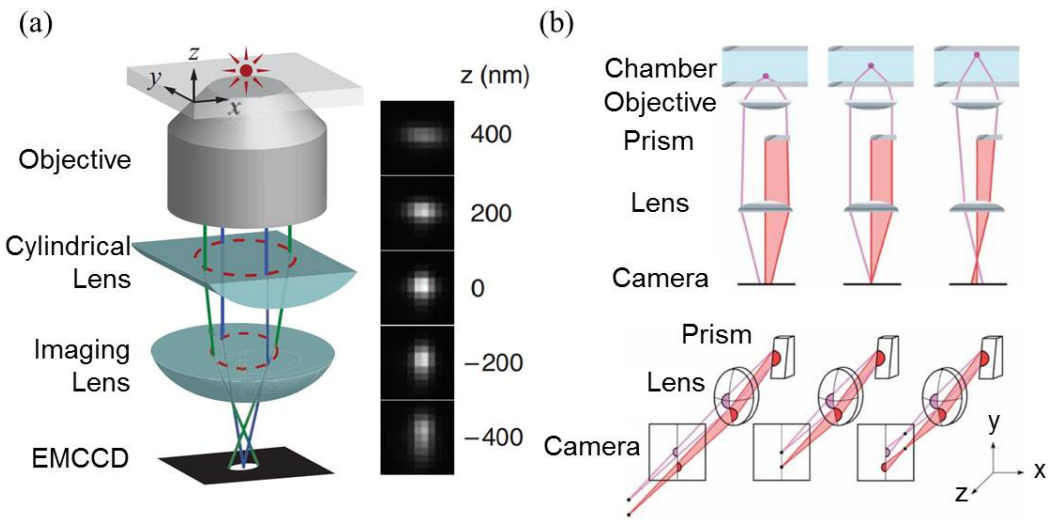

Figure 2. Point-spread-function engineering without spatial light modulator (**a**) Astigmatism imaging[67]: a cylindrical lens is inserted into the imaging path to render the image of each molecule elliptical. The ellipticity and orientation of a fluorophore's image varies as its position changes in z. (**b**) 3D tracking using a prism[45]: when the fluorescent molecule moves upward, the two beams of light split by the prism move symmetrically in opposite directions on the image.

Astigmatism imaging is the simplest and perhaps the earliest example of PSF engineering for 3D SMT[44]. It is easy to implement and the working principle is applicable to various types of microscopies (*e.g.* wide-field microscopy[106, 116], LSM[37, 117], and temporal focusing multiphoton excitation microscopy[118]). In astigmatism imaging, a weak cylindrical lens (another option is deformable mirror[119]) is inserted to the detection path, creating two slightly different focal planes for the x and y direction (Figure 2(a)). As a result, images of fluorescent molecules are circular in the average focal plane (approximately halfway between the x and y focal planes) but ellipsoidal below or above the average focal plane. The centroid and ellipticity of the image are then used to determine the lateral (x and y) and axial (z) coordinates of the molecule respectively[120].

Another simple method to encode the z position in the fluorescent image is to place a wedge prism at the back focal plane of the objective (Figure 2(b))[45]. The fluorescence collected by the objective is split in two beams by the prism. The left half-beam (filled purple) passes through the center of the lens, whereas the right half-beam (filled red) refracted by the prism passes below the center. Thus molecule's z movement is converted to x movement at the image plane, where molecule's z position is reported by the x-separation of the two split images.

Comparing to cylindrical lens and prism, spatial light modulators (SLM) provide much more flexibility in PSF engineering and more control over the optical aberrations that affect localization accuracy. A SLM is a liquid crystal based device that can modulate

the phase, amplitude, or polarization of incident light as needed, but in SMT typically a phase-only SLM is used. Examples of PSF engineering using SLM for 3D SMT include double-helix PSF (DH-PSF)[46-47], tetrapod PSF[48], self-bending PSF (SB-PSF)[49], corkscrew PSF[121], and bisected pupil PSF[122]. Due to their intrinsic similarity, only the first two techniques are discussed below.

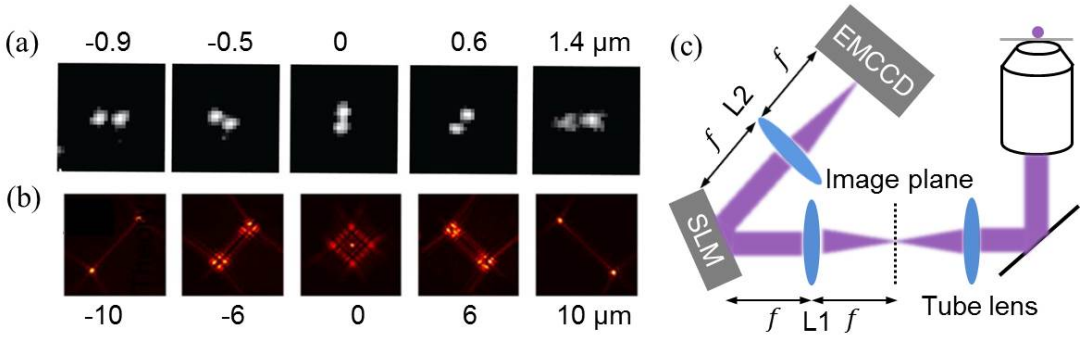

Figure 3. Point-spread-function engineering with a spatial light modulator (**a**) Images of a fluorescent bead at various axial positions in double helix PSF imaging[68] (**b**) Images of a fluorescent bead at various axial positions in tetrapod PSF imaging (**c**) Optical path of the single-molecule double-helix or tetrapod PSF setup.

The DH-PSF imaging system consists of a conventional inverted microscope and a 4*f* optical signal processing system as shown in Figure 3(c). Specifically, the objective lens and tube lens form an image of the sample at an intermediate plane. The lens L1 placed at a distance *f* from this intermediate plane produces the Fourier transform of the image at a distance *f* behind the lens. The Fourier transform is then phased-modulated by reflection from the LSM, and Fourier-transformed again by a second lens L2 (at a distance *f* to the SLM) onto the EMCCD to restore a real-space image[123]. As a consequence, a fluorescent molecule appears at the image plane as two lobs, and the two lobs have a unique orientation depending on the z-position of the molecule (Figure 3(a)). The xy position of the molecule is estimated from the midpoint of the line connecting the two lobs, and z position is

estimated from the angular orientation of the two lobs. Noticing that the failure to account for the molecule's transition dipole orientation can lead to significant lateral mislocalizations (up to 50–200 nm), the relative intensity of the two lobs is used as an additional parameter to determine the orientation of single-molecule emitter, which in turn can be utilized to correct the lateral localization[124].

In DH-PSF imaging, the depth over which one can determine the position of the molecules is only about 2 μm, posing a major limitation for applications requiring deep imaging and large-axial-range tracking. This limitation can be overcome by a tetrapod PSF design (Figure 3(b)) which shares the same optical implementation with DH-PSF but provides a z-range up to 20 μm. However, as PSF becomes more complex, the molecules in each image will need to be separated by greater distance for individual spots to be identified. Notably, Moerner's group has demonstrated a general method for PSF design that produces information-maximal PSF subject to system conditions (SBR, magnification and pixel size)[125]. Tetrapod PSF is just one solution to the optimization problem formulated in their work.

While engineered PSFs enable direct 3D tracking in the non-feedback systems, these 3rd generation tracking techniques require sophisticated calibration to accommodate factors that can distort the fluorescence images, such as emitter orientation, stage drift, the variation of localization accuracy across the field of view, and spherical aberration[46, 49, 124, 126]. It is this complexity and difficulty in implementation (especially the phase modulation of fluorescence wavefront) that prevents the widespread use of the 3rd generation tracking methods at this moment. In fact, the conventional epifluorescence microscopy[127-128], TIRF[28-29], HILO[129] and LSM[90, 94] are the dominant techniques today to investigate the 3D cellular processes at the single-molecule level.

1.3 FEEDBACK TRACKING MICROSCOPES

Feedback tracking systems have three major advantages over the non-feedback systems. First, the axial tracking range is no longer limited by the imaging depth of the objective (typically ± 1 μm), but rather by the travel range of piezo stage (± 15 μm). Second, there is no need for complicated PSF calibration as required in some 3rd generation tracking methods. Third, fluorescence lifetime of the tracer can be monitored simultaneously with its 3D position—thanks to the single-photon-counting detectors and TCSPC analysis.

1.3.1 Circularly scanning laser tracking

One of the first 3D feedback SMT designs is the circularly scanning laser tracking (orbital tracking). To illustrate its working principle, here we assume that the molecule moves in a 2D plane. In this scheme, the laser beam is circularly scanned (enabled by acousto-optic modulators[52] or resonant beam deflectors[59]) at the frequency ω_{xy}. When the molecule is right at the center of the scanning circle (Figure 4(a)), there's no signal intensity fluctuation during a scanning cycle. However, when the molecule deviates from the center, a sinusoidal variation of the signal over time can be observed. Therefore the molecule's lateral position can be derived from the magnitude and phase of this sinusoidal fluorescence signal[55]. To obtain the molecule's axial position, two laser beams are required. They rotate at the same frequency ω_{xy} and are focused at different depths (separated by ~1 μm) inside the sample (Figure 4(b)). More importantly, the optical powers in the beams are modulated 180° out-of-phase at the frequency ω_z (Figure 4(b)), thus allowing the molecule's axial position to be encoded in the ω_z frequency component of the fluorescence signal. Once the molecule's 3D position is determined, a piezo stage is used to bring the molecule back to the center of scanning circle. Thus the stage position represents the single-molecule position over time.

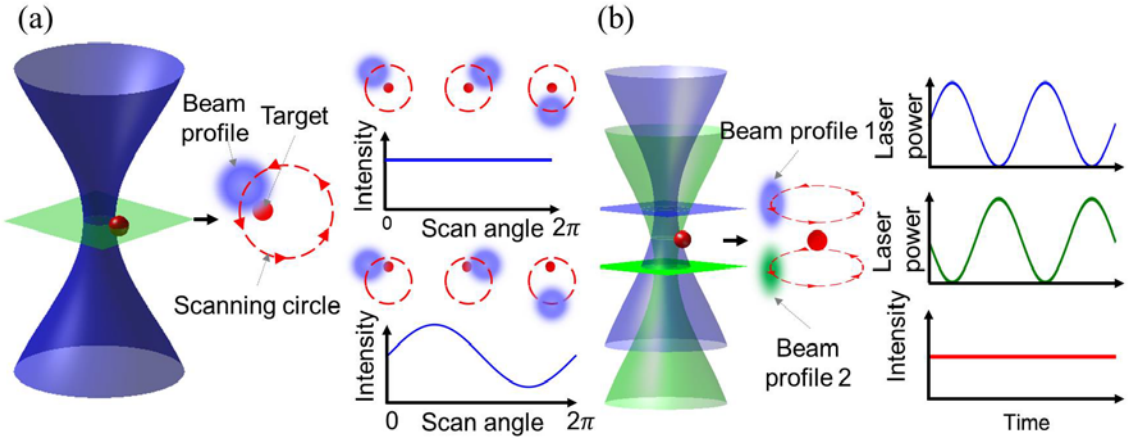

Figure 4. Circularly scanning laser tracking (**a**) Lateral position sensing[55]. The excitation laser scans circularly around the molecule. If the molecule is right at the center of the scanning circle, the fluorescence intensity remains constant during a scanning cycle (upper inset). If the molecule deviates a little from the center, the fluorescence intensity will exhibit modulation (lower inset). (**b**) Axial position sensing[55]. Two laser beams rotating at the same frequency are focused at different depths inside the sample.

The orbital tracking scheme works only when molecular motion is substantially small during each position estimation cycle (*i.e.* feedback bandwidth). To acquire fast dynamic information of the molecule whose motion is comparable to the system bandwidth, fluorescence correlation analysis similar to the fluorescence correlation spectroscopy (FCS) can be performed[59]. However, the combination of SMT and FCS does not increase the physical bandwidth, and the theory can only be applied to molecules undergoing isotropic Brownian diffusion. In other words, molecular motions such as active transport and sub-diffusion[130] are not accounted for using this hybrid analysis. Mabuchi's group has described a model of tracking error as a function of photon shot noise and molecule's diffusion coefficient[60, 131]. But again this model is only applicable to the free diffusion case. The original 3D orbital tracking system built by Gratton's group actually employed a two photon excitation source, which gives a higher SBR and suppresses the out-of-focus photobleaching[57-58]. Recently his group replaced the objective piezo with an

electrically tunable lens, which provides not only a much longer axial tracking range (500 μm) but also a shorter step response time (2.5 ms)[132].

1.3.2 Confocal tracking

In the orbital tracking approach, the molecular position is encoded by modulating the spatial distribution of laser intensity, which takes place in the sample space. One can also encode the molecular position in the image space. This idea was first proposed by Howard C. Berg for tracking bacterial (scattering signal is detected)[69] in 1971. But it wasn't until three decades later that tracking fluorescent nanoparticles or molecules became possible with this scheme, achieved separately by Yang's group[61, 133] and Werner's group[54, 106]. Their approaches are denoted as 3D confocal tracking here, since both of them utilized the spatial filtering effect typically seen in the confocal detection.

In Yang's approach, a pinhole is placed at the focus of the tube lens, but slightly axially offset (Figure 5(a) left). The fluorescence intensity through the pinhole will change as the molecule moves axially, thereby providing the z-position information. To detect the molecule's lateral position, the fluorescence emission is projected onto the ridges of two orthogonal prism mirrors, which split the signal to the two single-photon detectors (Figure 5(a) right). When the molecule is centered, the detectors receive the same amount of photons. When the molecule moves laterally, the photon count difference between the detectors will vary accordingly. The signals from the five detectors (one for z-position, two for x- and two for y-position) are fed to the controller, which sends a command to the xyz piezo-stage to bring the molecule back to the laser focus center for tracking. By combining the confocal tracking with the two-photon scanning microscopy, Yang's group has recently monitored cellular uptake of peptide-coated nanoparticles with a wide range of spatial and temporal resolutions[51].

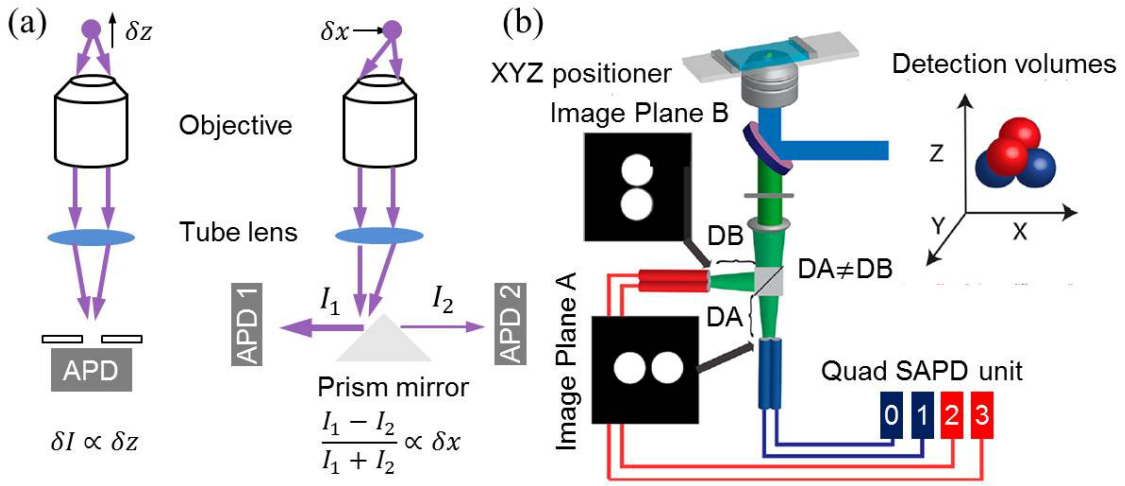

Figure 5. Confocal-feeback tracking (**a**) Confocal tracking developed by Yang's group[133]: Part of the emission light collected by the objective lens is focused onto a pinhole. The intensity throughput provides a measure of molecular z position. To detect the molecular lateral position, the image of the molecule is projected onto the ridges of two orthogonal placed prism mirrors. (**b**) Confocal tracking developed by Werner's group[134]: Two pairs of optical fibers are orthogonally installed. Each fiber is connected to an avalanche photodiode. The input face of each fiber serves as a pinhole, have a corresponding detection volume in the sample space (colored balls). One pair of fibers is axially separated from the other pair, so that the four detection volumes form a tetrahedron in the sample space.

Instead of using five detectors to achieve 3D confocal tracking, Werner's group used only four detectors. In Werner's approach (Figure 5(b)), the emission is split into two beams, and each beam is focused onto the center of a custom-made fiber bundle that consists of two multimode optical fibers. Each fiber serves as a spatial filter for the avalanche photodiode (APD) connected to it. The two fiber bundles are orthogonally orientated and axially offset. The resulting detection volumes form a tetrahedral geometry in the sample space (Figure 5(b) inset). A fluorescent molecule right in the center of the detection tetrahedron will give equal photon counts in the four detectors, while any displacement from the center will lead to asymmetric photon count distribution. This asymmetry, known as error signal, forms the basis for a feedback loop that drives the xyz

piezo-stage to reposition the molecule to the center of the detection tetrahedron. Taking advantage of the single-photon detectors, Werner's group has demonstrated lifetime measurement[50], photon-pair correlation analysis (*i.e.* antibunching)[135] and time-gated detection[136] (beneficial for SMT in high background environment, *e.g.*, inside a cell) together with 3D SMT, which are not possible with camera-based tracking.

Confocal tracking has two advantages over orbital tracking. First, confocal tracking has a better SBR since the laser beam is locked directly on the molecule for tracking, rather than having a small offset from the molecule. Second, confocal tracking can achieve a higher temporal resolution because it does not require laser scanning to build up an intensity time trace for position estimation.

1.3.3 TSUNAMI

Recently Dunn's group demonstrated a 3D tracking microscope, termed TSUNAMI (Tracking of Single particles Using Nonlinear And Multiplexed Illumination), that only requires one detector (a photomultiplier) to achieve 3D SMT[62, 64]. This approach is based on passive pulse splitters used for nonlinear microscopy. TSUNAMI discerns the 3D position of a molecule through spatiotemporally multiplexed two-photon excitation and temporally demultiplexed detection. In TSUNAMI, multiplexed illumination is realized by splitting the pulsed laser from a 76 MHz Ti-sapphire oscillator into four beams, with each beam delayed by 3.3 ns (one fourth of the laser repetition period) relative to its preceding one. These beams are focused through a high N.A. objective at slightly offset xyz positions. The four resulting two-photon excitation volumes are arranged in a tetrahedral geometry, in a way similar to the detection volume arrangement in Werner's 3D confocal tracking system. The four excitation volumes receive laser pulses at different time frames. With TCSPC analysis, each detected photon is assigned to a 3.3 ns–wide time gate (G1-G4 in

the fluorescence decay histogram, Figure 6(b)), and thus can be attributed to a specific excitation volume.

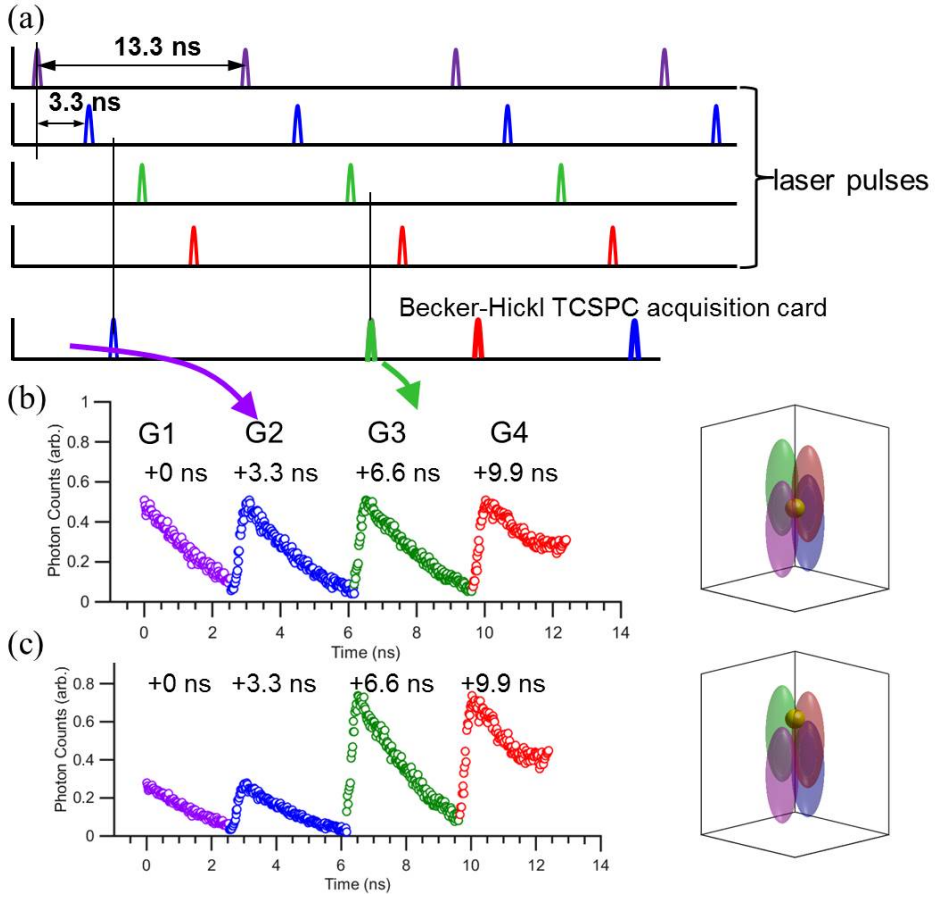

Figure 6. Spatiotemporally multiplexed two-photon excitation and temporally demultiplexed detection **(a)** 76 MHz pulsed laser from a Ti-sapphire oscillator is split into 4 beams, with each beam delayed by 3.3 ns relative to the preceding one. **(b)** Using a TCSPC acquisition card, each detected photon can be assigned to a specific time gate (G1~G4), leading to four fluorescence decay curves. The relative photon counts in each time gate (*i.e.* the area underneath the decay curve) can be used to infer the particle's 3D position. When the tracked particle is right at the center of the tetrahedron, photon counts in all time gates are about equal. The gold sphere in the excitation tetrahedron schematic represents the tracked particle. **(c)** When the particle moves away from the tetrahedron center, the photons counts in each time gate decrease or increase accordingly.

When the molecule sits right at the center of the excitation tetrahedron, the photon counts are approximately equal in all time gates. Any xyz displacement of the molecule

from the center can be estimated via the normalized photon count difference in the four time gates (*i.e.* error signal). A closed feedback loop then drives the galvo mirrors and the objective z-piezo mover to lock the excitation tetrahedron on the molecule for tracking.

1.3.4 Hybrid tracking system

Orbital tracking, confocal tracking, and TSUNAMI microscopes are superior to the camera-based tracking systems in probing fast dynamics of a single emitter. However, it can be equally important to find out how the single-molecule motion fits into the context of the entire biological system. The lack of contextual information (*e.g.*, cellular micro domains or neighboring molecules) poses the risk of misinterpreting the molecular behavior. Motivated by these concerns, Bewersdorf's group has developed a hybrid system that combines camera based biplane imaging with feedback SMT[54, 137]. In Bewersdorf's design, fluorescence of the molecule is split and separately collected in the two regions of an EMCCD, whose conjugate planes in the sample space are axially offset by ~750 nm. The fluorescence image acquired in either of these two regions directly reports the molecule's lateral position, whereas the image difference in the two regions can be used to discern the axial position. While using cameras for tracking could potentially facilitate co-registration of molecular trajectories and cellular images, camera-based tracking does not offer TCSPC analysis. It should be noted that spinning disk microscopy[136] and two-photon laser scanning microscopy[62] can be integrated into the orbital/confocal/TSUNAMI tracking microscopes to provide a view of slowly varying large-scale context where the rapidly diffusing molecules reside.

1.4 SCOPE AND ORGANIZATION OF THE DISSERTATION

The confocal tracking microscope was originally developed by Dr. James Werner at LANL. Fascinated by this technology, we built an identical system in our own lab (Chapter 2). Unfortunately, we didn't have a clear "big picture" to pursue until 2014. In 2014, W.E. Moerner group published a paper on biomolecular interaction visualization using their ABEL trap[72], which greatly inspired us since in vitro single-molecule detection is precisely the niche of our tracking microscope. Theoretically we can even do better than ABEL trap in biomolecule association/disassociation measurement because of the absence of artifacts that come from 2D confinement and electrokinetic force.

My contribution is to realize this opportunity by overcoming a series of technical challenges. Limited tracking duration, which is largely caused by the fast diffusion of target molecules, is the first obstacle (Chapter 3). The Stokes-Einstein equation tells us the slow-down of Brownian motion can be achieved either by increasing the medium viscosity, or the molecule's hydrodynamic radius. We conclude that the later approach is more promising and favorable due to its compatibility with biomolecules' natural activity and chemical cocktails that can increase photostability or emission rate[138] of the fluorophore.

Despite the efforts to extend the tracking duration, we still cannot observe a DNA molecule for a time longer than its dwell time in the hybridized/melted state, making the transient binding rates measurement extremely difficult. Imagine that we would like to measure the average time interval between buses in New York winter, but we never actually see one bus's departure and the next one's arrival because we are reluctant to stay at the bust stop for more than 3 minutes and become a snowman. Bearing that in mind, we need algorithms that can statistically "stitch" the short trajectories together. Through simulations, we have identified two (vbSPT in Section 4.2 and ebFRET in Section 4.3, Chapter 4) algorithms from the literature that have such population-level analysis

capability.

The most straightforward and generic way to probe a biomolecule's association is detecting the diffusion coefficient change from its 3D trajectory, since the association is usually accompanied by modification in the molecule's size. However, we found that the original design of confocal tracking microscope gave a huge error in binding rates characterization, due to the temporally correlated z tracking errors. In Section 4.2, we introduce a maximum likelihood estimation (MLE) algorithm that can better estimate target molecule's 3D coordinate, thereby decorrelating the z-tracking errors and increasing the z tracking accuracy significantly. Surprisingly, this temporal correlation (memory) issue has never been discussed anywhere else, although it is a common problem in the 3D SMT field.

An alternative contrast mechanism to differentiate a single biomolecule and its dimer/complex is Förster resonance energy transfer (FRET). This contrast is introduced to the DNA model system by labeling the ssDNA with an Atto dye, and its complementary strand with a dark quencher (Section 4.3). The optimization of the dye-quencher spacing is tedious and consumes most of the time. The fun part in this project is the implementation of a MLE algorithm for small-photon-number fluorescence lifetime fitting, without which 15 ms temporal solution for the FRET signal monitoring of a diffusing organic dye would be impossible.

I began a side project at the end of my fourth year trying to establish a theoretical model for rare molecule species quantification based on single-molecule fluorescence lifetime classification (not fitting!). The results (Chapter 5) turn out to be quite interesting although the statistical formulation is oversimplified and trivial.

The dissertation is mainly based on the following journal publications:

* **C. Liu**, Y.-L. Liu, E.P. Perillo, A.K. Dunn and H.-C. Yeh, "Single-molecule tracking and its application in biomolecular detection," *IEEE Journal of Selected Topics in*

Quantum Electronics 22(4): 6804013, 2016.

* **C. Liu**, Y.-L. Liu, E.P. Perillo, N. Jiang, A.K. Dunn and H.-C. Yeh, "Improving z-tracking accuracy in the two-photon single-particle tracking microscope," *Applied Physics Letters* 107, 153701, 2015.

* **C. Liu**, A. Rastogi and H.-C. Yeh, "Quantification of rare single-molecule species based on fluorescence lifetime," *Analytical Chemistry* (under revision).

* **C. Liu**, J.M. Obliosca, Y.-L. Liu, Y.-A. Chen, N. Jiang and H.-C. Yeh, "3D single-molecule tracking enables direct hybridization kinetics measurement in solution," *Nanoscale* (under review).

To summarize, there are two ways of thinking about the SMT technique. One is that it depicts a detailed movement trajectory that facilities our understanding of biomolecule transport and dynamics inside the cell, which is so far what most 2D SMT have demonstrated. The other is that SMT microscope is simply a “tweezer” that keeps a molecule inside the detection volume so that it can be observed for an extended period, and the information of our interest is encoded in the emission photons. This dissertation exclusively focuses on the second type application, although future direction might be a combination of two—building a spatiotemporal resolved molecular binding kinetics map inside a cell.

Chapter 2: Confocal-feedback tracking microscope[1]

2.1 THEORY, SIMULATION AND OPTIMIZATION

The design of our confocal-feedback tacking microscope is essentially the same with Werner's. The basic idea is simple: we continuously estimate the Brownian displacement of the target molecule from the laser focus center, and manipulate the molecule back to the center by moving a three-axis piezo stage underneath the sample. Rapid update of the feedback cycle (200 times per second) keeps the molecule near the center of the laser focus until the molecule is photobleached or escapes the detection volume. The movement history of the piezo stage represents the molecule's 3D trajectory.

The way our tracking microscope infers the molecule's lateral position is similar to a quadrant detector. It utilizes two optical fiber bundles for photon collection. The two fiber bundles have panda style input faces, one orientated in the x-direction, the other orientated in the y-direction. Each fiber in the bundles is connected to an avalanche photodiode. From the photon counts in the fibers (I_1, I_2, I_3, I_4), the xy displacement of the molecule is computed using Equation (2.1)-(2.2), where E_X and E_Y are constants termed the error signals.

$$E_x = \frac{I_1 - I_2}{I_1 + I_2}$$
$$E_y = \frac{I_3 - I_4}{I_3 + I_4} \tag{2.1}$$

$$\Delta x = k_X E_X$$
$$\Delta y = k_Y E_Y \tag{2.2}$$

1 Part of this chapter has been previously published in: C. Liu, E.P. Perillo, Q. Zhuang, K.T. Huynh, A.K. Dunn, and H.-C. Yeh, "3D single-molecule tracking using one- and two-photon excitation microscopy," SPIE Proceedings 89501C, 2014. I performed the simulations and wrote the manuscript.

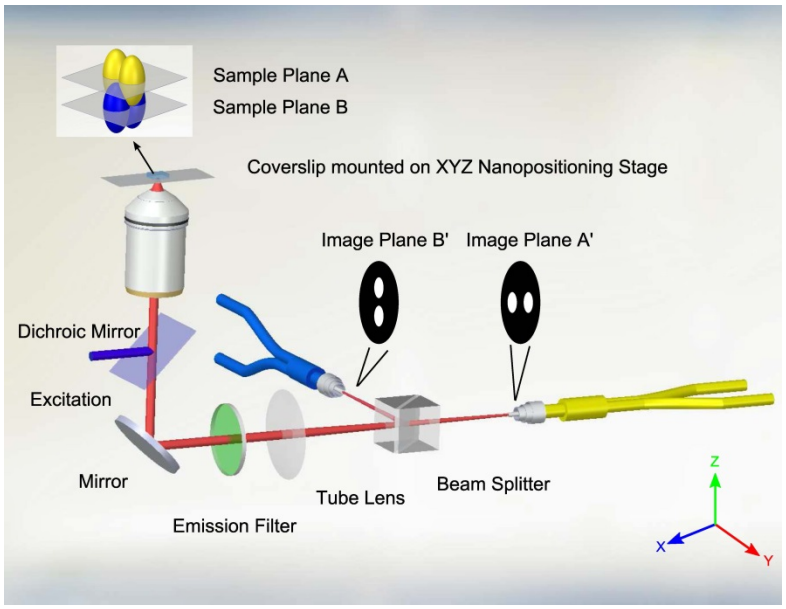

Figure 7. Schematic of the confocal-feedback tracking microscope. The sample suspended on a coverslip is mounted upon a three-axis, piezoelectric stage. Fluorescent molecules are excited by the laser through a water-immersion objective. The fluorescence is collected by the same objective, focused by the tube lens, and then split evenly onto two orthogonally installed optical fiber bundles. Each bundle consists of two multimode optical fibers. The fiber input faces serve as pinholes to filter out-of-focus light. The fiber bundles (blue and yellow) are not only orthogonally installed but also slightly offset along the optical axis, leading to a tetrahedral arrangement of the four probe volumes in the sample space. The xyz position of the target molecule is estimated from the differences in photon counts of the single-photon counting modules (SPCM) connected to the fibers.

The trick for z-position sensing is similar to dual focal plane imaging. The two fibers bundles are slightly offset along the optical axis, so that they image distinct planes within the sample, one above the laser focus, the other below the laser focus. If the molecule is right at z = 0 μm, then two fiber bundles will have the same photon counts ($I_1 + I_2 = I_3 + I_4$). Any displacement from the laser focal plane can be calculated by Equation (2.3)-(2.4).

$$E_z = \frac{(I_1 + I_2) - (I_3 + I_4)}{(I_1 + I_2) + (I_3 + I_4)} \tag{2.3}$$

$$\Delta z = k_Z E_Z \tag{2.4}$$

Since each optical fiber only accepts light from an extremely small sample volume (~1 fL, termed confocal volume), out-of-focus background can be greatly suppressed. This spatial filtering mechanism guarantees the signal-to-noise ratio (SNR) necessary for single-molecule detection.

2.1.1 Laser intensity distribution modeling

A prerequisite for successful single molecule detection is a high efficiency of collection of the emitted fluorescence photons. At the same time, we have to keep the detection region small to minimize background (including fluorescence from other molecules and Raman scattering). In our design, this is accomplished by tightly focusing the excitation laser with a high NA objective, and placing spatial filters (input faces of the multimode fibers in use are equivalent to the pinhole in a standard confocal microscope) in the detection path. How does the objective and spatial filters affect the single-molecule tracking? To answer this question, it's necessary to predict the number of detected fluorescence photons for any possible location of the molecule. The photon number is proportional to two factors (1) the fluorescence emission intensity, which is proportional to the excitation laser intensity experienced by the molecule before fluorescence saturation occurs (2) the efficiency with which photons from the fluorescent molecule are detected. In this section, we first calculate the laser intensity distribution $I(\vec{r}, \mathrm{z})$.

The excitation laser intensity is usually assumed to have Gaussian-Lorentzian geometry in the focal region. The intensity distribution of the excitation beam can be expressed as:

$$I(\vec{r}, z) = I(0, z)\exp(-\frac{2|\vec{r}|^2}{\omega^2(z)})$$

where $I(0,z) = 2P_0/\pi\omega^2(z)$, and $\omega^2(z) = \omega_0^2 + z^2(\lambda/n\pi\omega_0)^2$.

The assumption of Gaussian-Lorentzian geometry is sufficiently correct as long as the paraxial approximation holds[13]. However, when focusing a Gaussian laser beam by a microscope objective with high numerical aperture (N.A.), this approximation is no longer valid. Richard and Wolf[139] started from the assumption that the objective is perfectly aplanatic, and gave a set of compact expressions of electrical field $\vec{e}(P)$ near the focal point of the objective. The assumption of aplanatic imaging properties can be satisfied for state-of-the-art objectives. The excitation intensity $I(\vec{r},\mathrm{z})$ is proportional to $|\vec{e}(P)|^2$.

$$\begin{aligned} e_x(P) &= -iA\left(I_0 + I_2\cos 2\phi_p\right) \\ e_y(P) &= -iAI_2\sin 2\phi_p \\ e_z(P) &= -2AI_1\cos 2\phi_p \end{aligned} \tag{2.5}$$

$$\begin{aligned} I_0 &= I_0(kr_p,\theta_p,\alpha) = \int_0^\alpha \sqrt{\cos\theta}\sin\theta(1+\cos\theta)J_0(kr_p\sin\theta\sin\theta_p)e^{ikr_p\cos\theta\cos\theta_p}d\theta \\ I_1 &= I_1(kr_p,\theta_p,\alpha) = \int_0^\alpha \sqrt{\cos\theta}\sin^2\theta J_1(kr_p\sin\theta\sin\theta_p)e^{ikr_p\cos\theta\cos\theta_p}d\theta \\ I_2 &= I_2(kr_p,\theta_p,\alpha) = \int_0^\alpha \sqrt{\cos\theta}\sin\theta(1-\cos\theta)J_2(kr_p\sin\theta\sin\theta_p)e^{ikr_p\cos\theta\cos\theta_p}d\theta \end{aligned} \tag{2.6}$$

$$n\sin\alpha = \mathrm{NA} \tag{2.7}$$

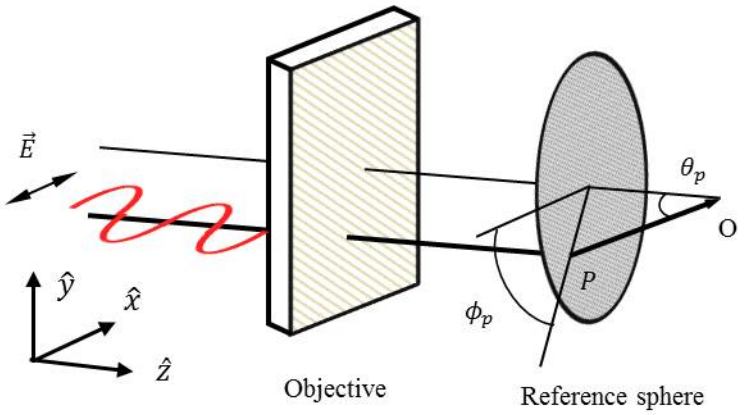

Figure 8. Schematic of the focusing geometry through the objective. A point source is assumed to be at infinity and give rise to a linearly polarized (along the x-direction) monochromatic plane wave at the entrance pupil of the objective. The objective here is perfectly aplanatic, which transforms an incident planar wavefront into a segment of a spherical wavefront. The origin ($\vec{r} = 0, \mathrm{z} = 0$) of the sample space coordinate system is at the focus of the laser beam. θ_p and ϕ_p are the polar angle and the azimuthal angle, respectively.

Figure 9(a) shows the laser beam intensity computed by the electromagnetic model. Although the electromagnetic model (Equation (2.5)-(2.7)) is expected to provide a better approximation of the laser intensity distribution, the Gaussian-Lorentzian model is much less computationally expensive. We will compare the error signals calculated from these two methods and determine which one is better suitable for further system modeling.

2.1.2 Collection efficiency function calculation

The efficiency with which photons from a fluorescent molecule are detected is formally described by photon collection efficiency function $\mathrm{CEF}(\vec{r}, \mathrm{z})$, where $(\vec{r}, \mathrm{z})$ is the molecule's 3D position. Here we have employed a geometric approximation of CEF in simulation, which has been proved to be reasonably accurate for typical confocal imaging[140]. If we introduce pinhole diameter in sample space s_0, $\mathrm{R} = r/s_0$, and $\mathrm{Z} = \sqrt{z^2 tan^2(\alpha) + \omega_0^2}/s_0$, then

$$\mathrm{CEF}(\vec{r}, \mathrm{z}) = \begin{cases} \left[H(Z-1-R)\cdot\pi + H(R-Z+1)\cdot H(Z+1-R)\cdot\left(\beta_1 + 2\beta_2 Z^2 - 2A(1,R,Z)\right)\right]\dfrac{1-\dfrac{Z}{\sqrt{Z^2+tan^2(\alpha)}}}{1-\cos(\alpha)}\dfrac{s}{\pi}, Z > 1 \\ \left[H(1-Z-R)\cdot\pi Z^2 + H(R-1+Z)\cdot H(Z+1-R)\cdot\left(\beta_1 + 2\beta_2 Z^2 - 2A(1,R,Z)\right)\right]\dfrac{1}{\pi Z^2}, \mathrm{Z} \le 1 \end{cases} \quad (2.8)$$

where $H(x) = \begin{cases} 1, x \ge 0 \\ 0, \ x < 0 \end{cases}$ is the Heaviside step function, $A(a,b,c)$ is the Heron's formula for triangle area calculation. Other parameters are defined as the following:

$$\alpha = \arcsin(\mathrm{NA}/n)$$
$$\beta_1 = \operatorname{acos}\left(\frac{1+R^2-Z^2}{2R}\right)$$
$$\beta_2 = \operatorname{acos}\left(\frac{R^2+Z^2-1}{2RZ}\right) \tag{2.9}$$
$$\omega_0 = \frac{\lambda}{n\pi\tan(\alpha)}$$

n is the refractive index of the medium between the objective front lens and the specimen. Figure 9(b) show the z-stacks of CEF slices at different depths. Each slice has the size 2 μm × 2 μm. Note that at the z = ±0.25 μm planes, two CEFs start to merge, indicating that the spatial resolving power fades away.

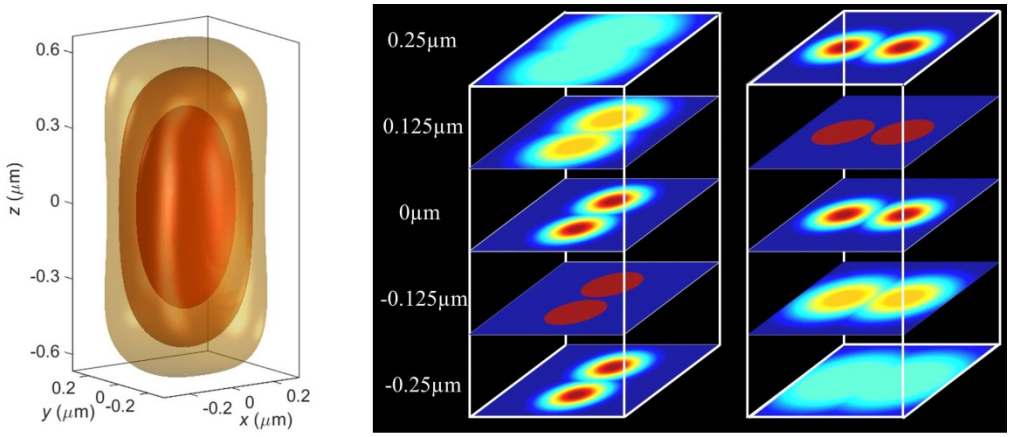

Figure 9. Optical modeling of single-molecule excitation and detection (**a**) Electromagnetic modeling of the laser beam intensity distribution. The plot shows isosurfaces where the intensity has fallen off to 1/*e*, 1/e^2 and 1/e^3 of its max value. (**b**) Z-stacks of collection efficiency function (CEF). CEF is a map of relative photon counts collected from a dipole emitter for a given location in the sample space. The left stacks correspond to the y-orientated fiber bundle, while the right stacks correspond to the x-orientated fiber bundle. Red color indicates high efficiency. In this simulation, fiber core diameter is 50 μm, the two fiber bundles are separated by 0.25 μm in the sample space and are symmetrical around the laser focal plane at z = 0. Laser wavelength is 640 nm, NA=1.2, magnification=75.

2.1.3 Error signals calculation

The error signals (E_X, E_Y, E_Z) provide important insights into the system performance. Their slopes are directly related to the position sensitivity and hence tracking accuracy. Their linear regions are where the molecule's displacement can be unambiguously resolved by Equation (2.1)-(2.4). We have compared the error signals given by the Gaussian-Lorentzian and electromagnetic model. The simulation results are shown in Figure 10. We can see that the difference between the two types of error signals is negligible, simply because of the dominant influence of collection efficiency function. Therefore, the Gaussian-Lorentzian model is sufficiently accurate and it should be employed for further studies. Since the slope of E_{Z} is smaller than $E_{\mathrm{X/Y}}$, we expect that z tracking accuracy will be worse than xy tracking accuracy.

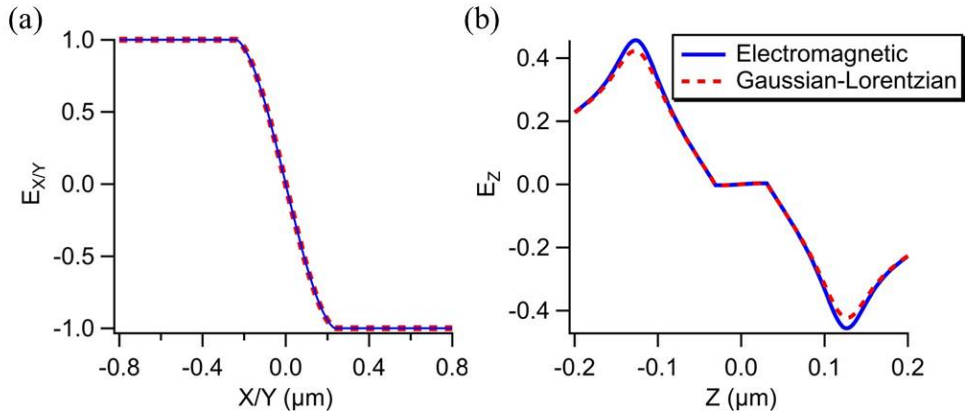

Figure 10. Error signals derived from electromagnetic modeling (blue solid curves) and Gaussian-Lorentzian modeling (red dashed curves) of the laser beam. (**a**) Error signals along the x/y direction (**b**) Error signals along the z direction

2.1.4 Optical configuration optimization

There are many parameters that govern the system's performance, such as the objective magnification, fiber bundle z-separation, and proportional gains (k_{X}, k_{Y} and k_{Z}). We have used Monte Carlo simulations to optimize these parameters. The target

molecule is modeled as diffusing in free space with diffusion coefficient D. For each time interval Δt, the molecule travels a distance $\Delta s = \chi\sqrt{2D\Delta t}$ along certain axis. χ is a random number generated from standard normal distribution[141]. The photon count k in each detector follows the Poisson distribution $P(k,\lambda) = \lambda^k e^{-\lambda}/k!$, where the parameter λ is proportional to the excitation intensity $I(\vec{r},\mathrm{z})$. Once the photon counts fall below the specified threshold, the tracking is terminated. Figure 11 shows the dependence of tracking duration on objective magnification M and fiber bundle axial separation in sample space.

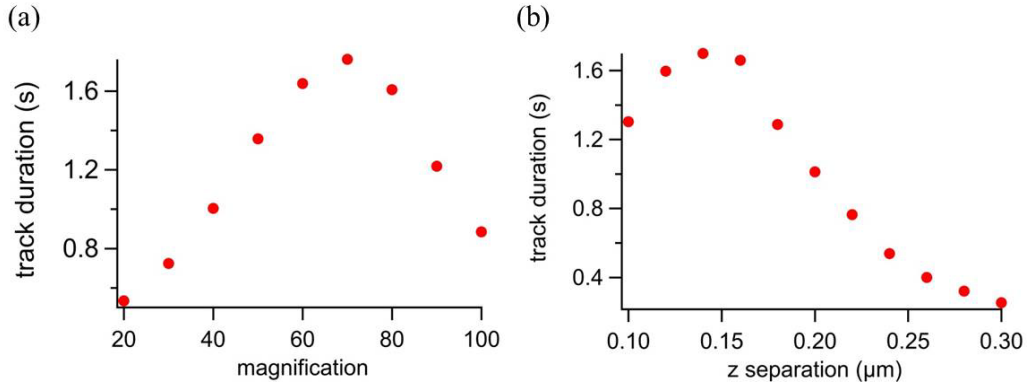

Figure 11. Median tracking duration as a function of (**a**) objective magnification and (**b**) fiber bundle separation in the sample space. The statistics were gathered from 150 shots for each parameter with fixed gain factors ($k_\mathrm{X} = k_\mathrm{Y}$ =0.35, k_Z =0.4). The fluorescent particle has a diffusion coefficient D = 1.5 μm^2/s. M=70 and Δz =0.14 μm gave the longest tracking duration.

We have also optimized feedback gain factors with tracking error as the performance metric. The results are shown in Figure 12. As expected, the tracking system has a much better tracking accuracy in the lateral direction than in axial direction. Due to the symmetry of optics, k_X and k_Y are always set to be equal. Tracking accuracy in xy is only loosely dependent on k_Z; similarly, tracking accuracy in z is insensitive to k_X and k_Y.

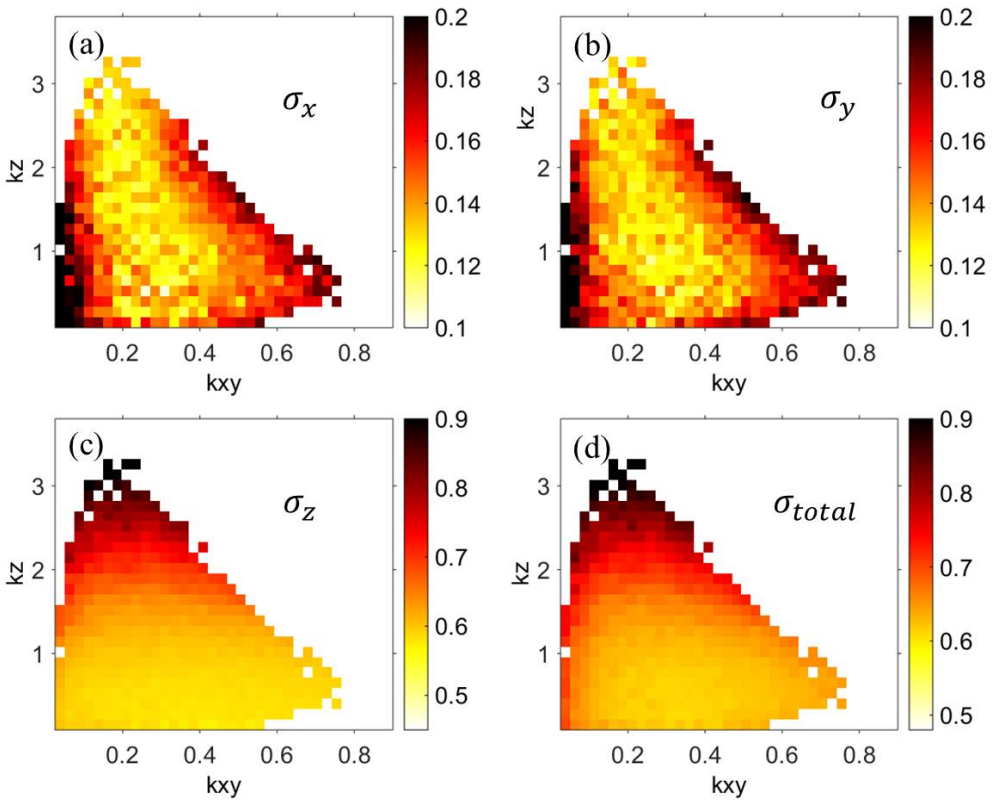

Figure 12. Tracking errors over a range of feedback gain parameters ($k_{\mathrm{XY}}, k_{\mathrm{Z}}$) for tracking the Brownian motion of a fluorescent particle with diffusion coefficient D = 0.5 $\mu m^2/s$. Each pixel represents the mean squared distance (σ) between the molecule position and stage position for a given set of (k_{XY}, k_Z). Panel (**d**) is the total mean squared distance $\sigma_{total} = (\sigma_x^2 + \sigma_y^2 + \sigma_z^2)^{1/2}$. For each ($k_{\mathrm{XY}}, k_Z$), σ is averaged from twenty 1-second runs. Tracking errors are only shown for (k_{XY}, k_Z) that enables at least ten 1-second tracking out of the twenty runs. Z tracking error (>200nm) dominates in σ_{total} but is still below the diffraction limit. XY tracking errors are ~100nm.

2.2 INSTRUMENTATION

2.2.1 System layout

The 3D tracking microscope is built around an Olympus IX71 microscope. Pulsed laser (average power 100 μW, repetition rate 10 MHz) from PicoQuant LDH-P-C-640B is reflected by the dichroic mirror (Semrock FF650-Di01-25x36), and then focused by a 60X NA=1.2, water immersion objective (UPLSAPO 60XW). The laser beam size is controlled by a Keplerian beam expander (Figure 13) for slightly underfilling the objective. The fluorescence is collected by the same objective, and filtered by ET700/75m (Chroma). Based on the number of photons collected in two optical fiber bundles (Polymicro, 50-μm core diameters, 55-μm center-to-center spacing) in every 5 ms, a xyz piezo stage (P-733K130, PI) with $30 \times 30 \times 30$ μm travel range is used to reposition the fluorescent molecule to the center of excitation focus. Photographs of the 3D tracking setup are shown in Figure 14.

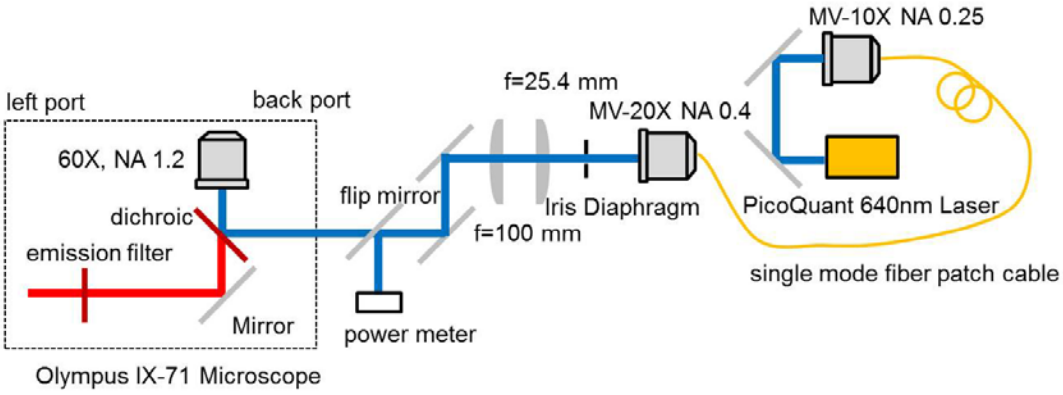

Figure 13. Excitation path of the confocal tracking microscope

Our tracking microscope is an integrated system that requires the laser, detector, data acquisition module, piezo stage and computers to be synchronized. We do so by using the PCI-6602 counter board as the master clock (Figure 15). The sync channel (CHANNEL

0) of PicoHarp 300 is connected to the SYNC OUTPUT of the PDL-800B picosecond pulsed diode laser driver. PHR 800 is a 4-channel detector router that supports simultaneous multichannel time-resolved measurement.

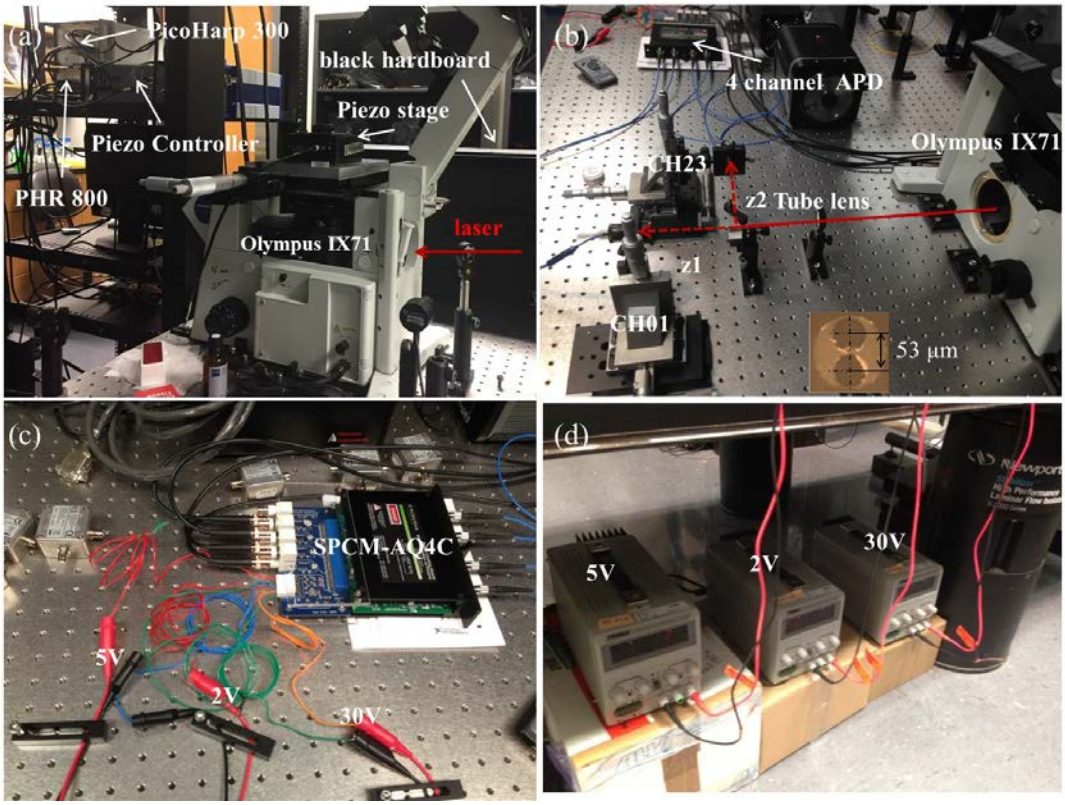

Figure 14. Photographs of the 3D confocal-feedback tracking setup (**a**) The excitation light goes into the microscope from the back port. The piezo stage is attached to the microscope through a custom-made adapter. The detection branch is covered by a black hardboard box (**b**) The detection branch with hardboards lifted. The original tube lens in the microscope is removed. The emission light is focused by an Edmund f=225 mm achromatic lens, and splitted by a 50/50 non-polarizing beam splitter cube. The inset is an image of the fiber bundle input surface. The two multimode fibers have a center-to-center spacing of 53 μm. (**c**) The 4-channel photon counting card SPCM-AQ4C. Its peak photon detection efficiency is 60% at 650 nm. (**d**) The DC power supplies for SPCM-AQ4C.

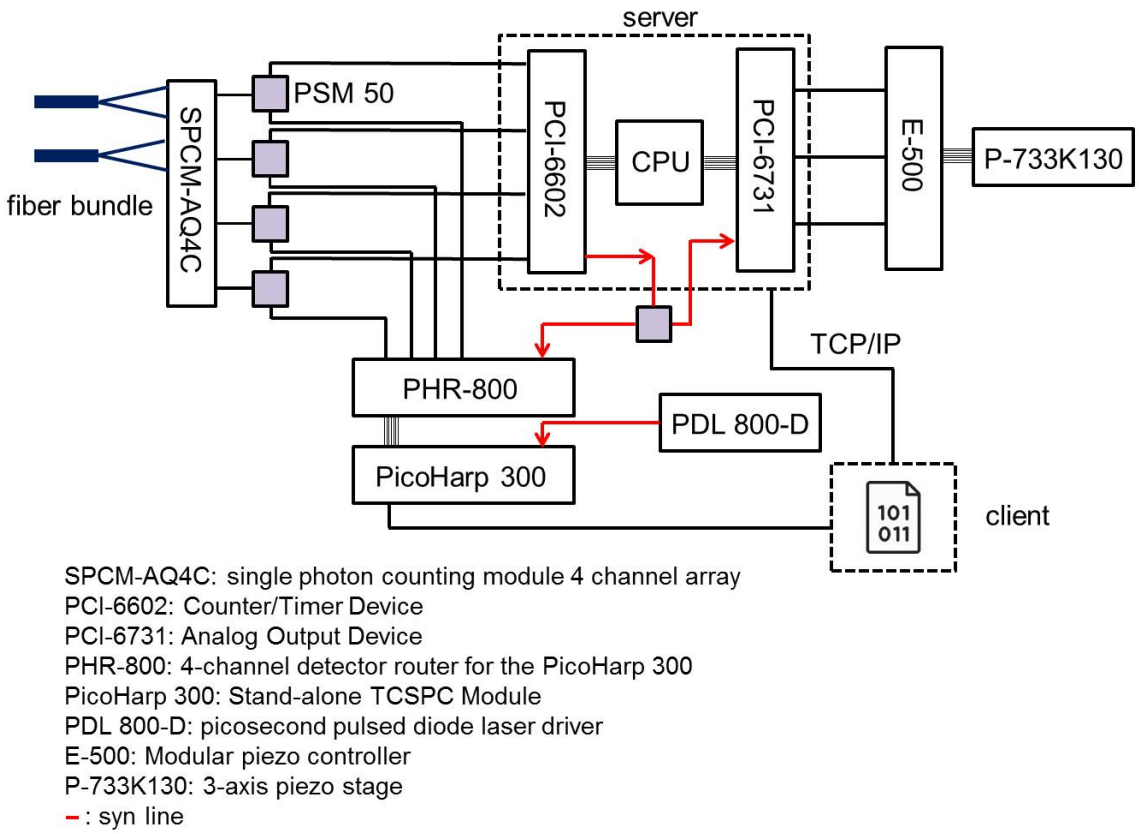

Figure 15. Electric connection diagram of confocal-feedback tracking system

2.2.2 Determine BFP of the tube lens by FCS

The z sensitivity of the tracking system is provided by two axially offset fiber bundles. Their distances to the tube lens are slightly different, so that they image two distinct planes in the sample space. Ideally, these two planes are symmetrical about the objective focal plane. Since the objective is infinity-corrected, if the fiber bundles are positioned at the back focal plane (BFP) of the tube lens, they will have largest photon collection efficiency. We have used the BFP of the tube lens as a reference position (z = 0) to find the optimal axial spacing of the two fiber bundles.

To find the BFP of the tube lens, we have performed a series of FCS experiments on 4 nM Qdot® 605 ITK™ Amino (PEG) Quantum Dots. The autocorrelation function

averaged from ten 20-seconds runs is fitted by Equation (2.10), in which N is the average number of fluorescent particles in the detection volume, τ_D is the characteristic residence time in the detection volume, $\alpha = \omega_{xy}/\omega_z$ is the ratio of radial and axial e^{-2} radius of the laser focus, F is the fraction of particles that have entered the triplet state (an non-emission state), and τ_F is the relaxation time of the triplet state[142]. Representative autocorrelation curves are shown in Figure 16(a). The average single QD brightness (SQDB) is defined as the photon count rate divided by N.

$$G(\tau) = \frac{1}{N}\frac{1}{(1+\tau/\tau_D)(1+\alpha^2(\tau/\tau_D))^2}\left(1+\frac{F}{1-F}e^{-\tau/\tau_F}\right)+G(\infty) \qquad (2.10)$$

As we moved the fibers bundles along the optical axis with a 500 μm interval, SQDB measured at each location is recorded and shown in Figure 16(b). The BFP of the tube lens is where the maxima of the SQB are achieved (grey vertical line). Starting from the BFP, we moved the fiber bundle in the transmission channel further away from the tube lens, and the fiber bundle in the reflection channel closer to the tube lens. The errors signals are collected by 3D scanning single QD605 immobilized on the coverslip.

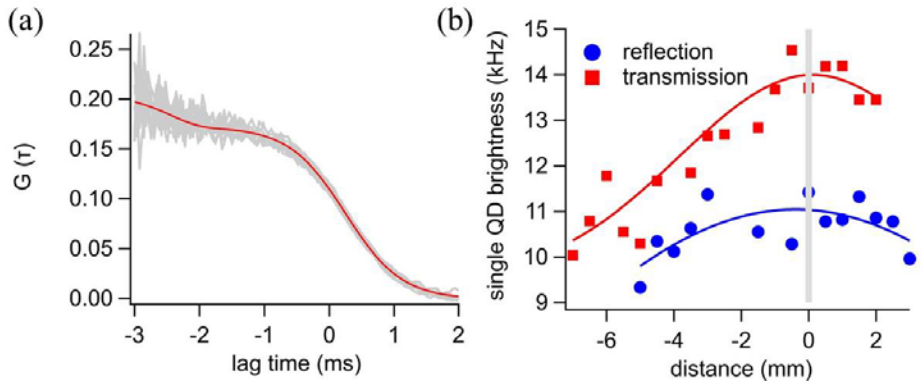

Figure 16. Determine the BFP of the tube lens with FCS (**a**) Ten autocorrelation curves (gray) are averaged and fitted (red). The lag time is in log10 scale. (**b**) Single QD brightness measured as a function of the displacement of the fiber bundle from tube lens BFP.

2.2.3 Determine fiber bundles positions relative to BFP

To reach the optimal axial separation (140 nm) of the fiber bundle predicted by our simulation, the count rates of single QD spread among all four fibers are recorded as a function of the QD xyz location. The first approach we have tried is to perform 2D Gaussian fitting (Equation (2.11)) of the measured point spread function (PSF) of single quantum dots with maximum likelihood estimation algorithm[143], and use N/σ^2 as a metric to find the conjugate planes of the fiber bundles input faces in the sample space. Then the axial spacing between the two conjugate planes can be calculated.

$$\mathrm{PSF} = \frac{N}{2\pi\sigma^2}\exp\left(-\frac{(x-u_x)^2+(y-u_y)^2}{2\sigma^2}\right)+b^2 \tag{2.11}$$

However, it turned out that N/σ^2 is not sensitive to the z position of QD, and the conjugate planes cannot be found with an uncertainty smaller than 150 nm. Therefore, we

instead optimized the z error signal. A tradeoff between the dynamic range[2] and the sensitivity[3] can be clearly seen in the error signals plotted in Figure 17.

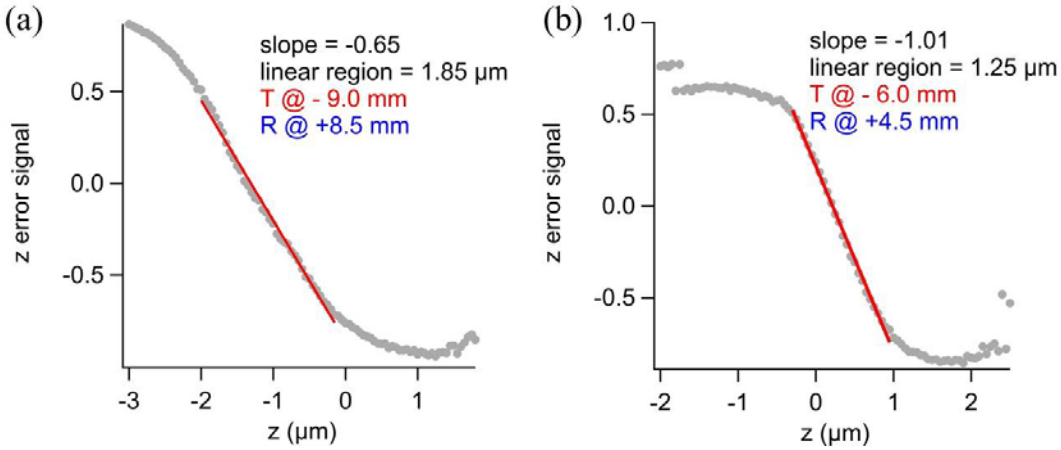

Figure 17. Tradeoff between sensitivity and dynamic range (**a**) When the two fiber bundles are more axially separated (the separation between fiber bundles in image space is 17.5 mm), the dynamic range is 1.85 µm and the sensitivity is 0.65 μm^{-1}. (**b**) When the fiber bundles are less axially separated (the separation is 10.5 mm in image space), the dynamic range is smaller (1.25 µm) but the sensitivity is larger (1.01 μm^{-1}).

The smaller the dynamic range, the easier the molecule escapes the confocal volume, the shorter the tracking duration is. Therefore, a large dynamic range is favored when we want to achieve longer tracking duration (especially when the molecule diffuses fast). On the contrary, good sensitivity is favored when the target molecule moves relatively slow, since a small dynamic range is sufficient to keep the molecule in the confocal volume. The major factor limiting the application of SMT microscope in biological studies currently is the tracking duration, instead of the tracking accuracy.

[2] Dynamic range is defined as the size of range in which the fluorescence molecule's coordinate is directly proportional to the error signal. Once the molecule is outside this range, its position cannot be resolved by Eq. (2.2)-(2.4). Therefore, the linear region size of the error signal is the dynamic range.

[3] Sensitivity represents how much the error signal will change given one-micron displacement of the fluorescent molecule. It is defined as the slope of the error signal linear region. Better sensitivity naturally leads to better tracking accuracy; therefore, these two concepts are used interchangeably in this dissertation.

Therefore, we have chosen a large fiber bundle axial separation that favors the dynamic range. The error signals along x- and y- direction, as well as the CEF under this condition are shown in Figure 18. The sensitives in x and y are 3.7 μm^{-1} and 3.96 μm^{-1} respectively, which are 5.7 times larger than that in z. The sensitives of the tracking system are determined by the gradient of excitation intensity. Due to the elongated excitation volume, the sensitivity is considerably smaller in the z direction, resulting in a much worse z-tracking accuracy. Other than this native sensitivity issue, the dependence of E_z on emitter's xy position can also deteriorate the z-tracking accuracy.

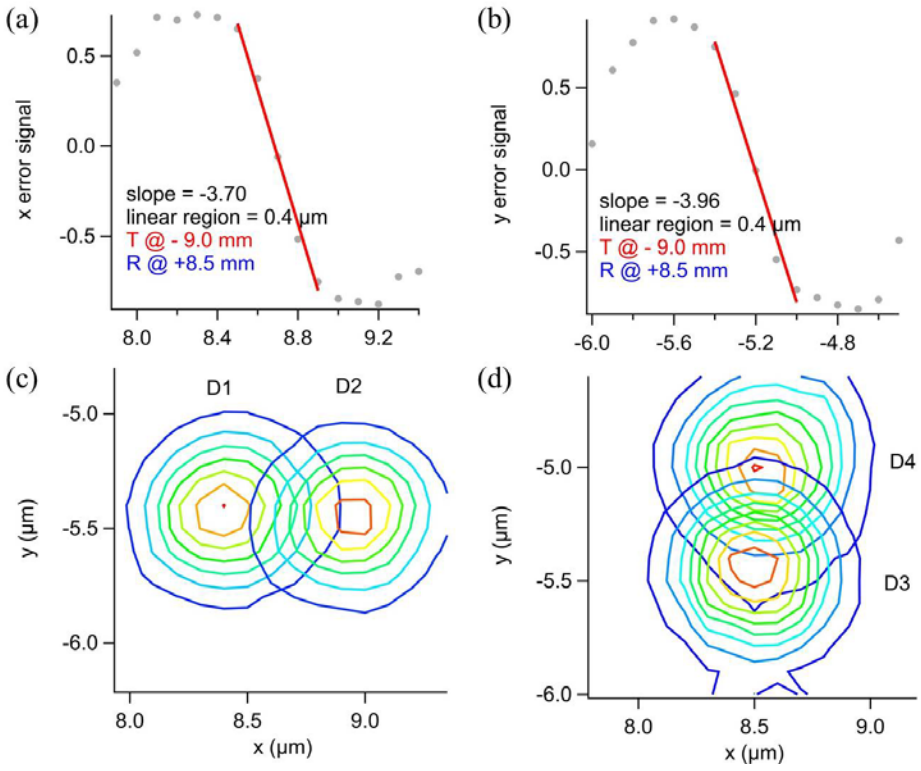

Figure 18. Error signals and CEF under optimal condition Top: error signals along (**a**) x axis and (**b**) y axis. Red solid lines are linear fits to the linear portion of the error signals. The linear slopes for x and y are -3.70 and -3.96 respectively. Bottom: contour plots of the collection efficiency function near z = 0 measured through four fibers. (**c**) Transmission channel (**d**) Reflection channel

There are ways to improve the z-tracking accuracy, *e.g.* through point-spread-function (PSF) engineering – the sharper the PSF, the better the resolution and tracking accuracy. Examples to achieve sharper excitation profiles in z include 4Pi microscopy[144] and IsoSTED[145]. While both techniques offer significantly increased z resolution, they cannot be easily integrated into most microscopes. The dual-objective arrangement in 4Pi microscopy typically interferes with the sample preparation. The need of both lateral and axial depletion beams makes IsoSTED alignment difficult. Besides, a high laser power is used in IsoSTED (typically >100 mW), leading to increased photobleaching rate and cell death.

2.3 TRACKING PERFORMANCE EVALUATION

2.3.1 Tracking accuracy characterization

To characterize the tracking accuracy of our setup, an immobilized fluorescent bead (Thermo Fisher Scientific F8783, 20 nm) is programmed to move in a pattern that reads "UTBME" (see Figure 19), with a speed of 5 μm/s. The same piezo stage that is used to move the bead is also used for tracking in a time-multiplexed way. By comparing the predefined trajectory of the fluorescent bead with its trajectory inferred from the tracking mechanism, the RMS tracking accuracy has been determined to be 25 nm in xy and 81 nm in z. Clearly, our tracking accuracy is beyond the diffraction limit of light.

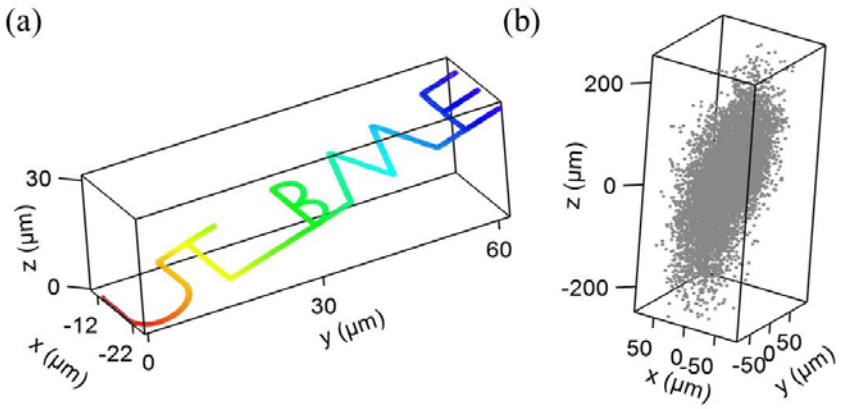

Figure 19. Tracking accuracy characterization (**a**) 3D trajectory of the fluorescent bead inferred from the tracking mechanism (**b**) the scatter plot of tracking error in x, y and z.

2.3.2 Diffusion coefficient characterization

In the above control experiment, the true trajectory of the fluorescent bead is known. To further validate the 3D trajectory obtained by our setup when the true trajectory is unknown, we have compared the theoretically predicted and measured diffusion coefficient value of a F8783 bead freely diffusing in 90 wt % glycerol (Figure 20). The diffusion coefficient D can be predicated by the Stokes-Einstein equation:

$$D = \frac{k_B T}{6\pi\eta r} \tag{2.12}$$

Where k_B is the Boltzmann's constant (1.38 × 10^{-23} m^2 kg s^{-2} K^{-1}), T is the absolute temperature (294K), η is the dynamic viscosity (0.1571 Ns/m^2, based on an empirical formula[146]), and r is the radius of the spherical particle (10 nm). D is calculated to be 0.14 μm^2/s.

On the other hand, D can be obtained by the mean-squared-displacement (MSD) analysis of the experimental single-particle trajectory. MSD (ρ) is defined in Equation (2.13):

$$\rho_{n\Delta t} = \frac{1}{N-n}\sum_{i=1}^{N-n}(\vec{r}_{i+n} - \vec{r}_i)^2, \quad i = 1, 2, ..., N-1 \tag{2.13}$$

where Δt is the frame duration, $r_i = (x_i, y_i, z_i)$, $i = 1,2,\ldots,N$ is the observed trajectory[147]. For normal diffusion[148], MSD and diffusion coefficient is related by $\rho = 6D$t. Therefore a least-square fit of a straight line to ρ versus t gives D. For larger number of n, fewer displacements of duration $n\Delta t$ are available and therefore the later MSD points have larger variance. In order to reduce the influence of the large variance of the later MSD points, only the first few points of the MSD curve are used. The optimal number p of MSD points to use is dependent on the particle localization error σ, number of data points N in the trajectory, and approximated diffusion coefficient D_{appr}. The exact relation[149] can be found in Equation (2.14)-(2.15)

$$x = \frac{\sigma^2}{D_{appr}\Delta t}$$

$$f = 2 + 1.35x^{0.6} \tag{2.14}$$

$$L = 0.8 + 0.564\mathrm{N}$$

$$p = \min(L, f \cdot L / (f^3 + L^3)^{1/3}) \tag{2.15}$$

The diffusion coefficient derived from MSD analysis of the experimental trajectory is 0.137 $\mu m^2/s$, which is almost identical to the theoretically predicted value.

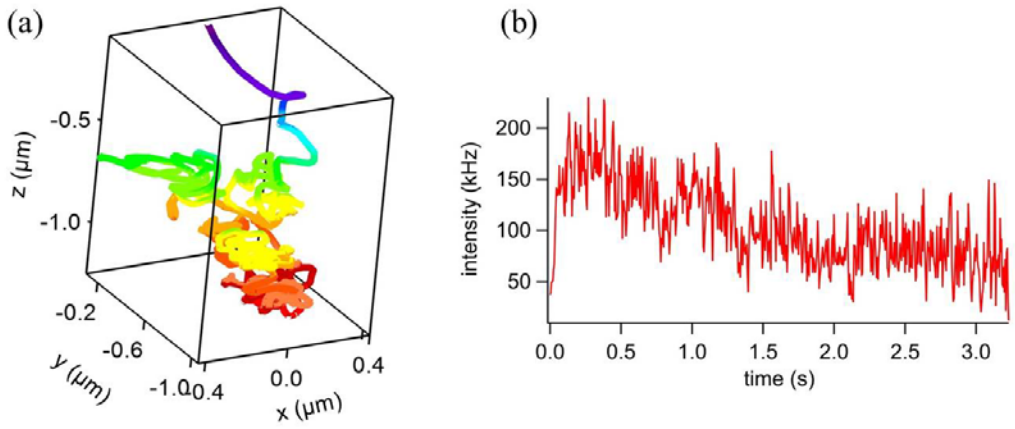

Figure 20. Tracking of a F8783 bead undergoing Brownian diffusion in 90 wt % glycerol (**a**) Rainbow color coded 3D trajectory of a single F8783 bead. The diffusion coefficient (D) predicted by Stokes-Einstein equation is 0.140 $\mu m^2/s$, D derived from mean-squared-displacement analysis[149] of the experimental trajectory is 0.137 $\mu m^2/s$. The trajectory starts in red, ends in purple. (**b**) Photon count rate of the tracked F8783 bead. The bead is gradually photobleached.

2.3.3 Time-correlated single photon counting

By virtue of the single photon counting detector and TCSPS module, we can easily perform antibunching analysis and on-line fluorescence lifetime measurement of the tracked particle.

Fluorescence antibunching is a unique property of a single-molecule emitter. It refers to the phenomenon that a single molecule cannot emit two photons within a time interval shorter than the fluorescence lifetime[150-151]. This simply reflects the fact that after emitting a photon, a single molecule needs to undergo resorption of an excitation photon and radiative decay back to the ground state, before it can emit another photon. Here we

have utilized this property as the ultimate proof that a single fluorescent particle is tracked by our system.

To observe antibunching, single ATTO647N labeled ssDNA (/5ATTO647NN/ CGATAGTATGATGG) are tracked one by one. The time difference between two photons detected by the transmission channel and the reflection channel is repeatedly measured and histogrammed with 128 ps resolution. This photon-pair delay histogram is shown in Figure 21 (a). The dip near zero delay indicates that the probability of the tracked molecules emitting two photons simultaneously is essentially zero. The peaks in the histogram are equally spaced by 100 ns, identical to the reciprocal of the pulsed laser repetition rate. Antibunching behavior exists only when the particle is a single quantum emitter. If that is not the case, *e.g.,* the particle of interest is a fluorescent bead with many organic dyes incorporated, to confirm single-particle tracking, we can compare the photon count rate during tracking with the single particle brightness characterized by a separate FCS experiment.

As a demonstration of lifetime measurement, the fluorescence decay histogram accumulated from 120 Cy5 labeled ssDNA (5'-TTACGGCGATAGTATGAT GGAACC-Cy5-3') tracked in 90 wt % glycerol is shown in Figure 21 (b). The histogram can be well fitted by an exponential decay model with lifetime 1.55 ns.

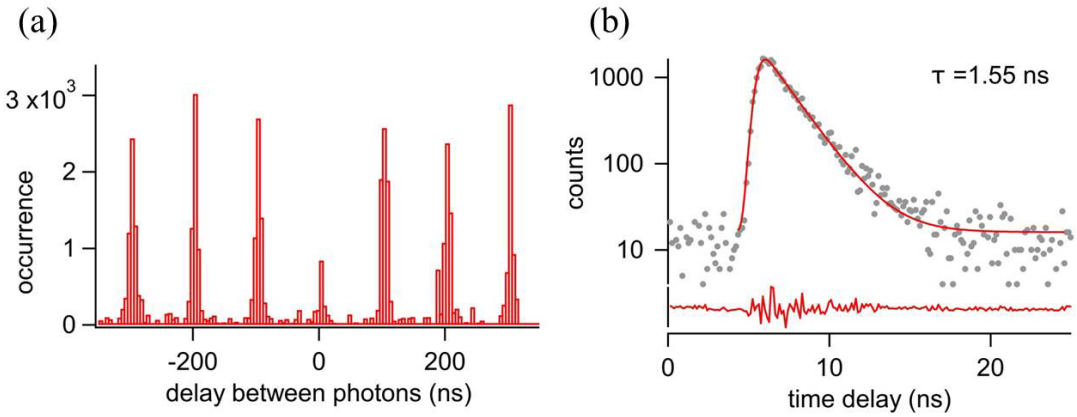

Figure 21. Antibunching and fluorescence lifetime analysis (**a**) Photon-pair correlation histogram obtained from 190 5'-ATTO647N-ssDNA tracks. A Stanford Research DG535 4-Channel Digital Delay Pulse Generator in combination with an inverter and 10 dB attenuator is used to physically delay the reflection channel by 300 ns in the measurement (**b**) Histogram of photon arrival times (grey dots) with respect to the excitation laser pulse, obtained from 120 ssDNA-Cy5 tracks. The histogram is fit to an exponential convoluted with Gaussian instrument response function plus a flat background. The residuals are also shown. The fitted Cy5 lifetime is 1.55 ns.

2.3.4 Tracking duration benchmark

Tracking duration is highly dependent on the target molecule's diffusion rate, emission rate and photostability. To understand the limit of tracking system, it is beneficial to characterize the tracking duration for a variety of fluorescent particles with different diffusion and photophysical properties.

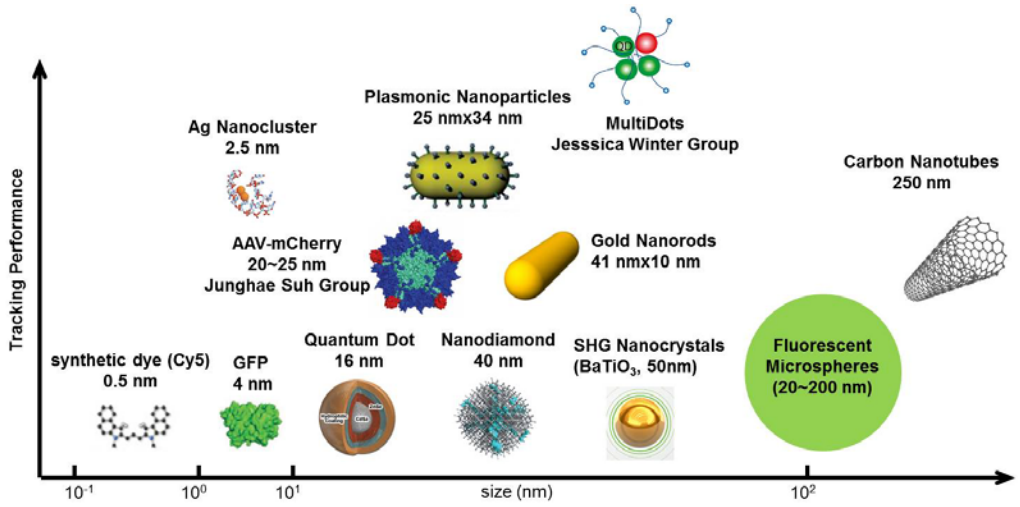

Figure 22. A variety of luminescent particles for single particle spectroscopy in the literature. Unlike fluorescence, the photoluminescence of gold nanorods and SHG nanocrystals is free of photobleaching and photoblinking. Therefore, photoluminescence is theoretically a better candidate than fluorescence particles for optical labeling[152]. However, they require multiphone excitation so we are not able to test them in our lab.

Single organic dye labeled DNA oligos represent a family of fluorescent particles that are most difficult to track. They have relative fast diffusion rate due to the small size, and poor photostability when oxygen scavenger is absent. They are non-spherical, so their diffusion coefficient D cannot be easily estimated from the Stokes-Einstein equation (2.12). In this section, we first explain how we use FCS to quantify D of non-spherical fluorescent particles, using dye-labeled DNA as an example. This method can be applied to other non-spherical particles, including nanodiamonds, nanorods, silver nanocluster, tetrahedral DNA nanostructure, and others (Figure 22). We use 200 nm fluorescent beads (Thermo Fisher F8807) as a reference. The Stokes-Einstein equation predicts its D to be 2.13 $\mu m^2/s$ (η=0.0010049 Ns/m^2) in water, and the characteristic residence time in the focal volume (τ_D) measured by FCS is 15.50 ms. On the other hand, τ_D of 30nt-ssDNA in 90 wt % glycerol is 0.391 ms. Since τ_D is inversely proportional to the diffusion coefficient, D of 30nt-ssDNA is 0.3766 $\mu m^2/s$.

glycerol wt %	Viscosity (Ns/ m^2)	D(μm^2/s)
90	0.22531	0.3766
80	0.061412	1.3817
70	0.023303	3.6412
60	0.011001	7.7131
0	0.0010049	84.4380

Table 2: Diffusion coefficient of 30nt-ssDNA vs. glycerol weight percentage at 20°C. Viscosities are estimated based on parameters in Cheng (2008)[146].

D can alternatively be obtained by mean-squared-displacement analysis of SMT trajectory. Following the procedures in Equation (2.13)-(2.15), D of 9nt-ssDNA in 90 wt % glycerol way is 2.66 μm^2/s (Figure 23).

The dependence of D on molecular weight in is shown in Figure 23. Clearly, there is a negative correlation between them. Actually diffusion coefficient is more about molecular size and morphology.

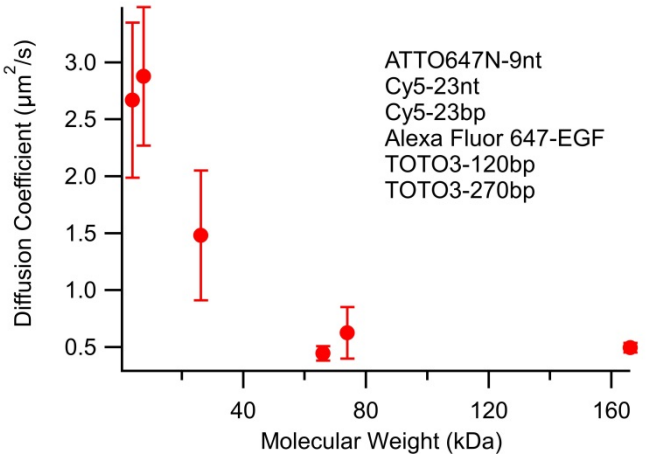

Figure 23. Diffusion coefficient as a function of molecular weight for several fluorescent particles

The longest tracking durations achieved for four types of fluorescent molecules/particles that are mostly used in SMT are shown in Figure 24. Limited by the

photobleaching, Cy5 and ATTO565 can only be tracked for ~3 seconds. 100 nm fluorescent beads can be tracked for longest time because of their slow diffusion and superior photon emission rate.

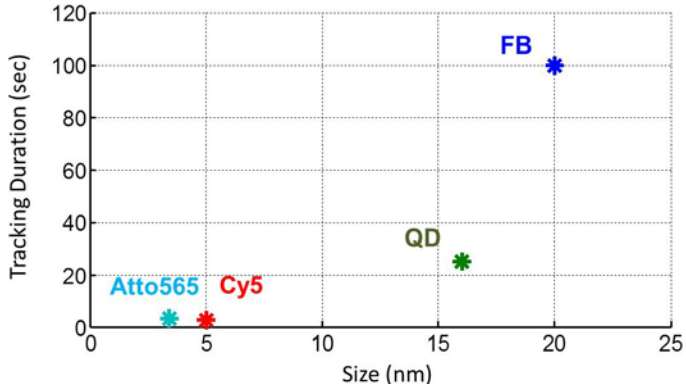

Figure 24. Tracking durations for ATTO565, Cy5, 20 nm quantum dots, and 100 nm fluorescent beads.

2.3.5 Tracking of emerging fluorescent nanostructure

3D nucleic acid-based structures have exhibited properties that are quite different from their linear forms[153-154]. Tetrahedral DNA nanoconstruct (TDN) is one of the most interesting self-assembled DNA nanostructure that has attracted great interest in drug delivery[155] due to its low cytotoxicity, cell permeability, and high resistance to enzymatic degradation in biological media[156]. Its modification versatility also makes it a great candidate for nano-imaging. Here we use TDN to benchmark our tracking capability for multiple organic dye labeled particles.

The TDN particles we used were provided by Prof. Hao Yan in Arizona State University. The particles were self-assembled from 10 ATTO647N labeled ssDNA, such that each vertex and central point of the tetrahedron is attached to an ATTO647N. A 15nt-

ssDNA is tagged which can be used for further DNA binding study. The DNA sequences are listed below.

1. /5ATTO647NN/ TGGCACGCCAGTGTACCACTGTACTTGATTGGCTGAGCGCTTC
2. /5ATTO647NN/ CACACTCTTACGGCTGACCATGAAGCGCTCAGCCAATCAAGTTTACATGCGCAGGACCGCGACT
3. /5ATTO647NN/ ATGGTCAGCCGTAAGAGTGTGTCCACAAGAAGGCGCTCTTCAG
4. /5ATTO647NN/ AGGAACCAGGCGTGTGGAACCTCCTGGACTGTGCCGGAGGTGTAGTCGCGGTCCTGCGCATGTA
5. /5ATTO647NN/ ACACCTCCGGCACAGTCCAGGCCTAGACGGATTCTC
6. /5ATTO647NN/ CATTGTCCTCGGACGGTCCAGCTGAAGAGCGCCTTCTTGTGGTGCCTCTACGGTCGTCTGGCGA
7. /5ATTO647NN/ CAAGGAGCTGGAAGGCCGTGGTCGCCAGACGACCGTAGAGGC
8. /5ATTO647NN/ CCACGGCCTTCCAGCTCCTTGTGGTTCCACACGCCTGGTTCCTCACTCGACTCTCAGAAGTGTC
9. /5ATTO647NN/ CAGTGGTACACTGGCGTGCCAGGATGGAGCTCATATCGGTCTTGACACTTCTGAGAGTCGAGTG
10. /5ATTO647NN/ CTGGACCGTCCGAGGACAATGTAGACCGATATGAGCTCCATCC

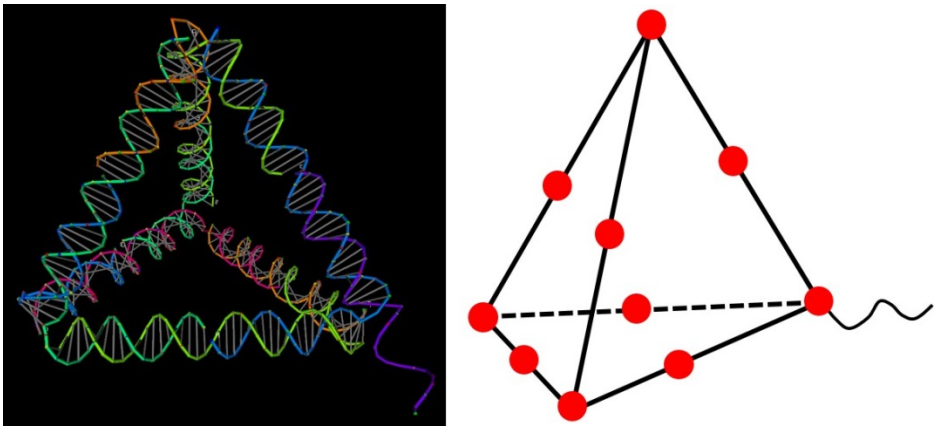

Figure 25. Schematic of the tetrahedral DNA nanoconstruct. TDN has good mechanical rigidity and structure stability. Each red dot represents an ATTO647N dye. The tail is a 15nt-ssDNA that potentially can be used for DNA binding studies.

The 3D trajectory, lifetime trace and photon count rate trace of a single TDN diffusing in 70 wt % dextran is shown in Figure 26. We use dextran, instead of glycerol to

slow down TDN diffusion because glycerol destabilizes the TDN structure[4]. The ATTO647N on the TDN are gradually photobleached. After 25 seconds, the emission rate falls bellows the tracking threshold. Stepwise photobleaching is not observed because of TDN's constant jiggling around the laser focus. The fluorescence lifetime is roughly a constant and consistent with single ATTO647N lifetime.

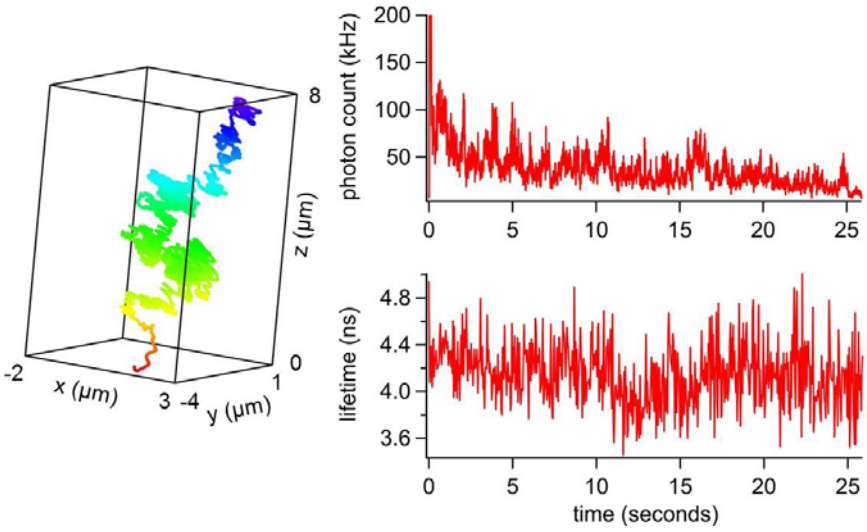

Figure 26. Tracking of single TDN in 70 wt % dextran. The 3D trajectory is rainbow color coded, starting from red, ending in purple. The ATTO647N molecules on the TDN are gradually photobleached. The diffusion coefficient of TDN is 0.59 $\mu m^2/s$.

4 Single TDN brightness in 90 wt % glycerol is measured by FCS to be 2 kHz, suggesting that TDN is completed disassembled. In 70 wt % glycerol, TDN brightness is ~15 kHz, suggesting that TDN is partially disassembled.

Chapter 3: Extend tracking durations[5]

The time scale of molecular biology spans from microseconds (ion channel gating) to minutes (protein diffusion across a cell). Without sufficiently long observation time window, we will not be able to observe minor reaction pathway and stochastic process on a single-molecule level[6]. The observation window (*i.e.* tracking duration) is fundamentally limited by three factors: molecule's diffusion rate, fluorophore photostability, and SNR[7]. In this chapter, we will describe our strategies to extend the tracking duration, targeting on these factors.

3.1 VISCOUS MEDIUM TO SLOW DOWN MOLECULE'S DIFFUSION

Glycerol is highly viscous (its viscosity is 1407 times higher than water) and it has been used to slow down molecule's diffusion in several single-molecule studies[53, 133, 157], including ours. However, glycerol is not completely biocompatible, as it can either stabilize or destabilize DNA duplex dependent on its concentration[158-160]. In our experiment we have found that glycerol destabilize DNA duplex when its concentration is >70 wt %.

In our experiment, DNA duplex is hybridized in house from two ssDNA, one with ATTO633 labeled at 5' end, the other is labeled by a dark quencher Iowa Black® RQ (Figure 27(a)). ATTO633 and Iowa Black® RQ form a FRET pair. The quencher labeled

---

5 Part of this chapter has been published in C. Liu, J.M. Obliosca, Y.-L. Liu, Y.-A. Chen, N. Jiang and H.-C. Yeh, "3D single-molecule tracking enables direct hybridization kinetics measurement in solution," Nanoscale, 9:5664-5670, 2017. I performed the experiments and wrote the manuscript.

6 People may argue that observing a few single molecules for a long period is equivalent to observing many single molecules for a short amount of time, which is only true when the biologicsl system is ergodic. Long observation windows are preferred for another reason: statistical averaging of single molecule data, which typically relies on pre-defined model of the dynamic process, can be avoided.

7 The localization accuracy is determined by SNR. Poor estimates of molecule position make it difficult to reposition the piezo stage correctly and keep the target molecule in the detection volume.

strand has four locked nucleic acids incorporated so that the DNA duplex is predicted to be stable at room temperature (by melting temperature calculation) in standard buffer. However, in 80 wt % and 90 wt % glycerol, the dsDNA exhibits switching between two fluorescence lifetime states (an open and a closed state, Figure 27(b)), suggesting that the dsDNA undergoes conformational change. Multiple lifetime states can also be observed in the lifetime histograms (Figure 27(c)). In 70 wt % glycerol, the histogram can be well fit by a single Gaussian peak. As the glycerol concentration increases, a side peak becomes apparent.

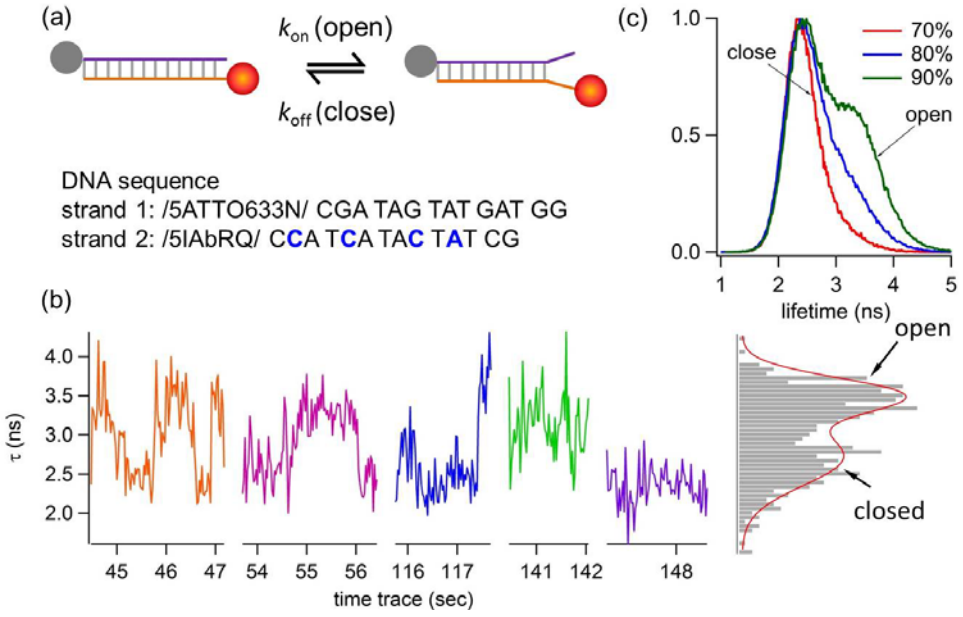

Figure 27. Glycerol destabilizes DNA duplex (**a**) Schematic of the DNA duplex that is labeled by a FRET pair (**b**) Representative single-molecule fluorescence lifetime traces with 25 ms temporal resolution (**c**) Fluorescence lifetime histograms built from single-molecule lifetime traces.

Glycerol is clearly not an ideal medium for biomolecule studies. We have considered dextran as an alternative of glycerol. Dextran is also soluble in water, and it is widely used to apply osmotic pressure to biomolecules; but it raises the DNA melting

temperature[161]. Therefore, we have considered the possibility to develop a glycerol/dextran mixture with neutral effect on DNA molecules. Such a mixture can provide sufficient slowing-down effects without introducing artifact into the DNA kinetics. However, we have found that dextran creates intermediate fluorescence lifetime states which are between unquenched ATTO633 (ssDNA) and quenched ATTO633 (dsDNA). The results are summarized in Figure 28.

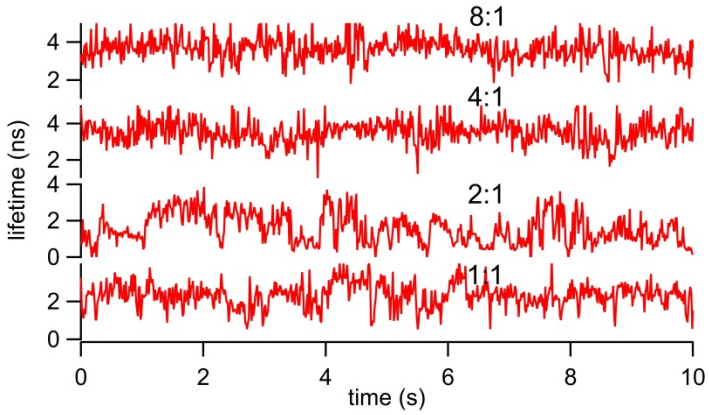

Figure 28. Single-molecule lifetime traces in glycerol and dextran mixture. ATTO633 labeled strand (strand-1) is the reporter and its fluorescence lifetime is quenched upon hybridization with the quencher strand (strand-2). [glycerol+dextran]=90 wt % is fixed, while the ratio between glycerol and dextran is varied. Multiple lifetime states become more pronounced as the dextran concentration goes higher. Strand-1: /5ATTO633N/TGGTCGTGGGGCAACTGGGTTCGCT/3Bio/, Strand-2: /5IABkFQ/CACGACCA

In conclusion, neither glycerol nor dextran is a good candidate for the SMT medium as they may alter the functions and activities of biomolecules under study. To solve the bio-compatibility issue, we have explored a liposome tethering method, which doesn't increase solution viscosity but rather increases the hydrodynamic radius of the target molecule.

3.2 LIPOSOME TETHERING TO SLOW DOWN MOLECULE'S DIFFUSION

Recently Kim et al.[162] reported a liposome tethering approach to slow down Brownian motion that can eliminate the necessities of highly viscous medium (glycerol and dextran for instance). In this approach, fluorescent particles are tethered to freely diffusing liposomes (size can range from tens to hundreds of nanometers[163]) through the biotin-NeutrAvidin interaction (Figure 29). Since the diffusion coefficient of a particle is inversely proportional to its hydrodynamic radius, theoretically the particle's motion can be slowed down significantly.

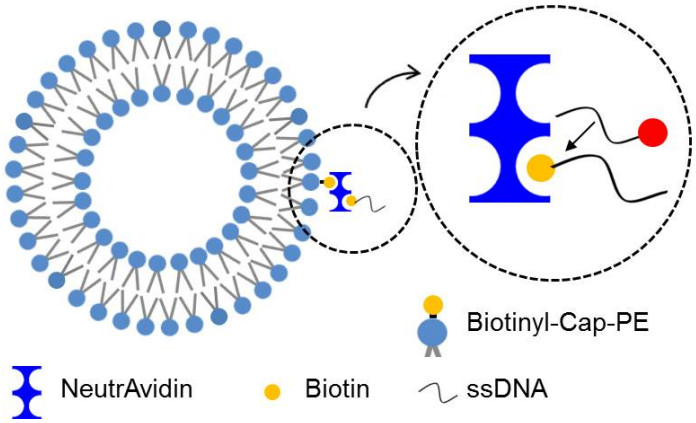

Figure 29. Schematic description of the liposome tethering approach. Tethering of the DNA molecule is achieved through the biotin-NeutrAvidin interaction.

We have followed the protocol in the literature[162] and prepared liposome with the help of Prof. Jeanne Stachowiak group. The slow-down effect of liposome is quantified by the residence time (τ_D) of DNA in focal volume, measured by FCS. As shown in Figure 30, τ_D of DNA with 100 nm liposome tethering is 22 times larger than that without liposome tethering, indicating very effective slow-down. τ_D of DNA with 1 μm liposome tethering, however, is only 4 times larger than that without tethering. This is because the 1 μm liposome concentration (limited by the maximum lipid concentration can be

experimentally achieved) is not sufficient and actually more than 80% DNAs are not liposome tethered. The measured τ_D=1.56 ms cannot reflect the real diffusion rate.

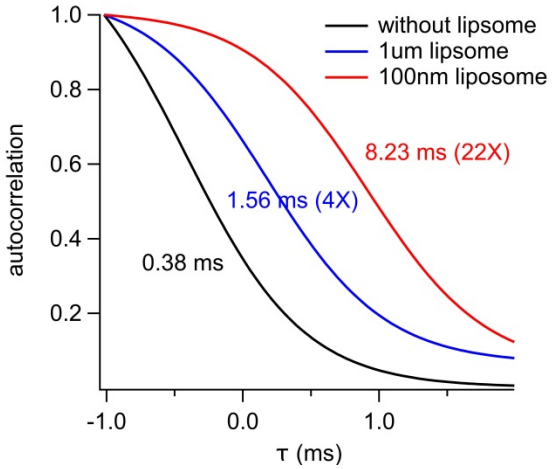

Figure 30. Normalized autocorrelation functions of /5ATTO633N/TGG TCGTGGGGCAACTGGGTTCGCT/3Biotin/ without liposome tethering (black), with 100 nm liposome tethering (red), and 1 μm liposome tethering (blue).

The diffusion coefficient of 5'ATTO633-25nt-biotin3' with 100 nm liposome tethering is measured by FCS (focal volume size calibrated by fluorescent beads) to be 4.6 $\mu m^2/s$, which is 26% larger than 30nt-ssDNA in 70 wt % glycerol without liposome tethering (Table 2). Although the slow-down effect of liposome tethering is not as good as 70 wt % glycerol, the tracking durations in these two cases turn out to be quite similar. Therefore practically 100 nm liposome tethering is a better approach than 70 wt % glycerol in biomolecular studies.

Theoretically photo-protection buffer (*e.g.* PCD/PCA oxygen scavenger, explained in detail in the next section) can increase photostability of the dye and thereby further increase the tracking duration. However, with 100 nm liposome tethering, we did not see

any benefit brought by the photo-protection buffer. This finding indicates that the diffusion rate (4.6 $\mu m^2/s$), instead of photobleaching is the limiting factor of tracking durations.

3.3 OXYGEN SCAVENGER AND SALINE BUFFER

Photobleaching and blinking of fluorophores pose fundamental limitations on the single-molecule fluorescence measurements. Blinking and photobleaching are the result of excited states converting to transient or permanent dark states instead of the ground states. Molecular oxygen (O_2) plays an important role in photostability. On one hand it is responsible for photobleaching via photo-oxidization[164]; On the other hand, it is an efficient quencher of triplet state which is responsible for blinking. Current approaches for improving dye stability typically involve the addition of an enzymatic oxygen scavenger system (*e.g.* PCD/PCA[6] and GOC[120, 159]) as well as chemicals (*e.g.* Trolox) to suppress blinking[165]. Here we have tried to use Trolox (6-hydroxy-2,5,7,8-tetramethylchroman-2–carboxylic acid) in combination with PCD/PCA [8] to eliminate blinking and reduce photobleaching. Although PCD/PCA system did not help to extend tracking duration in >70 wt % glycerol[9], it's not without merit in our single-molecule research. We found that on both an ensemble level and single-molecule level, Cy5-, Alex Fluor 488-, Alex Fluor 647N-, ATTO565-, and ATTO647N-DNA is significantly quenched by certain types of salt in the buffer (Table 3), and the quenching can be fully reversed by the addition of oxygen scavenger (Figure 31 and Figure 32).

This quenching phenomenon is a serious problem because buffers with certain salinity are necessary to maintain the activity of the biomolecules. Surprisingly, this quenching phenomenon has not been reported by any literature, and the exact quenching mechanism is not clear.

---

[8] PCD: protocatechuate-3,4-dioxygenase, PCA: protocatechuic acid. PCD is a multimeric enzyme that catalyze the conversion of PCA to β-carboxy-cis, cis-muconic acid in one step, resulting in the consumption of 1 mole of O2 and the production of two protons per mole of PCA converted.

[9] We suspect that PCD enzyme is inhibited by the high-concentration glycerol. In liposome tethering experiment (glycerol free), the addition of PCD/PCA system did not increase tracking duration because the diffusion rate, instead of the photostability is the limiting factor.

High salt buffer	Tris–HCl[1]	KCl[2]	HEPES+NaCl[3]	sodium phosphate[4]	TAE[5]	TBE[6]
brightness after 5 minutes	79%	48%	42%	45%	87%	87%
brightness after 60 minutes	100%	37%	36%	37%	/	95%

1: 2X, pH 8.0
2: 100 mM
3: 25 mM HEPES + 100 mM NaCl
4: 100 mM, pH 7.2
5: 1X, pH 8.2~8.4
6: 1X, pH 8.2~8.4

Table 3: Brightness of a single ATTO647N-DNA measured by FCS. At t = 0, ATTO647N-DNA is suspended in the buffer. Brightness is normalized relative to the values in DI water. The quenching is permanent except for Tris-HCl buffer.

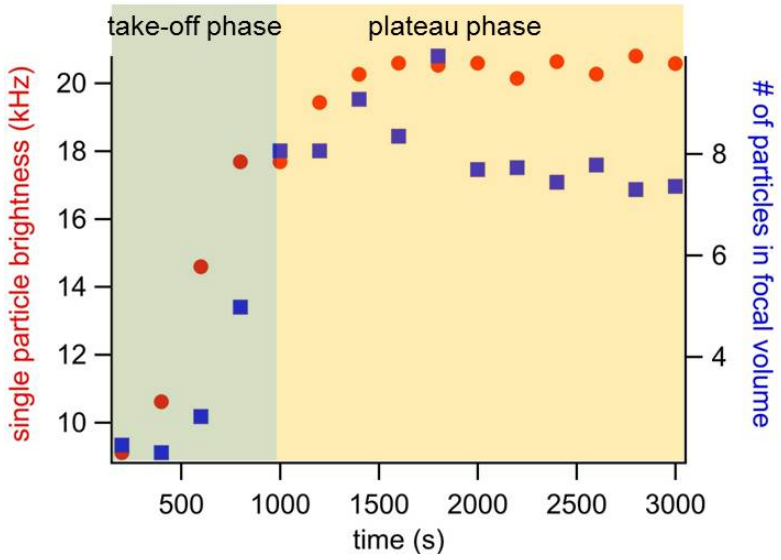

Figure 31. PCD/PCA system can fully rescue the brightness of single ssDNA-ATTO565. At t = 0, the oxygen scavenger is added to the PBS buffer containing ssDNA-ATTO565. After ~17 minutes, ATTO565 is equally bright as in DI water (20.5 kHz in PBS buffer vs. 19.2 kHz in water). The DNA sequence is TTAGTATGAT/3ATTO565N/.

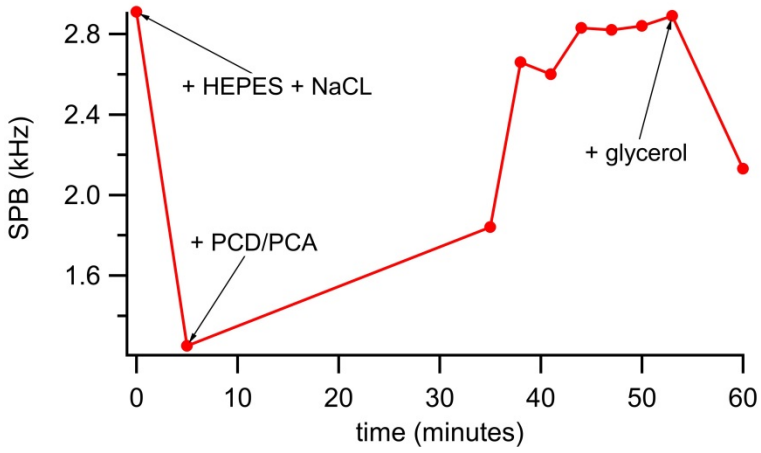

Figure 32. Change of single ATTO647N-DNA brightness over time. The DNA solution contains 25 mM HEPES and 100 mM NaCl. At t=5 minutes, PCD/PCA oxygen scavenger is added to the solution. At t =53 minutes, glycerol is added. The final glycerol concentration is 90 wt %.

Even without oxygen scavenger, the brightness of single ATTO647N can gradually recover with time in Tris-HCl (100% recovery) and TBE (95% recovery) buffer. The results are similar for Cy5- and ATTO633-DNA. To this end, we have identified Tris-HCl as the best buffer for SMT as it provides the largest fluorescence signal intensity.

Chapter 4: DNA hybridization-melting kinetics measurement[10]

Biomolecular binding is one of the most fundamental processes in living systems. It plays critical roles in all corners of biology, such as DNA hybridization, membrane receptor signaling, and transcriptional regulation. Traditionally, molecular binding dynamics can be characterized by FRAP (fluorescence recovery after photobleaching)[166-167], FCS[168-169] and FCCS (fluorescence cross-correlation spectroscopy)[170-173]. Although FRAP, FCS and FCCS can achieve sub-millisecond temporal resolution in monitoring fast dynamic processes, the requirement of time-averaging of multiple events makes these traditional methods difficult in probing short-lived interactions and obtaining statistical properties from a heterogeneous sample[174]. On the other hand, with SMT, one can not only directly observe individual biomolecular binding events, but also recover transient intermediates[8], quantify equilibrium association and dissociation kinetics[26, 72], and characterize static and dynamic disorder[1].

Despite the recent advances in 3D SMT techniques, non-feedback 2D SMT (including wide-field, TIRF, and light sheet microscopy) is still the dominant approach for biomolecular binding detection at the single-molecule level. Instrument complexity could be one reason, but 3D feedback SMT has several more fundamental limitations. First, most 3D feedback SMT (orbital tracking, confocal tracking and TSUNAMI) systems track only one molecule at a time. To get sufficient tracking data for meaningful statistical analysis, a long measurement time is often required, indicating a low throughput at high cost. On

[10] Section 4.1 has been published in C. Liu, Y.-L. Liu, E.P. Perillo, A.K. Dunn and H.-C. Yeh, "Single-molecule tracking and its application in biomolecular detection," IEEE Journal of Selected Topics in Quantum Electronics 22(4): 6804013, 2016. Section 4.2 has been published in C. Liu, Y.-L. Liu, E.P. Perillo, N. Jiang, A.K. Dunn and H.-C. Yeh, "Improving z-tracking accuracy in the two-photon single-particle tracking microscope," Applied Physics Letters 107, 153701, 2015. Section 4.3 has been published in C. Liu, J.M. Obliosca, Y.-L. Liu, Y.-A. Chen, N. Jiang and H.-C. Yeh, "3D single-molecule tracking enables direct hybridization kinetics measurement in solution," Nanoscale, 9:5664-5670, 2017. I performed the experiments and simulations, and wrote the manuscripts.

the other hand, 2D SMT is beneficial for tracking multiple molecules simultaneously and probing interactions among them. Second, compared to the non-feedback 2D SMT microscopes, feedback microscopes often have a lower available photon budget (*i.e.* photon collection efficiency × total number of photons emitted by the molecule before photobleaching), resulting in fewer molecular position estimates. This is due to the fact that the confocal scheme used in the feedback systems has a much lower photon collection efficiency (0.5%–1%) as compared to that of the wide-field microscopy. Although TSUNAMI provides a better collection efficiency by employing the non-descanned, single-detector scheme, two-photon excitation suffers from higher photobleaching rate as compared to one-photon excitation at comparable fluorescence emission rates[175-176].

In this chapter, we first give an overview of biomolecular binding detection methods by traditional 2D SMT. Then we introduce our 3D SMT methods using DNA transient binding as a model system. Two contrast mechanisms, diffusion rate and fluorescence lifetime, can be utilized to sense DNA binding/unbinding events on the confocal tracking microscope. We explain the challenges and our strategies associated with these two mechanisms respectively.

We are interested in the DNA model system because accurate knowledge of nucleic acid (NA) hybridization kinetics in its natural context is critical for understanding the fundamental regulatory functions of small NAs. However, current kinetics measurement techniques are not live cell compatible. Surface plasmon resonance[177-178] and ensemble fluorescence quenching[179-181] are common techniques for annealing and melting kinetics measurements, but these methods requires an externally imposed perturbation (such as rapid mixing[180] or temperature jump[182]) followed by relaxation analysis and thus are generally incompatible with live cell studies. In addition, not at the single-molecule level,

these ensemble methods do not provide information about rare reaction intermediates[8], minor reaction pathways[183] or interaction hot spots[32].

4.1 OVERVIEW OF BIOMOLECULAR BINDING DETECTION USING SMT

Four signatures of biomolecular binding events are usually measured by 2D SMT: colocalization/codiffusion, Forster resonance energy transfer (FRET), localization enhancement, and apparent diffusion rate change. Colocalization and codiffusion are the most commonly used signatures for binding detection at the single-molecule level[8, 26-27, 184-186]. Using the dynamic dimerization of GPCR (G-protein-coupled receptor)[34] as an example (Figure 33(a)): each GPCR monomer in the plasma membrane can be labeled with a fluorescent dye precisely at 1:1 ratio, and imaged as a bright spot on a TIRF microscope. Whether an observed spot represents a single GPCR monomer or a homodimer can be determined from its signal intensity level (or the number of bleaching steps[187]). In the time-lapse sequence of images, the dimerization of GPCR monomers would manifest itself as the colocalization and codiffusion of two monomer spots, whereas the splitting of one dimer spot into two monomer spots signals the opposite process. To detect the association of two different biomolecules, two-color single-molecule imaging can be performed in a similar way[7, 94, 188-190].

Since the molecular size is much smaller than the resolution (~200 nm) of a TIRF microscope, incidental events where molecules reside within 200 nm from each other (called incidental colocalizations) can be misinterpreted as molecular binding. FRET, which occurs only when the donor and acceptor fall within ~10 nm from each other[185], can be used to differentiate these two processes. As shown in Figure 33(b), the binding of YFP-labeled Ras (donor) and BiodipyTR-labeled GTP (acceptor) is detected as the appearance of an emission spot of BiodipyTR-GTP colocalized with the YFP-Ras spot, and the

appearance of BiodipyTR spot correlates with reduced YFP emission[191]. However, no FRET signal does not necessarily mean the absence of protein binding. The donor-acceptor pair and the labeling sites have to be carefully chosen for any FRET based biomolecular binding studies.

The rest two signatures (localization enhancement and diffusion rate change) arise from the fact that biomolecular binding is usually accompanied by the slowdown of the molecule's diffusion. These signatures are often used in studying the association of transcription factor (TF) or RNA polymerase (RNAP) with chromatin DNA, where the TF/RNAP essentially becomes immobile upon DNA binding. Localization enhancement describes the phenomenon that when molecules are imaged with a camera using a long exposure time, fluorescence from the unbound molecules is collected over the entire field of view as these unbound molecules diffuse rapidly. On the other hand, bound molecules emit from a highly localized region, thus giving a signal higher than the auto-fluorescence background over time[4, 110]. By collecting fluorescence images at different exposure times, the residence time of TF/RNAP on chromatin DNA can be precisely determined (Figure 33(c)). Compared with localization enhancement, direct analysis of the molecule's trajectory (*e.g.*, by mean-square-displacement calculation[147], cumulative probability distribution calculation[192-193], hidden Markov modeling[194], and confinement analysis[195]) provides a more quantitative view of the molecular diffusion rate[90, 196] and residence time[110, 197] (Figure 33(d)), which makes it suitable for studying binding processes that involves multiple molecular species and diffusive states[198].

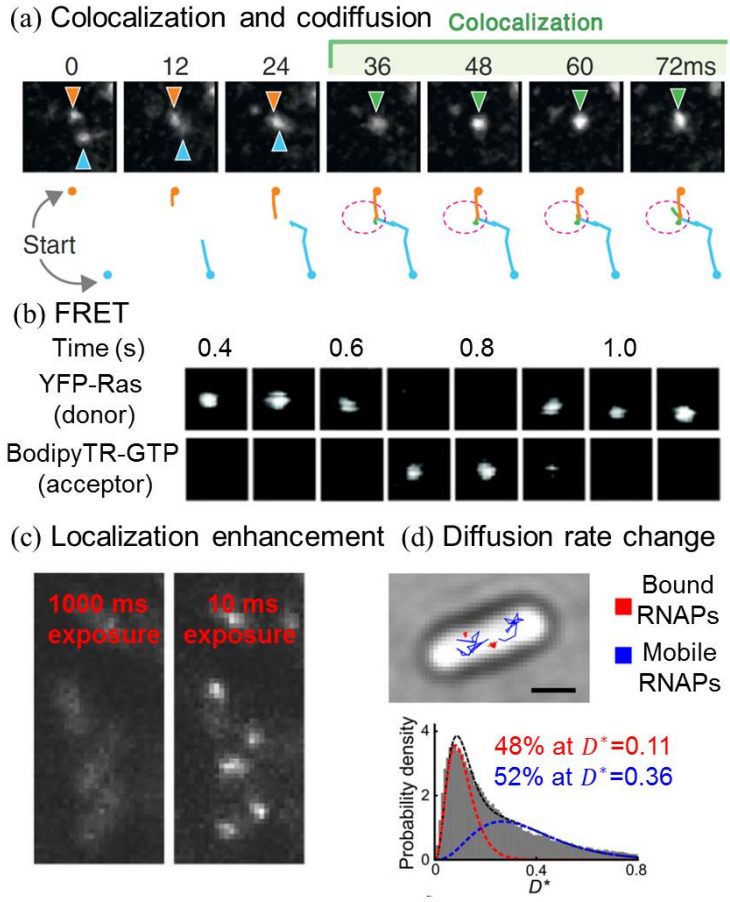

Figure 33. Biomolecular binding detection based on non-feedback 2D SMT. (**a**) Colocalization and codiffusion of binding partners. The image sequence shows two diffusing FPR (N-formyl peptide receptor, a class-A G-protein-coupled receptor) molecules and their trajectories. The two molecules first became colocalized (form FPR dimers) then diffuse together[34]. (**b**) FRET images of single YFP (donor) labeled small G-protein Ras and BodipyTR (acceptor) labeled GTP undergoing FRET upon Ras-GTP binding[191]. (**c**) Localization enhancement. At exposure time of 1000 ms, individual lac repressors (a transcription factor) appear as diffusive background. At 10 ms, they are visible as nearly diffraction-limited spots. The residence time of lac repressor on DNA is determined by obtaining fluorescence images at different exposure times[4]. (**d**) Diffusion rate change. Individual RNAP (RNA polymerase) molecules are categorized as DNA-bound (example trajectories colored in red) or mobile (example trajectories colored in blue) based on their apparent diffusion coefficients *D**calculated from mean-squared-displacement (MSD) of their trajectories. The distribution of *D** can be fitted with two diffusing species (*i.e.* DNA-bound and mobile)[196].

4.2 DIFFUSION RATE AS THE CONTRAST MECHANISM

Biomolecular interactions are usually accompanied by modification in size and hence diffusion rate. Theoretically molecular motion can be a general and yet specific contrast mechanism to detect molecular binding. However, to distinguish molecules by their diffusion rates with traditional FCS, the diffusion times must differ by at least a factor of 1.6 for comparable fluorescence signal[199]. Unfortunately, quite a number of important processes do not produce such a large change in molecular weight (~1.6^3=4 fold change). For example, the formation of a dimer from two monomers leads to a change of diffusion coefficient of only 25%[200]. On the other hand, the high spatiotemporal resolution data provided by SMT allows for more sophisticated and thorough analysis of molecular motion. In this section, we will apply state-of-the-art single-molecule trajectory analysis algorithm to molecular binding detection, and identify the challenges and solutions associated with SMT techniques.

4.2.1 Simulation framework and algorithm benchmarking

Our simulation is based on a DNA hybridization-melting kinetics model (Figure 34), which involves tracking of an ATTO647N-labeled single-stranded DNA (ssDNA, 10 nt) in the presence of its unlabeled complementary strand (10 μM) in solution. With proper ionic strength, 10-bp complementary region results in transient binding at room temperature. ssDNA and dsDNA exhibit different diffusion coefficients in solution. Transitions between binding and unbinding states can be analyzed using a hidden Markov model.

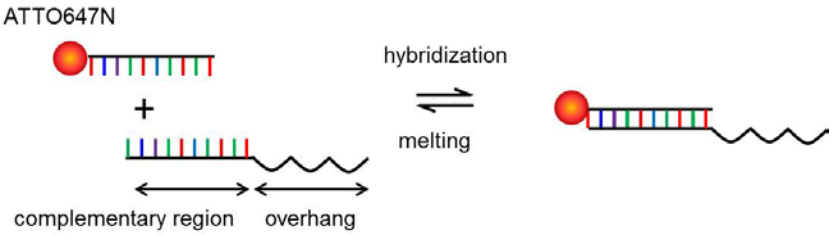

Figure 34. A tracking simulation model: hybridization and melting of an ATTO647N-labeled DNA system. A variable-length overhang region allows us to tweak the diffusion rate change upon DNA hybridization.

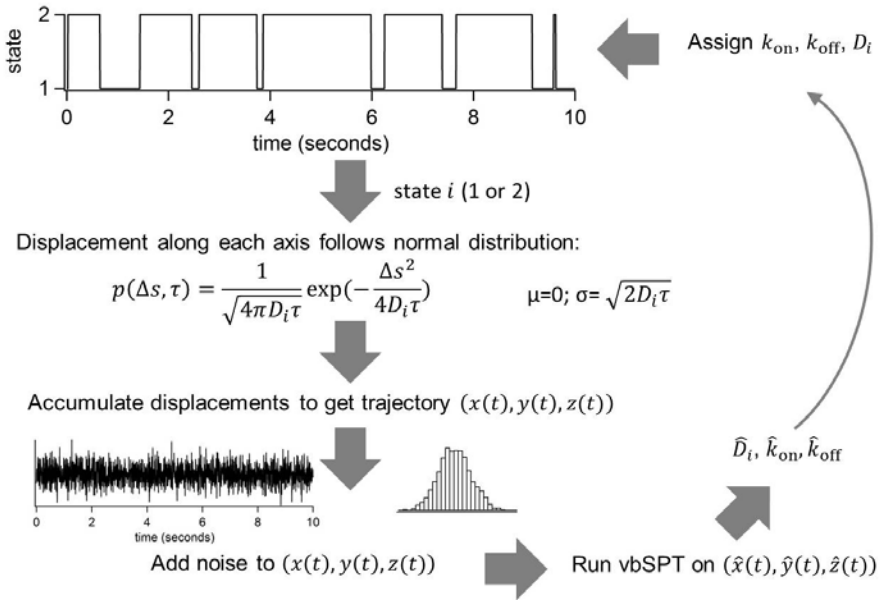

Figure 35. Flow chart of DNA transient binding kinetics simulation. The DNA hybridization and melting process is modeled as a Markov chain.

We first compare the kinetics estimated by vbSPT and traditional Baum-Welch algorithm. The predefined parameters in this simulation are as follows: k_{on}=2.99s^{-1}, k_{off}=0.7s^{-1}, D_1=1.6 μm^2/s, D_2=0.2 μm^2/s. Tracking errors are assumed to be zero. As shown in Figure 36, the Baum-Welch algorithm is not convergent due to short duration (0.2

seconds) of the single-molecule trajectories, whereas vbSPT converges to the true values because of its capability to combine the information content in short tracks.

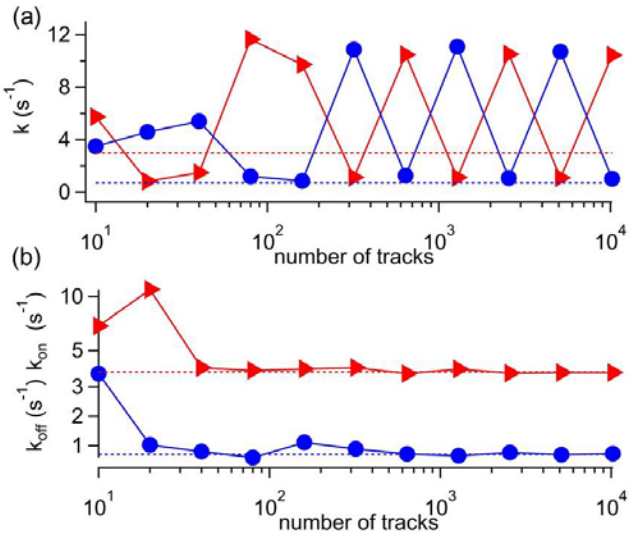

Figure 36. Comparison of k_{on} (red) and k_{off} (blue) estimated by the Baum-Welch algorithm and variational Bayes algorithm. The tracking duration is 0.2 seconds. Dash line represent the true values of k (**a**) The Baum-Welch estimates of k never converge to their true values no matter how many tracks are analyzed (**b**) The variational Bayes estimates of k converge to the true values for an increasing number of tracks.

Next, we benchmark vbSPT performance as a function of diffusion rate difference between the ssDNA and dsDNA, and the number of tracks available. In this simulation, Gaussian noise (σ_x=25.7 nm, σ_y=25.7 nm, σ_z=81.5 nm, experimentally characterized values) is added to the trajectory to better approximate reality. The results are shown in Figure 37. vbSPT cannot differentiate the two diffusive states when the relative difference of D is less than 10%. When the relative difference is more than 100%, a few thousand trajectories are sufficient to estimate the kinetic rates within ±5% error of the true values.

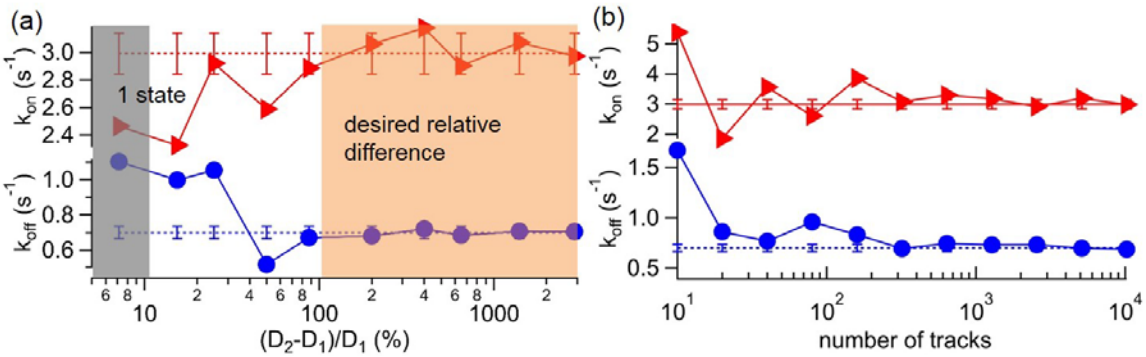

Figure 37. Variational Bayes estimates of transition rates k when trajectories have Gaussian noise. Tracking duration is 0.2 seconds. (**a**) D_2=3 μm^2/s is fixed, D_1 is varied and hence the relative difference between these two diffusion coefficients. 3,000 tracks are analyzed. When the relative difference is less than 10%, vbSPT cannot differentiate the two diffusive states (gray area). When the relative difference is larger than 100%, k estimates are within ±5% error of the true values (orange area). (**b**) Estimates of k as a function of number of trajectories analyzed. The diffusion coefficients are fixed (D_1=1 μm^2/s, D_2=3 μm^2/s).

4.2.2 Discrepancy between simulation and experiment

In the previous sections, we have developed a theoretical framework for DNA transient binding rate measurement using diffusion rate as the contrast mechanism. The feasibility and robustness of the framework is proved by simulation. However, vbSPT cannot correctly determine the number of diffusive states in experimental single DNA trajectories, even though the experimental condition satisfies the prerequisite identified from the previous section (significant difference in diffusion coefficients and a large number of trajectories). We speculate that the reason causing this discrepancy is that the white Gaussian tracking error assumed in simulation is unrealistic.

In single-particle tracking, the localization errors are often modeled as white Gaussian noise[11] when studying the effects of localization errors on the particle behavior

[11] White Gaussian noise is an idealization of real-world noise that satisfies the following criteria: the noise at each time moment is random (and hence uncorrelated) and follows the same Gaussian distribution. White Gaussian noise is an i.i.d. (independent and identically distributed) sequence.

interpretation (*e.g.* free diffusion or confined diffusion)[33, 147, 201]. While the white Gaussian noise model greatly simplifies the mathematical analysis of localization errors, the white Gaussian noise assumption may not be true in the real tracking experiments.

So far most SMT literature merely demonstrate that their tracking errors are normal distributed [12] and disregard the temporal properties of the errors. In fact, with close examination, we found many of the published single-particle trajectories[50-51, 51-52, 55, 191] show notable temporal correlation in their tracking errors. We believe it is the temporal correlation of experimental tracking errors that leads to questionable results in binding kinetics measurements.

To test this hypothesis and solve the correlation problem, we develop a new tracking algorithm termed maximum likelihood estimation, or MLE. MLE is supposed to provide better molecule position estimation at each time step and hence reduce the temporal correlation of tracking errors. In section 4.2.3, we describe how MLE works and why it is predicted to outperform our current error signal analysis (ESA) algorithm. In section 4.2.4, we will prove that temporally correlated tracking errors make the current trajectory analysis tools perform poorly and the MLE tracking scheme alleviates this problem by generating temporally uncorrelated tracking errors.

4.2.3 Maximum likelihood estimation of molecule position

Using MLE for particle position estimation, Sahl and coworkers have previously achieved 2D single-particle tracking with xy-localization error as small as 10-20 nm[202]. MLE finds the most likely position of the emitter by comparing the recorded photon counts in the four detectors $\vec{I} = [I_1, I_2, I_3, I_4]$ with a 3D reference map $\vec{R}(x, y, z) = [R_1(x, y, z), R_2(x, y, z), R_3(x, y, z), R_4(x, y, z)]$, where $R_i(x, y, z)$ denotes the photon

[12] They do so by Gaussian-fitting the histogram of the tracking errors and presenting the R^2 values.

counts in the *i*-th detector when the reference emitter is located at position (x, y, z). Such a 3D reference map $\vec{R}(x, y, z)$ can either be established by optical modeling, or established experimentally by raster scanning the excitation tetrahedron with an immobilized fluorescent nanoparticle (*i.e.* the reference emitter) while recording the four signal intensities as a function of the particle's position. $\vec{R}(x, y, z)$ is further normalized such that $\sum_{i=1}^{4} R_i(x, y, z) = 1$. For a given emitter position (x, y, z), the probability of detecting I_i photons in the i-th time detector follows Poisson distribution (where R_i is the expected value and the variance):

$$p_i\left(I_i; R_i \mid x, y, z\right) = \frac{(R_i(x, y, z))^{I_i}}{I_i!} \exp\left(-R_i\left(x, y, z\right)\right) \tag{4.1}$$

The likelihood of detecting $\vec{I}$ photons at a position (x, y, z) with $\vec{R}(x, y, z)$ expected photons on average is given by the product of the above probabilities:

$$L(\vec{I}; \vec{R} \mid x, y, z) = \prod_{i=1}^{4} p_i(I_i; R_i \mid x, y, z) \tag{4.2}$$

The most likely position of the emitter is thus the location where this likelihood L is maximized, or equivalently where the log-likelihood is maximized[202]:

$$(\hat{x}, \hat{y}, \hat{z}) = \underset{(x,y,z)}{\operatorname{argmax}}[\sum_{i=1}^{4} I_i \ln(R_i(x, y, z))] \tag{4.3}$$

In each time step, we search for a position (x, y, z) that maximizes the log-likelihood $[\sum_{i=1}^{4} I_i \ln(R_i(x, y, z))]$ and uses that to represent the emitter's position.

MLE should outperform ESA because ESA has a fundamental flaw in its z-position estimate – the cross-talk between the lateral and axial directions is not accounted for in the analysis. MLE, on the other hand, uses all the information available for position estimate which takes any possible cross-talk into account.

4.2.4 MLE reduces temporal correlation

To investigate the temporal properties of tracking errors, we plotted the autocorrelation functions[203] $C(\tau)$ of white Gaussian noise, ESA z-tracking error and MLE z-tracking error in Figure 38(a), and fitted them with a single exponential decay model[204] (Ae^{-t/τ_0}). As expected, the autocorrelation function of zero-mean white Gaussian noise (C_{GAU}) asymptotically approaches a delta function, showing no temporal correlation at all. Similar to C_{GAU}, the autocorrelation function of the MLE z-tracking error (C_{MLE}) decays rapidly, with a temporal correlation length τ_0 = 0.36 (in units of time steps). On the contrary, C_{ESA} decays slowly with τ_0 = 2.06. To understand the whiteness of the z-tracking errors, their power spectral densities[205] (PSD) were plotted and compared (Figure 38(b)). Ideal white noise has a constant PSD. Both autocorrelation and PSD analyses indicate that the z-tracking error from the MLE scheme is a better approximation of white Gaussian noise.

Temporally uncorrelated tracking errors can be crucial for the reliable recovery of molecular kinetics from 3D SMT data. We have verified this hypothesis using DNA hybridization and melting kinetics as a model system. In our simulations, transition between the hybridized state (D_{h} = 0.15 μm^2/s) and the melted state (D_{m} = 0.30 μm^2/s) is a memoryless process, with a rate constant k_{on} = 2.99×10^5 M^{-1}s^{-1} for hybridization and a constant k_{off} = 0.7 s^{-1} for melting. The tracking duration varies from 0.5 s to 1.5 s, limited by the photostability of the fluorescent tag. A hidden Markov model (HMM) is adopted to model the random switch between the two diffusive states[72, 194, 206], and a 3D variational Bayes method (vbSPT[198]) is used to determine the hybridization-melting kinetics (*i.e.* k_{on} and k_{off}) from downsampled 3D trajectory data. Here downsampling of the raw trajectory data (time step δt = 5 ms) is just an additional step to further decorrelate tracking errors at the expense of worse effective temporal resolution.

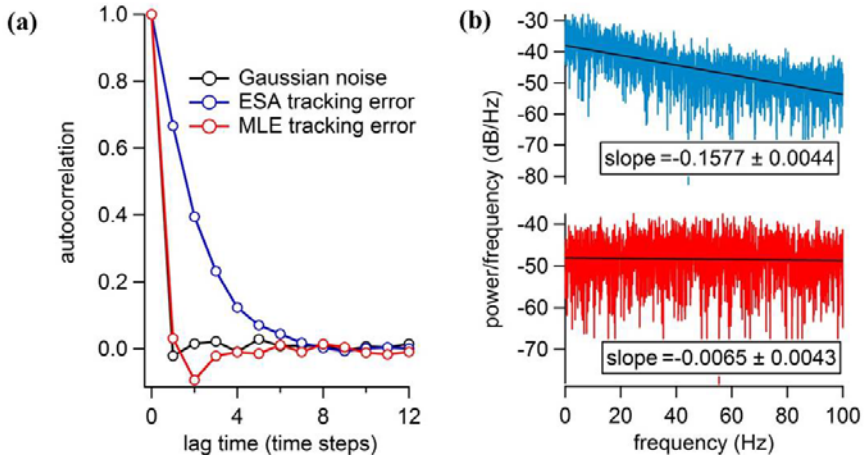

Figure 38. Quantification of temporal correlation in tracking error **(a)** Normalized autocorrelation functions of zero-mean white Gaussian noise (C_{GAU}, black), ESA z-tracking error (C_{ESA}, blue) and MLE z-tracking error (C_{MLE}, red). The autocorrelation function $C(\tau)$ of error $e(t)$ is defined as: $C(\tau) = \langle \delta e(t) \cdot \delta e(t+\tau) \rangle / \langle e(t) \rangle^2$, where $\langle\ \rangle$ represents averaging over time and $\delta e(t) = e(t) - \langle e(t) \rangle$. **(b)** Power spectral densities of ESA z-tracking error (blue) and MLE z-tracking error (red). The fitted slopes are also shown in inset (coefficient value ± one standard deviation). A constant power spectral density is the characteristic of white noise. In this simulation, the diffusive particle (D = 0.5 μm^2/s) is tracked for 20 seconds. Each time step is 5 ms.

The relative errors of $\hat{k}_{on}$ and $\hat{k}_{off}$ (estimates of rate constants) are functions of effective temporal resolution ($\Delta t = N \cdot \delta t$, $1/N$ is the downsampling ratio), number of tracks, and tracking duration (Figure 39). Consistent with previous reports[198], the relative errors of $\hat{k}_{on}$ and $\hat{k}_{off}$ monotonically decrease with increasing number of tracks and tracking duration. Without any downsampling (Δt = 5 ms), the relative errors of $\hat{k}_{on}$ are over +70% for ESA tracking (Figure 39(b)) and in a range of +20% to +40% for MLE tracking (Figure 39(c)). These large positive relative errors are predominantly caused by the temporal correlation of the tracking errors, which can be reduced by downsampling. Using a downsampling ratio of 1/2 (Δt = 10 ms), the relative errors of $\hat{k}_{on}$ fall within ±5% for MLE tracking. On the other hand, even though a downsampling ratio 1/7 is used (Δt = 35 ms), the relative errors of $\hat{k}_{on}$ are still biased and over +12% for ESA tracking. In other

words, MLE tracking offers both better molecular kinetics estimation and higher effective temporal resolution.

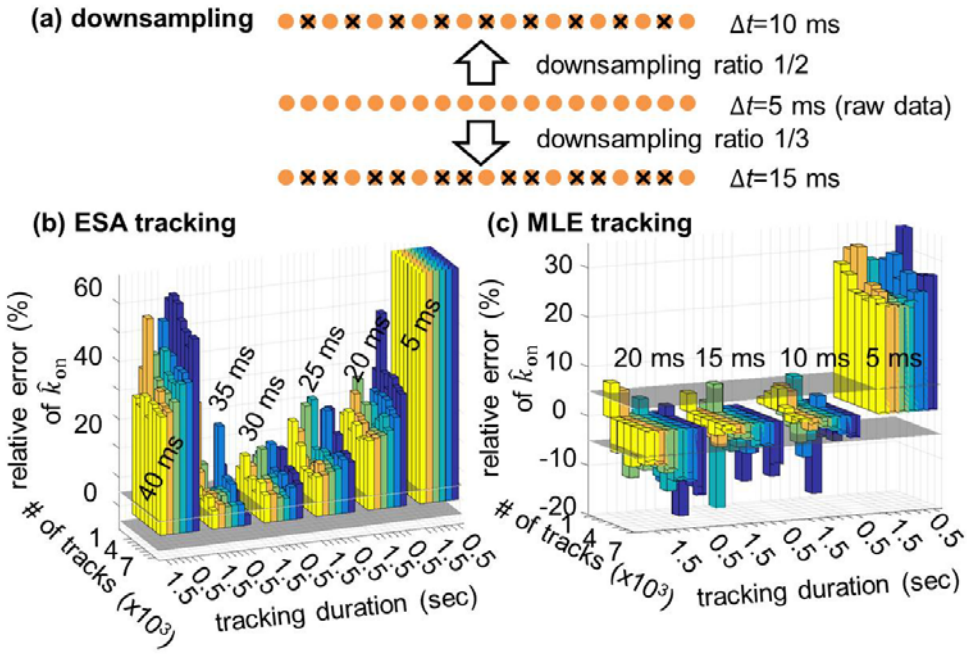

Figure 39. Comparison of ESA and MLE in terms of kinetic rates estimation accuracy **(a)** Downsampling of the raw trajectory data. Raw trajectory data have a temporal step size Δt = 5 ms. Downsampling ratios of 1/2 and 1/3 result in Δt = 10 ms and Δt = 15 ms, respectively. Downsampled trajectories are then analyzed by the 3D variational Bayes method (vbSPT)[198] in order to discern the binding-unbinding kinetics ($\hat{k}_{on}$ and $\hat{k}_{off}$) of the tracked particle. **(b)** Relative error of $\hat{k}_{on}$ derived from ESA-based trajectories. **(c)** Relative error of $\hat{k}_{on}$ derived from MLE-based trajectories. In this simulation, the number of tracks and track duration are varied to assess the convergence of vbSPT. Each bar represents one vbSPT analysis of 1,000-7,000 trajectories, with bar height showing the relative error of $\hat{k}_{on}$ and bar color encoding tracking duration (0.5 s – purple, 0.7 s – dark blue, 0.9 s – light blue, 1.1 s – green, 1.3 – orange, 1.5 s – yellow). The horizontal grey planes are where the relative error equals $\pm$5%. The 6 bar groups in (**b**) correspond to $\hat{k}_{on}$ obtained from 6 different downsampling ratios, whose Δt are integer multiples of 5 ms. Similarly the 4 bar groups in (**c**) correspond to $\hat{k}_{on}$ obtained from 4 different downsampling ratios.

4.2.5 MLE increases tracking accuracy

By virtue of MLE, the z-tracking accuracy is enhanced by 1.7 fold (Table 4). While the z-tracking error is still larger than the xy-tracking error, their relative difference is reduced from 129±23% to 33±4%. Besides, the relative error for the calculated diffusion coefficient is decreased from 14±1% to less than 2%. The improvement of the z-tracking accuracy can be clearly seen in the z-tracking error histograms (Figure 40). Both histograms can be well described by a Gaussian distribution, with mean approximately equal zero. Comparing the two tracking schemes, MLE clearly gives a narrower z-tracking error distribution (σ = 50.2 nm vs. 93.9 nm) and a better diffusion coefficient estimate ($\widehat{D}$ = 0.50 $\mu m^2/s$ vs. 0.47 $\mu m^2/s$).

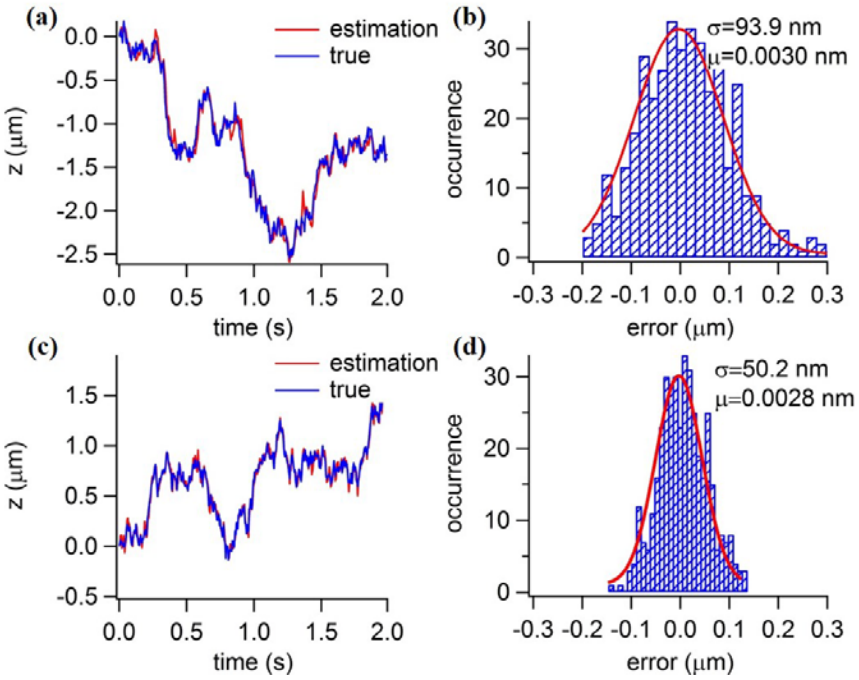

Figure 40. Representative z trajectories and tracking error distribution. **(a)** and **(b)**: ESA tracking. **(c)** and **(d)**: MLE tracking. The red curves represent the estimated z trajectories while the blue curves represent the true z trajectories of the diffusive particle. In this simulation, the diffusive particle (D = 0.5 μm^2/s) is tracked for 2 seconds, and 250 of 2-second-long trajectories are used to build the histograms. The standard deviations of the fitted Gaussian curves are 93.9 nm (ESA) and 50.2 nm (MLE), respectively. The diffusion coefficients calculated from the mean-squared-displacement analysis are 0.47 μm^2/s and 0.50 μm^2/s, respectively.

	Method	XY	Z	$\widehat{D}$ (μm^2/s)
D=0.5 μm^2/s	ESA	42.9	87.6	0.42±0.06
	MLE	38.7	50.7	0.51±0.06
D=1.0 μm^2/s	ESA	53.4	123.8	1.14±0.13
	MLE	55.6	72.8	1.00±0.11
D=1.5 μm^2/s	ESA	65.7	164.7	1.76±0.20
	MLE	69.0	95.5	1.53±0.18

$\widehat{D}$ is the estimation of true diffusion coefficient D
ESA: error signal analysis
MLE: maximum likelihood estimator

Table 4: Tracking errors of different position estimation algorithms

4.2.6 Discussion and conclusion

Both enhanced z-tracking accuracy and less temporally correlated z-tracking errors can contribute to the improved molecular kinetics estimation shown in Figure 39(c). To understand their relative importance, we have tested two scenarios in simulations: (**a**) the z-tracking errors are kept small but they are temporally correlated; (**b**) the z-tracking errors are large but they are temporally uncorrelated. By comparing the relative errors given by the MLE-based tracking and the scenario (**a**) (Table 5), we have found that more precise kinetics estimation in MLE-based tracking cannot be solely explained by better z-tracking accuracy. On the other hand, by comparing the relative errors given by the ESA-based tracking and the scenario (**b**), we have found that the quality of kinetics characterization can be dramatically improved solely by making the tracking error less correlated over time, even when the tracking error amplitude remains the same. Therefore, decorrelation of z-tracking error plays a critical role in reliable recovery of molecular kinetics.

	Relative error of $\hat{k}_{\mathrm{on}}$ (%)
MLE-based tracking	42
Scenario (a)	133
ESA-based tracking	3388
Scenario (b)	155

Table 5: Relative errors of k_{on} estimates for different types of tracking error

In conclusion, we have developed a maximum likelihood estimator (MLE) that can improve the z-tracking accuracy by 1.7 fold, without sacrificing the xy-tracking accuracy. MLE outperforms the traditional ESA tracking scheme mainly because ESA has a fundamental flaw in its z-position estimate—the cross-talk between the lateral and axial direction is not accounted for. MLE, on the other hand, uses all the information available for position estimate (including any possible cross-talk), therefore resulting in a much

smaller z-tracking error. We believe that the less temporally correlated z-tracking error found in MLE tracking is also a result of its better position estimate in each time step. With less temporally correlated tracking error, precise hybridization-melting kinetics of a DNA model system have been recovered from thousands of short trajectories *in silico*. Our preliminary implementation of the MLE algorithm on a quad-core Windows PC suggests that MLE can be run in quasi real time (<1ms), and potentially can be further accelerated by dedicated field-programmer gate array (FPGA). Our approach can be readily applied to other feedback-driven SPT techniques which suffer from the large z-tracking error and the temporally-correlated-tracking-error issues. This work demonstrates that temporally uncorrelated tracking error is as important as small tracking error, and binding-unbinding kinetics cannot be correctly characterized without first examining the temporal properties of tracking/localization errors.

4.3 FLUORESCENCE LIFETIME AS THE CONTRAST MECHANISM

Intensity-based FRET has been extensively used in 2D biomolecular binding detection as reviewed in Section 4.1. However, it cannot be readily applied to feedback SMT due to the effective excitation intensity fluctuation caused by molecule's residual diffusion. Here we adopt an intensity-independent approach to the measurement of FRET. The goal of this work is to recover the annealing rate (k_{on}) and melting rate (k_{off}) of single DNA molecules from the fluorescence lifetime traces obtained in free solution. The experiment involves tracking the reporter strand (5' labeled with ATTO633, 50 pM) in the presence of a high concentration (0.2-1 μM) of its complementary quencher strand (5' labeled with Iowa Black® FQ). Dark quenchers are dyes with no native fluorescence. By labeling the complimentary strand with dark quencher instead of fluorescent dyes, the complimentary strands concentration can be much higher, which offers the possibility to probe weak nucleic acid interactions.

4.3.1 Experimental details

With the TCSPC (time-correlated single photon counting) module, we can time tag photons with 128 ps resolution and group them into consecutive time windows (Figure 41 top right). After properly compensating the time delays among the four detection channels (see Appendix A.5), a single fluorescent decay histogram is built for each time window by accumulating the photons collected in all detectors. The fluorescence lifetime for each window is then fitted by the maximum likelihood estimator[207-208]. In our experiments, ~130 photons ($\mathrm{SNR} \approx 1.4$) are sufficient for lifetime estimation. This leads to a temporal resolution of 15 ms in monitoring the lifetime change of tracked molecules. The single-molecule lifetime trace can be merged with the molecule's 3D trajectory to provide spatiotemporally resolved binding/unbinding kinetic information of the tracked molecules.

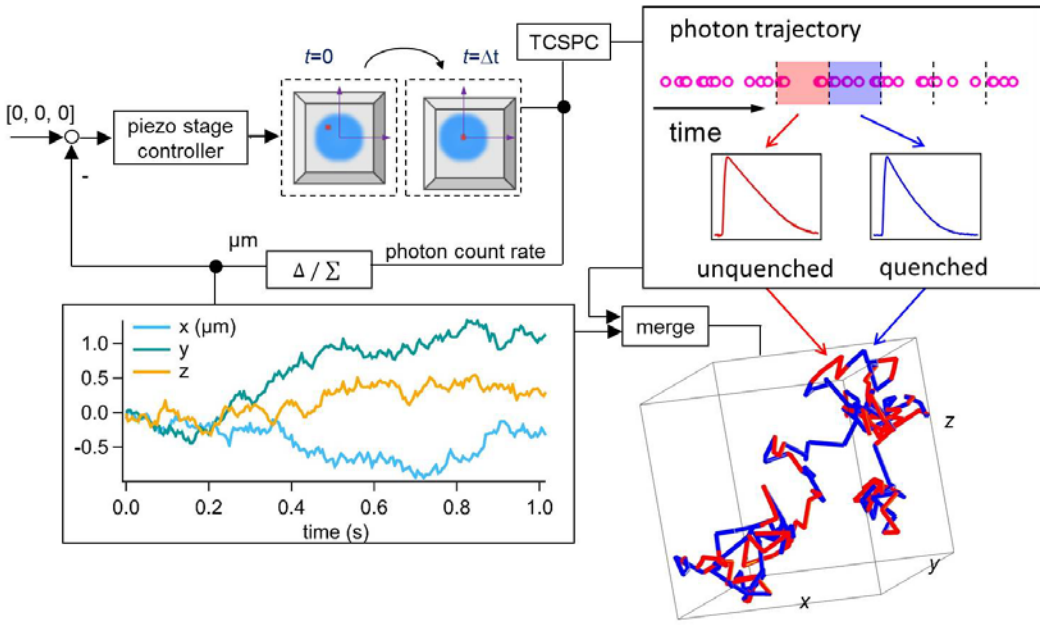

Figure 41. Diagram of our spatiotemporally resolved single DNA annealing-melting kinetics measurement (**Top left**) The diffusion of the fluorescent molecule in 3D space is compensated by repositioning the xyz piezo stage every 5 ms, so that the molecule can be locked in the center of the Gaussian laser beam. (**Bottom left**) A 3D trajectory of 5'ATTO633-labeled 8nt-ssDNA in 70 wt % glycerol (**Top right**) The per-photon time-tagged information from the TCSPC module is used in post-processing to generate fluorescence lifetime trace at 15-ms time window. Since the lifetime of the reporter strand is reduced upon hybridization with its Iowa Black® FQ-labeled complementary strand, the observation of multiple switching between two lifetime states (red: unquenched state; blue: quenched state) is expected. (**Bottom right**) The fluorescence lifetime trace is then mapped onto the 3D trajectory, providing not only the temporal but also spatial information of annealing-melting events that take place along the 1015-ms trajectory.

Figure 41 bottom right panel shows such a merged 3D trajectory of a 5'ATTO633-labeled 8nt-ssDNA (reporter strand-1 in Table 6) freely diffusing in 70 wt % glycerol and transiently hybridizing with its complementary strands. The trajectory is color coded with two distinct fluorescence lifetime. The longer lifetime (unquenched ATTO633) corresponds to the ssDNA state, whereas the shorter lifetime (quenched ATTO633) indicates the dsDNA state. The annealing-melting events can be clearly observed along this merged 1-second trajectory.

We characterized the quenching efficiency at various donor-quencher separation distances (Figure 42(b)). As molecules with large diffusivities are difficult to track for a long time, we slow down the diffusion of DNA by running the tracking experiment in 70 wt % glycerol solution.

Five representative lifetime traces of tracked single reporter strands are shown in Figure 42(c). The black lines indicate the binary state (ssDNA or dsDNA) sequences identified by ebFRET[209], a MATLAB library for analyzing single-molecule FRET time series with hidden Markov model (HMM). The digital switch between the two lifetimes is only seen in the presence of quencher strands.

The lifetime histogram built from these traces can be well fitted by two Gaussian distributed peaks (Figure 42(d)), centered at 2.41 ns and 3.60 ns respectively. The 3.60 ns lifetime, presumably given by the unquenched ATTO633 on reporter strand-1, is shorter than the 4.16 lifetime of the same strand measured in 20 mM Tris-HCl pH 8.0 buffer at the ensemble level. Two factors may contribute to this discrepancy. First, the addition of glycerol in SMT experiments decreases the lifetime by increasing the refractive index of the solution, as suggested by the Strickler Berg equation[210-211]; Second, the background fluorescence (lifetime<600 ps) from Iowa Black® FQ can bias the fitted lifetime towards a smaller value. As ensemble measurements require a stable 8-bp duplex at room temperature, locked nucleic acids (LNA) are incorporated in the duplexes for ensemble lifetime characterization. LNA may significantly change the relative orientation between the dye and quencher transition dipole moments, which can possibly explain why the quenched-state lifetime measured in SMT is also different from the value (2.01 ns) in Figure 42(b).

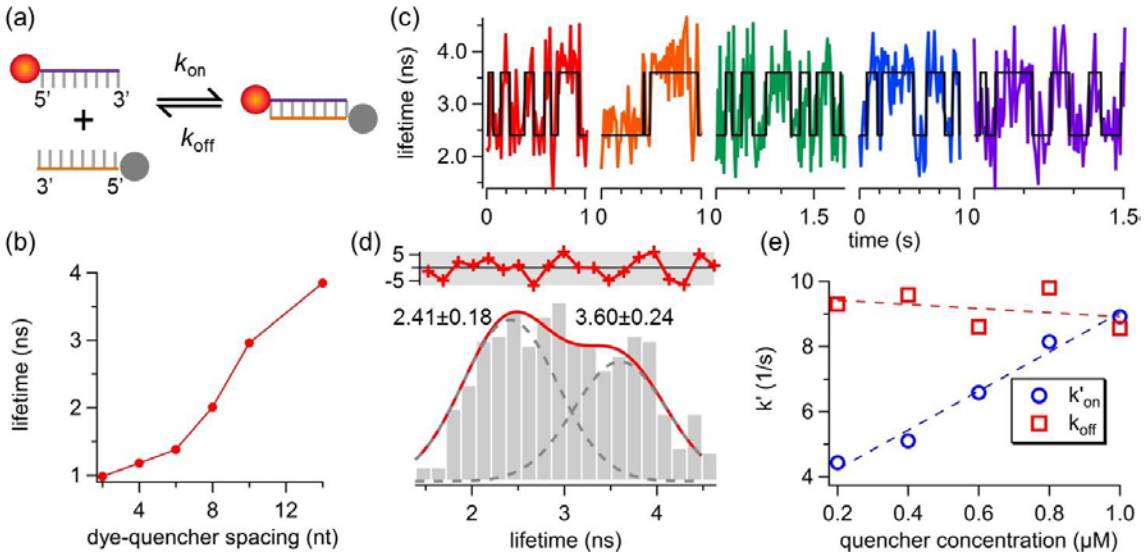

Figure 42. Reporter lifetime and estimated kinetic rates (**a**) The reaction scheme of the donor-quencher system. The reporter strand is a 5'ATTO633-labeled 8nt ssDNA. The quencher strand is a 5'-Iowa Black® FQ-labeled ssDNA that is complementary to the reporter. Iowa Black® FQ is selected as the dark quencher due to its absorption peak at 532 nm, so that ATTO633 is only partially quenched upon duplex formation. (**b**) The fluorescence lifetime of ATTO633 as a function of its spacing from the dark quencher, measured from ensemble experiments. ATTO633's lifetime drops from its native 4.16 ns to 2.01 ns (dsDNA) when the dye-quencher distance is 8 bp. (**c**) Representative single-molecule lifetime traces of reporter strand-1 in 70 wt % glycerol at room temperature. The quencher strand concentration is 0.6 μM. Transient annealing and melting events are clearly manifested as the digital switch of fluorescence lifetime. (**d**) The lifetime histogram built from the lifetime traces in (**c**) also shows two states (3.60 ± 0.24 ns and 2.41 ± 0.18 ns, R^2=0.87). The red curve in the upper panel shows the residuals from the two-peak Gaussian fit. (**e**) Apparent annealing (k'_{on}) and melting rates (k_{off}) extracted by ebFRET[209]. Dashed lines indicate linear fits. k_{on}, the slope of the linear fit of k'_{on} vs. quencher concentration is identified to be 5.13 ± 0.42 $M^{-1}s^{-1}$ (k_{on}). k_{off} is identified to be 9.55 ±0.64 s^{-1}.

To find out the annealing (k_{on}) and melting (k_{off}) rates of single freely diffusing DNA molecules, we conducted 3D-SMT of reporter strands at five different quencher strand concentrations (from 0.2 μM to 1 μM). As shown in Figure 42(e), the apparent annealing rate (k'_{on}) recovered by ebFRET is proportional to the quencher strand concentration ($k'_{on}=k_{on}\cdot$[quencher strand]), while k_{off} is roughly invariant. This result

reflects the fact that the DNA annealing process is essentially a pseudo first-order reaction (since the quencher strand concentration is >4,000-fold higher than that of the reporter strand), while the melting is a zero-order reaction. We have successfully characterized k_{on} (5.13×10^6 $M^{-1}s^{-1}$), k_{off} (9.55 s^{-1}), and K_a (0.54 μM^{-1}) of the 8-bp model duplex system diffusing at 4.8 $\mu m^2/s$. It has been previously shown that k_{on} measured in 3D solution is 3 to 4-fold higher than that measured on a 2D lipid film[212]. As expected, our kinetics values are 1.5 to 3-fold higher than chose measured by surface-based techniques[213-215].

4.3.2 ebFRET algorithm benchmark

A major challenge in SMT-based DNA hybridization kinetics measurement is that the track duration, which is limited by the SNR, dye photostability, and molecule's diffusivity, is usually shorter than the average dwelling time of the molecule in a certain state (either ssDNA or dsDNA). Therefore, most single-molecule lifetime traces fail to show any or show only one state transition. The information they provide is too little for conventional HMM algorithms (*e.g.* Hammy[216], vbFRET[217], QuB[218]) to recover the transition rates between the two states.

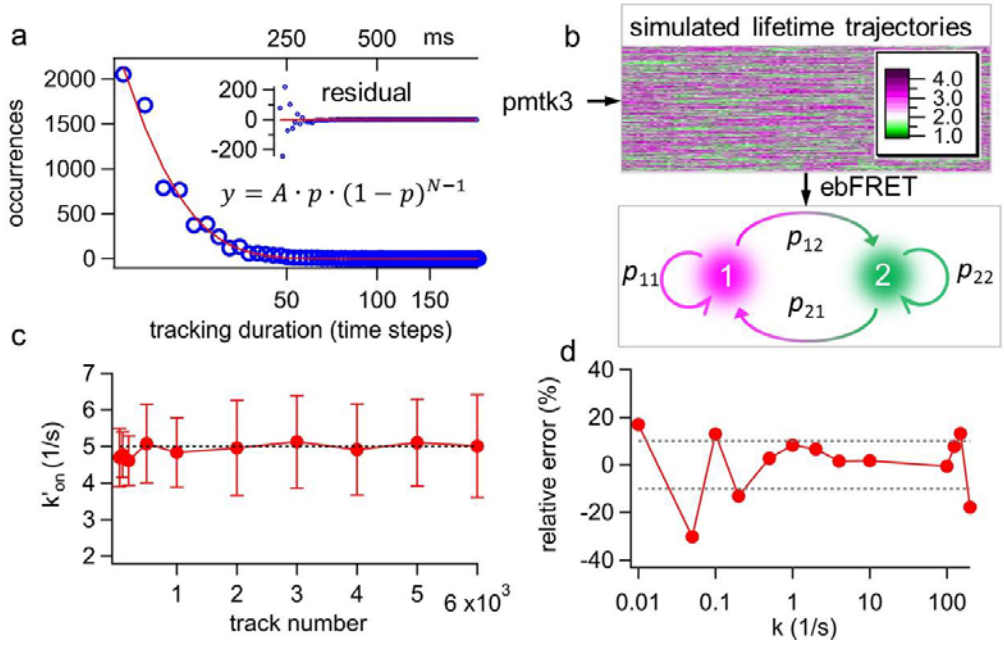

Figure 43. Benchmark ebFRET by simulation (**a**) The experimental track durations are found to follow a geometric distribution with p=0.13 (p is the probability of losing track of the molecule for each time step, N is the number of time steps before the molecule is lost). (**b**) Based on estimated p from (**a**) and preset annealing-melting rates, we generate thousands of simulated lifetime traces of various lengths using the MATLAB toolkit pmtk3. The lifetime traces are further processed by ebFRET to estimate the transition matrix, and hence k'_{on} and k_{off}. (**c**) Estimated k'_{on} vs. the number of lifetime traces used by ebFRET. The true k'_{on} is preset to be 5 s^{-1}. The error bars are calculated from the standard deviation of the transition matrix, which is also estimated by ebFRET. (**d**) 2,000 lifetime traces produced by a wide range of kinetic rates (k'_{on}= k_{off} = k) are processed by ebFRET. The relative error of estimated k as a function of the preset k (k'_{on}=k_{off}= k) is shown.

We have found that the ebFRET algorithm provides an elegant solution to this challenge. The experimental track durations can be modeled by a geometric distribution (Figure 43(a)), with the probability of tracking the molecule successfully for each time step equals to 0.87. Based on this probability, preset k'_{on} and k_{off}, a number of fluorescence lifetime traces are generated and fed to the ebFRET (Figure 43(b)). Since ebFRET only reports the estimated transition matrix (unitless) instead of the kinetic rates (s^{-1}) of our interest, a conversion from the transition matrix to rates is needed. Based on the relation

shown in Equation (4.4)-(4.6), annealing (k_{on}) and metling rate (k_{off}) can be derived from Equation (4.7)-(4.8).

$$p_{12} = \frac{k_{on}}{k_{on} + k_{off}}[1 - e^{-(k_{on}+k_{off})\Delta t}] \tag{4.4}$$

$$p_{21} = \frac{k_{off}}{k_{on} + k_{off}}[1 - e^{-(k_{on}+k_{off})\Delta t}] \tag{4.5}$$

$$p_{11} = 1 - p_{12}, \quad p_{22} = 1 - p_{21} \tag{4.6}$$

$$k_{on} = -\frac{p_{12}\ln(1 - p_{21} - p_{12})}{(p_{12} + p_{21})\Delta t} \tag{4.7}$$

$$k_{off} = -\frac{p_{21}\ln(1 - p_{21} - p_{12})}{(p_{12} + p_{21})\Delta t} \tag{4.8}$$

In Figure 43(c), the preset kinetic rates (k'_{on}=5 s^{-1}, k_{off}=10 s^{-1}) are fixed, while the number of lifetime traces generated for ebFRET analysis are varied. Estimated k'_{on} converge rapidly to the ground truth and the relative error is less than 4% when 500 traces or more are used. The conclusion is similar for k_{off}. On the other hand, k'_{on} estimated by vbFRET[217] doesn't converge to the true value.

In addition, ebFRET offers a broad dynamic range for rate estimation – ebFRET can recover k with less than 10% error when k is within 0.5-125 s^{-1} and 2,000 lifetime traces are used for analysis (Figure 43(d)). This 250-fold dynamic range is more than one order of magnitude higher than that of vbFRET. We emphasize that 2,000 traces is a practical number as they can be collected experimentally within one hour. Our simulation results prove that the integrated 3D-SMT and ebFRET method can discern kinetics (0.5-125 s^{-1}) with average dwelling time that is even shorter than the lifetime monitoring temporal resolution (15 ms), and longer than our track duration (expectation value = 115 ms).

4.3.2 Results and discussion

A number of buffer and strand conditions are known to affect the DNA annealing and melting rates, including salt[219-220], glycerol concentration, and GC content. To further validate the capability of our method, we have measured the kinetics of reporter strand-1 at different glycerol and Tris-HCl buffer concentrations, as well as the kinetics of another reporter strand (reporter strand-2) with less GC content. The results are summarized in Table 6. As expected, decreasing the Tris-HCl concentration from 20 mM to 4 mM reduces the association constants K_a of reporter strand-1 by 3.2 fold (from 0.54 μM^{-1} to 0.17 μM^{-1}), which can be explained by a smaller k_{on} and a larger k_{off}. Dependent on the salt and glycerol concentration, glycerol can either stabilize[158] or destabilize[159-160] DNA duplex. Here we show the duplex stability was significantly reduced (a 13-fold reduction in K_a of reporter strand-1) when glycerol concentration is increased from 70 wt % to 80 wt %, which is dominantly attributed to a significant decrease of k_{on} (from 5.13 to $0.45\times10^6 M^{-1}s^{-1}$). On the other hand, the less GC content affects the dsDNA stability mainly through an increase of k_{off}, which is consistent with reports published earlier[72].

reporter	sequence (5' to 3')	Tris-HCl buffer	glycerol conc.	k_{on} ($10^6 M^{-1}s^{-1}$)	k_{off} (s^{-1})
reporter strand-1	ATTO633-TGGGCGGG	20 mM	70%	5.13±0.40	9.55±0.64
		4 mM	70%	3.63±0.66	21.60±0.40
		20 mM	80%	0.45±0.05	10.99±2.0
reporter strand-2	ATTO633-TGATTGTG	20 mM	70%	5.65±0.56	15.71±1.98

Table 6: Annealing and melting rates of two reporter strands at different salinity and glycerol concentration

It should be noted that with the typical μM or less concentration of probe, the heat from radiation-less decay is too small to effect the temperature of the solution. (http://www.chempep.com/ChemPep-Generic-Term_Fluorescent_Dyes.htm)

4.3.4 Protein induced fluorescence enhancement

In the previous sections, we described a FRET-based method for biomolecule interaction detection. This method requires mutagenesis or chemical modification of both the partners involved in the interaction, and the decrease of reporter's photon emission rate upon molecular association makes it more difficult to be tracked. Recently, an alternative single-molecule assay termed protein induced fluorescence enhancement (PIFE) is developed in Myong's lab[221]. PIFE refers to the photophysical effect that a Cy3 becomes brighter when a protein approaches its vicinity. The underlying mechanism is that the protein reduces the cis-trans isomerization of Cy3 by increasing the effective medium viscosity, resulting an enhancement of the quantum yield as well as fluorescence lifetime[222-223].

Cy5 shares a similar chemical structure with Cy3 and also undergoes cis-trans isomerization[224]. Although Myong group has shown that Cy3 exhibits a 1.9-fold increase of brightness when its distance from a protein is 1 base pair[221], so far the applications of PIFE are only limited to Cy3. In this section, we explored the possibility of utilizing the PIFE effect of Cy5 for DNA transient binding detection.

The protein in our study is BamHI restriction enzyme (Thermo Fisher 15021-023, 2000 unites), which recognizes G^GATCC site on a dsDNA and cut best at 37 °C. The dsDNA is hybridized in house from the following two strands: 5'-Cy5-TGGATCCATAGTAGCGTAGCGTAGCGTAGCGTAGCGTAGC-3' and 5'-Biotin-

GCTACGCTACGCTACGCTACGCTACGCTACTATGGA-3'. BamHI binding site is in close proximity with Cy5. The reaction schematic is shown in Figure 44.

Figure 44. BamHI binding site on a Cy5 labeled dsDNA

We perform single-molecule tracking of the dsDNA in the buffer containing BamHI, 50 mM Tris-HCl, and 10 mM $CaCl_2$. Calcium is used in place of magnesium to prevent BamHI-mediate cleavage. Unfortunately, very few PIFE events were observed in the experiment (Figure 45).

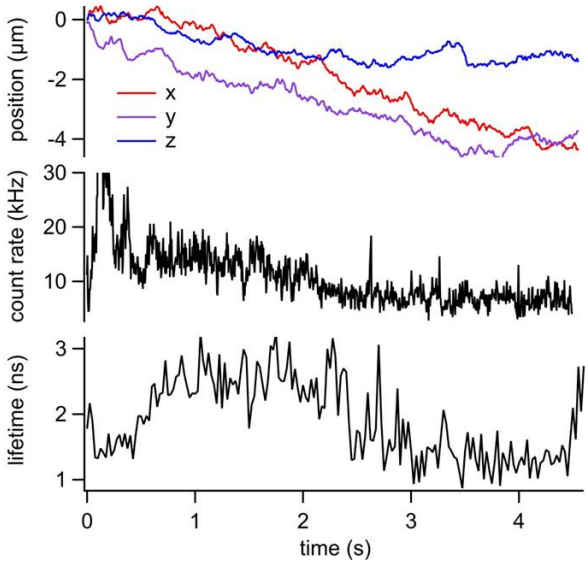

Figure 45. Overserving PIFE effect by SMT. Fluorescence lifetime of Cy5 increases by ~1.8-fold when BamHI binds to the dsDNA. The photon count rate trace is not perfectly correlated with the lifetime trace due to the Brownian motion of dsDNA under study. Only 3 PIFE events are observed in 40,000 single-molecule trajectories. The solution contains 70 wt % MW=40,000 dextran.

We repeated the experiment in 50 wt % and 60 wt % glycerol with three different BamHI concentration (0.075 U/μL, 1 U/μL, 3 U/μL). Not a single PIFE event was observed. To test BamHI activity in highly viscous solution, we conducted gel electrophoresis in 0%, 10%, 20% and 50% dextran with or without the presence of BamHI enzyme. The results are shown in Figure 46.

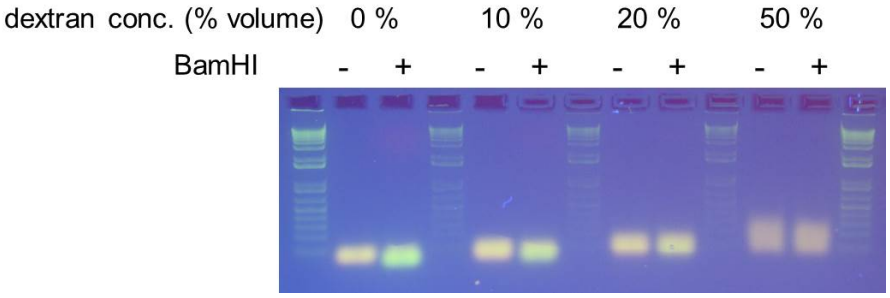

Figure 46. Gel electrophoresis of the Cy5-labeled dsDNA with or without BamHI in various concentrations of dextran. If BamHI is fully functional, Cy5 will be cut out from the dsDNA and the band shows purely green, the color of DNA intercalating dye. If Cy5 is not cut out, the band shows an orange color, which is in part contributed by the red color of Cy5.

4.4 LIMITATIONS AND OPPORTUNITIES

Although we have successfully recovered the transient binding kinetics rates from the DNA model system, there are several limitations in this work:

(1) The tracking duration is so short that a combined analysis of multiple (typically a few thousand) trajectories is necessary to yield accurate estimates of the kinetics rates. This statistical averaging approach is somewhat equivalent to an ensemble measurement, making the observation of minor reaction pathway very difficult if not impossible.

(2) A hidden Markov model is presumed to describe the DNA transient binding process. Our combined analysis method cannot be directly applied to non-Markov biological process.

(3) The solvent (glycerol) affects the DNA binding/unbinding kinetics. The rate constants measured from our experiment do not reflect their properties in the biological condition, despite that our results are comparable to the literature.

(4) The fluorescence lifetime change detection approach puts an upper limit (~1 μM) on the concentration of quencher-labeled complementary strands, since the quantum yield of the quencher is not zero. In fact, 5 uM Iowa Black® FQ gives us a background fluorescence of 3.3 kHz (4 channels combined) at 640 nm excitation, which makes the SNR only 4. Iowa Black® RQ is even worse (144 kHz for 5 uM), since it has direct absorption of the laser light. The concentration limitation prevents us from probing weak biomolecular interactions.

(5) The throughput is low since we can only track one molecule at a time. An estimate of k_{on} and k_{off} requires a total experiment time >30 hours.

To overcome these limitations, a greatly extended physical bandwidth is desirable: we need better temporal resolution as well as longer tracking duration. Ideally, we should be able to track a small dye-labeled molecule in buffer containing no viscous medium, for a time period only limited by the photostability of the dye. There is no silver-bullet solution, but we can improve the system for in vitro studies from the following aspect(s): (1) Place another objective orthogonal to the existing objective for z-position sensing. The working distance of the new objective has to be long enough to bypass the physical constraints posed by the existing objective. (2) Achieve isotropic point-spread-function by spatial light modulation and stimulated emission depletion[145]. (3) Employ a 2D laser scanning and single-photon encoding method similar to Moerner, (2014)[72] to increase the temporal resolution of lateral position tracking. The xy trajectory will be analyzed to extract useful information, while z tracking only serves to prevent the molecule from escaping the detection region.

Chapter 5: Quantification of rare single-molecule species[13]

Fluorescence techniques have fundamentally changed the way that we study complex biological and chemical systems as they not only enable sensitive, real-time observation of the systems but also allow for precise quantification of specific entities inside the systems. Among various fluorescence emission signatures that can be used for quantification[225], fluorescence lifetime is an intrinsic property of fluorophore that does not depend on the experimental factors such as excitation intensity, photon collection efficiency, and fluorophore concentration[226-227]. As a result, fluorescence lifetime can be a reliable means to distinguish various fluorescent species down to the single-molecule level[18, 183, 228-233]. One potential application of identifying single molecules by their lifetimes is in DNA sequencing[228-230]. Whereas single fluorophores can also be classified simply based on their excitation and emission wavelengths[234], such detection often requires an instrument with multiple excitation sources and detection channels[235]. On the other hand, distinct fluorophores with similar spectral properties but different lifetimes can be measured one-by-one in a flow stream using only one excitation source and a single detection channel.

5.1 EXPERIMENT DESIGN

Enderlein *et al.* has previously demonstrated the discrimination of single R6G and TRITC molecules in a continuous flow by analyzing the fluorescence decay of individual emission bursts recorded[230]. The misidentification probabilities of the single fluorophores were very high (~20%) due to the small number of photons per burst (~50) that could be used for lifetime estimation. This is because in a typical flow system the time for a

13 Part of this chapter has been previously published in C. Liu, A. Rastogi and H.-C. Yeh, "Quantification of rare single-molecule species based on fluorescence lifetime," Analytical Chemistry, 89 (9): 4772–4775, 2017. I built the mathematical model and wrote the manuscript.

fluorophore to traverse the detection volume is on the order of 1 ms[229]. Although single-molecule identification accuracy can be improved by a correlative measure of fluorescence burst size and fluorescence lifetime (together with time-gated background reduction)[228-229], only ~90% identification accuracy was achieved this way. While the misidentification rate can be significantly reduced if the same molecule is allowed to flow through the detection volume multiple times (*e.g.* repeat sequencing of identical DNA strands that are fluorescently labeled and enzymatically digested[228]), it is difficult to perform this type of repetitive detection on a random biological system using only a conventional microfluidic and confocal apparatus.

Here we show that a freely diffusing fluorophore can be tracked in solution by a custom-made, confocal-feedback 3D single-molecule tracking system, enabling single-molecule interrogation time to be extended from 1 ms to more than 60 ms (Figure 47). Although an extended observation window can also be achieved by tethering the molecule of interest to a surface[234] or trap it in a confinement[20, 72], such methods require tedious preparation steps and cannot be applied to classify single molecule species inside a living system. Using only lifetime as the basis for molecular identification, the significantly extended observation window provided by our tracking system leads to a molecular identification accuracy (MIA) greater than 95% in a two-component system.

While many creative ways are currently under development to further enhance the molecular identification accuracy, we ask ourselves two questions: (1) what is the adequate molecular identification accuracy that enables precise quantification of a rare molecular species embedded in a sea of a major species (for instance, 1 in 10^3), and (2) what is the minimum number of single-molecule tracks required to reach a preset confidence level in molecular quantification? As precise quantification of rare molecular species is crucial in many aspects of chemical, biological and medical research (such as detection of rare

genetic mutations for early cancer diagnosis[236]), analytical solutions to this type of problems are needed.

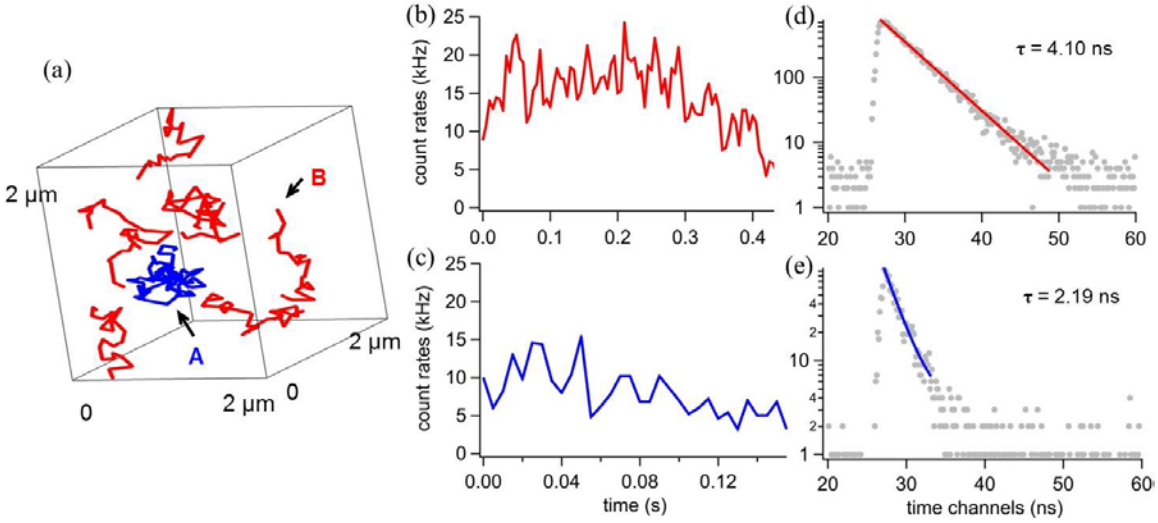

Figure 47. 3D SMT based fluorescence lifetime classification. (**a**) Representative molecular trajectories of the two types of fluorescent molecules A and B in solution. (**b**), (**c**) Emission time traces of selected B and A molecules, respectively. (**d**), (**e**) Corresponding fluorescence decay curves of the tracked B and A molecules. Here the A species is the quenched ATTO633 dye and the B species is the unquenched ATTO647N dye.

5.2 STATISTICAL MODELING

Here we show the derivation of the analytical solutions to these questions. We assume that in our two-component model system we have fluorophores A and B with two distinct lifetimes (τ_A and τ_B). The molecular ratio of A to B is a:b, where A is the rare species (a/b<<1). Our fluorescence lifetime classifier (a maximum-likelihood estimator[208]) has the following confusion matrix:

	Actual A	Actual B
Predicted A	α	$1-\beta$
Predicted B	$1-\alpha$	β

where α and β are the lifetime-based molecular identification accuracies for A and B respectively. Using the burst integrated fluorescence lifetime (BIFL) analysis method, Seidel's group has previously demonstrated the identification and quantification of two dyes with different fluorescence lifetimes in a mixture[233]. Because the standard deviation of the fluorescence lifetime depends on the number of analyzed photons ($\sigma \sim 1/\sqrt{N}$)[237], the quantification accuracy of Seidel's method is limited by the short observation window of the flow-through detection scheme. Here we use quenched ATTO633 dye (A species) and unquenched ATTO647N dye (B species) as our model system. Measured by the 3D tracking system, the A and B species have average photon count rate/lifetime of 8.02 kHz/2.11 ns and 14.60 kHz/3.87 ns, respectively. When the observation window is 5 ms, standard deviations of the lifetime measurements are 0.59 ns (σ_A) and 0.67 ns (σ_B). The corresponding α and β values of these broad histograms are around 0.87. When the observation window is extended to 60 ms, σ_A and σ_B decrease to 0.22 and 0.24 ns. The resulting narrower lifetime histograms increase α and β values to 0.95 and 0.99 respectively.

Suppose that K single-molecule trajectories are collected in a tracking experiment, where each tracked molecule is classified to be either A or B by the MLE classifier. True

molecular numbers for A and B are K_A and K_B. Here we denote the event that $\widehat{K}_A$ and $\widehat{K}_B$ molecules are classified as A and B ($\widehat{K}_A + \widehat{K}_B = K_A + K_B = K$) as M. The probability p(M) is then:

$$\mathrm{p}(M) = \sum_{i=0}^{K} C_i^K \left(\frac{a}{a+b}\right)^i \left(\frac{b}{a+b}\right)^{K-i} \left[\sum_{j=0}^{i} C_j^i \alpha^j (1-\alpha)^{i-j} \cdot C_{\widehat{K}_A - j}^{K-i} \beta^{\widehat{K}_B - (i-j)} (1-\beta)^{\widehat{K}_A - j}\right]$$

where i is the number of true A molecules among all tracked molecules, and j is the number of true A molecules that have been correctly classified as A. p(M) can be considered as follows: p(M)= (probability of having i true A molecules in the tracking experiment)·[(probability of j molecules among i being correctly classified as A) · (probability of having $\widehat{K}_A - j$ true B molecules being misidentified as A)].

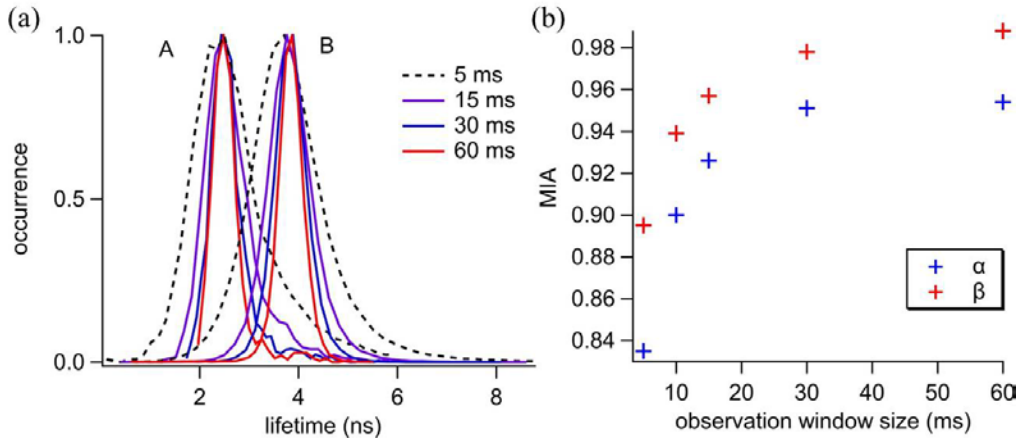

Figure 48. Larger observation windows leads to better molecular identification accuracy (**a**) Single-molecule lifetime histograms of the two fluorescent species A and B. The much extended observation window enabled by molecular tracking clearly provides more precise single-molecule identification based on lifetime. At 5 ms observation window, the estimated lifetime is biased towards a lower value due to scattering and dark counts. (**b**) Molecular identification accuracy (MIA) as a function of observation window size. Here α and β are the lifetime-based molecular identification accuracies for A and B, respectively. When the observation window is extended beyond 30 ms, much more photons are collected for lifetime estimation, resulting in α and β values greater than 95%.

We now calculate the probability of $\widehat{K}_A/\widehat{K}_B$ ratio to be within ±5% error (*i.e.* a predetermined, acceptable error) of the true a/b ratio, which is termed $p_{\pm 5\%}$:

$$p_{\pm 5\%} = \sum_{n=K_A^-}^{K_A^+} \sum_{i=0}^{K} C_i^K \left(\frac{a}{a+b}\right)^i \left(\frac{b}{a+b}\right)^{K-i} \left[\sum_{j=0}^{i} C_j^i \alpha^j (1-\alpha)^{i-j} \cdot C_{n-j}^{K-i} \beta^{K-n-(i-j)} (1-\beta)^{n-j}\right]$$

$$K_A^- = \text{round}(K \cdot \frac{(1-5\%) \cdot a}{b + (1-5\%) \cdot a})$$

$$K_A^+ = \text{round}(K \cdot \frac{(1+5\%) \cdot a}{b + (1+5\%) \cdot a})$$

where i is the number of true A molecules among all tracked molecules, and j is the number of true A molecules that have been correctly classified as A. K_A^+ and K_A^- are the upper and lower bounds of the numbers of predicted A so that the $\widehat{K}_A/\widehat{K}_B$ ratio can be within ±5% error of the true a/b ratio. For instance, when *K* is 10,000 and a/b = 100, K_A^+ and K_A^- are 104 and 94, respectively. $p_{\pm 5\%}$ is simply adding up the probabilities of having a $\widehat{K}_A$ within the range of $[K_A^-,\ K_A^+]$.

Here we assume that each classification event is a Bernoulli trial. Most studies simply use $\widehat{K}_A/\widehat{K}_B$ as an estimate of the true population ratio a/b[230-231]. However, we found that $F(\widehat{K}_A, \widehat{K}_B) = \widehat{K}_A/\widehat{K}_B$ is a biased estimator of a/b since:

$$E(F(\widehat{K}_A, \widehat{K}_B))$$

$$= E(\widehat{K}_A) \Big/ E(\widehat{K}_B) = \frac{K \cdot \frac{a}{a+b} \cdot \alpha + K \cdot \frac{b}{a+b} \cdot (1-\beta)}{K \cdot \frac{a}{a+b} \cdot (1-\alpha) + K \cdot \frac{b}{a+b} \cdot \beta} = \frac{a \cdot \alpha + b \cdot (1-\beta)}{a \cdot (1-\alpha) + b \cdot \beta} \neq \frac{a}{b}$$

To fix this problem, we propose an unbiased estimator $G\ (\widehat{N}_A, \widehat{N}_B)$ that faithfully reflects the a/b ratio regardless the values of α and β:

$$G\ (\widehat{K}_A, \widehat{K}_B) = \frac{\widehat{K}_A \cdot \beta - \widehat{K}_B(1-\beta)}{\widehat{K}_B \cdot \alpha - \widehat{K}_A(1-\alpha)}$$

It can be verified that

$$E\left(G\left(\widehat{K}_A, \widehat{K}_B\right)\right) = \frac{E\left(\widehat{K}_A\right) \cdot \beta - E\left(\widehat{K}_B\right)(1-\beta)}{E\left(\widehat{K}_B\right) \cdot \alpha - \widehat{K}_A(1-\alpha)} = \frac{a \cdot (\alpha + \beta - 1)}{b \cdot (\alpha + \beta - 1)} = \frac{a}{b}$$

5.3 RESULTS AND DISCUSSION

We now use the formulas derived above to predict the minimum number of single-molecule tracks required (termed $K_{\pm 5\%}$) to obtain a $p_{\pm 5\%}$ value greater than 95%. Assume one A molecule is embedded in 1,000 B molecules, and molecular identification accuracies (α and β) equal to 95%. When only 1,000 tracks are randomly acquired for analysis, there is only 5.7% chance that the estimator *G* represents the true a/b ratio with less than ±5% error ($p_{\pm 5\%}$ = 5.7%; denoted as a confidence level of 5.7%). To achieve 95% confidence level ($p_{\pm 5\%}$ = 95%) in detecting one A molecule embedded in 1,000 B molecules, we find that 90 million tracks are required. However, the number of tracks required is reduced by more than 5-fold, from 90 million to 17 million, when α and β increase from 0.95 to 0.99 (here we assume $\alpha = \beta$, Figure 49(a)). Our calculation indicates that for $0.95 \leq \alpha \leq 0.99$, $K_{\pm 5\%}$ and α have approximately a linear relationship (Figure 49b). For $0.99 \leq \alpha \leq 0.99999$, the relationship can be approximated by a power-law fit (Figure 49(c)). When α is equal to 0.99999, $K_{\pm 5\%}$ is further decreased to 1.55 million. When we change the criteria to be $p_{\pm 10\%}$ = 0.9 (*i.e.* ±10% error is allowed in quantification with 90% confidence level), the corresponding $K_{\pm 10\%}$ is 0.26 million. It should be noted that even when α is unity, $K_{\pm 5\%}$ is still as high as 1.52 million (Figure 49(d)). This is simply because we randomly sample the molecules in solution – among the 1,000 tracks acquired, there can be no A molecules at all.

When a/b ratio becomes smaller than 1/1000, the number of required tracked increases rapidly. For instance, at a/b ratio of 10^{-4}, it takes (1) $\alpha = \beta = 0.999$, 180 million tracks or (2) $\alpha = \beta = 0.9999$, 152 million tracks to reach a 95% confidence level. To speed up the calculation of C_n^m in MATLAB, normal approximation to binomial distribution is used. The results are identical to the standard C_n^m calculation for large *m*.

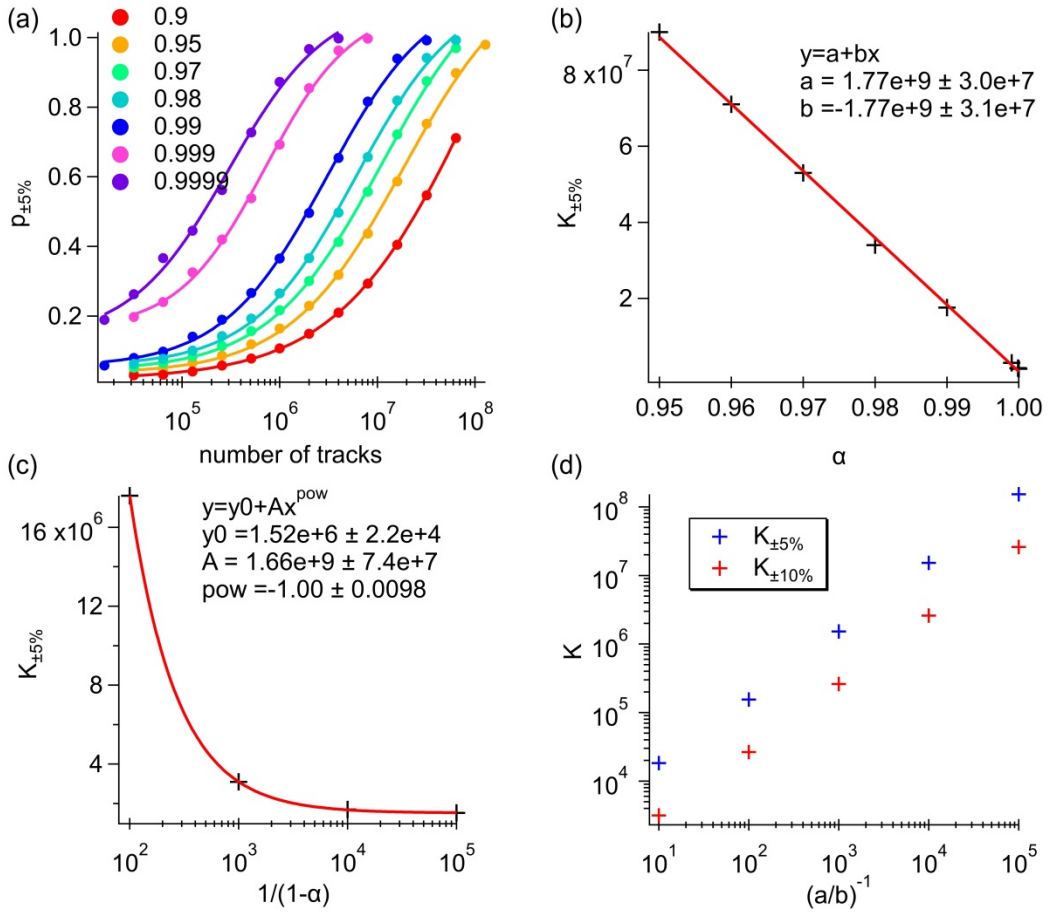

Figure 49. Results of $p_{\pm 5\%}$ and $K_{\pm 5\%}$ calculation. In this analysis, the a/b ratio is fixed at 1/1000. (**a**) The probability of having a/b quantification results within ±5% relative error ($p_{\pm 5\%}$) as a function of number of tracks, at different α and β values. (**b**) The minimum number of tracks required ($K_{\pm 5\%}$) to reach 95% confidence level ($p_{\pm 5\%}$ > 95%) as a function of α. A linear fit works well within this region. (**c**) $K_{\pm 5\%}$ as a function of 1/(1-α) for α=0.99, 0.999, 0.9999, and 0.99999. A power-law fitting is needed to (**d**) $K_{\pm 5\%}$ and $K_{\pm 10\%}$ as a function of $(a/b)^{-1}$, when α = β =1.

The tracking throughput (how many tracks can we get in an hour) depends on the analyte concentration. At 80 pM, we can typically obtain 10^4 tracks in an hour. While it is currently impractical to obtain millions of tracks in a single tracking experiment, our calculation indicates that sub-million tracks can possibly provide us with a reasonably good result in molecular quantification, depending on the a/b ratio that we want to quantify and

the quantification error that we can live with. However, it is still an open question how to increase the current tracking throughput from 10^4 tracks per hour to 10^5 tracks per hour. Our calculation here highlights both the opportunities and challenges that we have in precise single-molecule quantification using 3D tracking systems with lifetime characterization capabilities.

Appendix: Technical notes and protocols

A.1 OXYGEN SCAVENGER PREPARATION

The widely used PCD/PCA oxygen scavenger system consists of 50 nM PCD (Protocatechuate 3,4-dioxygenase), 2 mM PCA (3,4-dihydroxybenzoic acid), 25 mM HEPES, 100 mM NaCl and 3 mM Trolox. In our experiment, HEPES and NaCl are however not used.

(A) PCD storage buffer: 50 mM KCl, 1 mM EDTA, and 100 mM Tris-HCl pH 8.0, 50% glycerol

- 1 mL 10X KCL (0.3728 g in 10 mL DI)
- 1 mL 10X EDTA (0.0372 g in 10 mL DI)
- 1 mL 10X 1M Tris-HCL
- Glycerol: 5 mL
- DI: Add to 10 Ml

(B) PCD Stock Solution (1000X=50 µM, 238 µL)

- 8.33 mg PCD (Sigma P8279-25UN, MW~700 kDa, 3U/mg)
- Add 238 µL PCD storage buffer
- Storage: every 20 µL in -20 °C

(C) PCA Stock Solution (50X=100 mM, 5 mL)

- 0.077 g PCA (Sigma 37580-25G-F, MW=154.12)
- DI: add to 5 mL, adjust pH=9 using NaOH
- Storage: every 100 µL in -20 °C

(D) Trolox Stock Solution (25X=75 mM, 10 mL)

- 0.12 g Trolox (Sigma 238813-1G, MW=250.29)
- 1 mL methanol
- DI: Add to 10 mL, adjust pH=9.5 using NaOH

- Storage: every 250 µL in -20 °C

500 µL 680 pM DNA for tracking

- 0.536 g glycerol (426 µL)
- Dilute Cy5-DNA to 8 nM with Tris-HCl buffer. Get 43 µL from it.
- 20 µL 25X Trolox
- 10 µL 50X PCA
- 1 µL 1000X PCD

The GOC system consists of 0.5 mg/mL glucose oxidase, 140 µg/mL catalase and 10% (w/v) glucose.

A.2 LIPOSOME TETHERING

Our liposomes preparation follows the protocol in a 2015 Nature Communication paper[162]. Synthetic lipids POPC (1-palmitoyl-2-oleoyl-sn-glycero-3-phosphocholine, 850457P), DOPS (1,2-dioleoyl-sn-glycero-3-phospho-L-serine, 840035P), POPE (1-palmitoyl-2-oleoyl-sn-glycero-3-phosphoethanolamine, 850757P), cholesterol (700000P) and Biotinyl Cap PE (1,2-dipalmitoyl-sn-glycero-3-phosphoethanolamine-N-(cap biotinyl), 870277P) are purchased from Avanti Polar Lipids and mixed at a molar ratio POPC:DOPS:POPE:Chol:Biotinyl Cap PE=54.9:5:20:20:0.1. The mixture of lipids was dried and kept in vacuum for 24 h. The dried lipid film was hydrolysed with T50 buffer (10 mM Tris-HCl, pH 8.0, 50 mM NaCl) through vortexing. Afterwards, a cycle of freezing and thawing in liquid nitrogen followed by a water bath (35 °C) was repeated several times to form large unilamellar vesicles. To prepare monodisperse unilamellar liposomes, we performed extrusion using a mini extruder (Avanti Polar Lipid) with a 100-nm polycarbonate filter (Whatman).

A.3 SINGLE-MOLECULE TRACKING WITH FLUORESCENCE LIFETIME MEASUREMENT

A. Fiber bundle position calibration

(A.1) Turn on PicoHarp 300 and PHR 800. Turn on PicoQuant LDH-P-C-640B laser. Make sure the laser power is 100 μW, and repetition rate = 10MHz.

(A.2) Move the objective all the way down, raise the flip mirror (#1) blocking the laser light from entering the microscope, and raise the flip mirror (#2) between the emission filter wheel and detectors.

(A.3) Clean the objective with lens cleaning tissue – use the reflection of the room light to ensure it is clean. Then add n=1.33 immersion oil to the objective and add a No. 1 coverslip. Put a magnet on each corner of the coverslip.

(A.4) Connect the BNC cable (CH0 and CH1 in the 1st round, then CH2 and CH3 in the 2nd round) to the ALV auto-correlator.

(A.5) Dilute 0.5μL 100μM ATTO633-DNA sample with 1,000 μL DI water (final concentration is 50 nM)

(A.6) Lower mirror #1, set the emission filter wheel to 5, and adjust the focus using the auto-collimator.

(A.7) Raise mirror #1, lower mirror #2, and set the emission filter wheel to 4.

(A.8) Place 25uL ATTO633-DNA solution on the coverslip and raise the objective by 25μm to focus into the sample. Place a hydrated lid on top of the sample to prevent evaporation.

(A.9) Lift the black board covering the detectors. Open the ALV software. Set 40 runs with 15 seconds for each run. Turn off lights and turn on detectors. Wait a few seconds until all the DC power supplies show green light.

(A.10) Start the ALV software, monitor photon count traces when moving the fiber bundle with micrometers. Try to balance the detection channels and get as high photon count rate as possible. The photon count rate should be ~800kHz for each channel.

(A.11) To check if the two channels are balanced, set 5 runs with 20 seconds for each run. Save the data as CH01.ASC on desktop. Run ReadFCS.m. Photon count rate difference between CH0 and CH1 must be within 2 kHz, same for CH2 and CH3.

B. Detector time delay and IRF calibration

(B.1) Put the black board back without touching the optical cable. Re-connect all BNC cables to the power splitter.

(B.2) Put two ND filters (OD=2 and OD=0.4) in the excitation path.

(B.3) Open PicoHarp software. Set resolution 4ps, integration time 600 seconds. Check the box in front of “Routed”.

(B.4) Light off. Detectors on. Input 1 should has photon count rate 20~40 kHz. Start the measurement. Figure 50 is what you should see on the screen.

(B.5) Save the data as 2112_4ps.phd. Run read_phd.m, and select the phd file you just saved. You should see four smooth fluorescence decays histograms. Run this command in matlab: save(‘2112_4ps.mat’,’Counts’);

(B.6) Remove the ND filters. Clean the objective using the steps listed above. Focus the laser on the upper surface of the coverslip again. Adds 25uL Ludox onto the fresh coverslip and set the filter wheel to 5. Raise the objective by 25μm.

(B.7) Put two ND filters (OD=1 and OD=0.5) in the excitation path.

(B.8) In PicoHarp software, set resolution to be 128ps. Start measuring the instrument response function (IRF). The measurement only takes ~1 minute.

(B.9) Save the data as irf_128ps.phd. Run read_phd.m, and select this file. You should see four IRF by now. Run this command in MATLAB: save(‘irf_128ps.mat’,’Counts’);

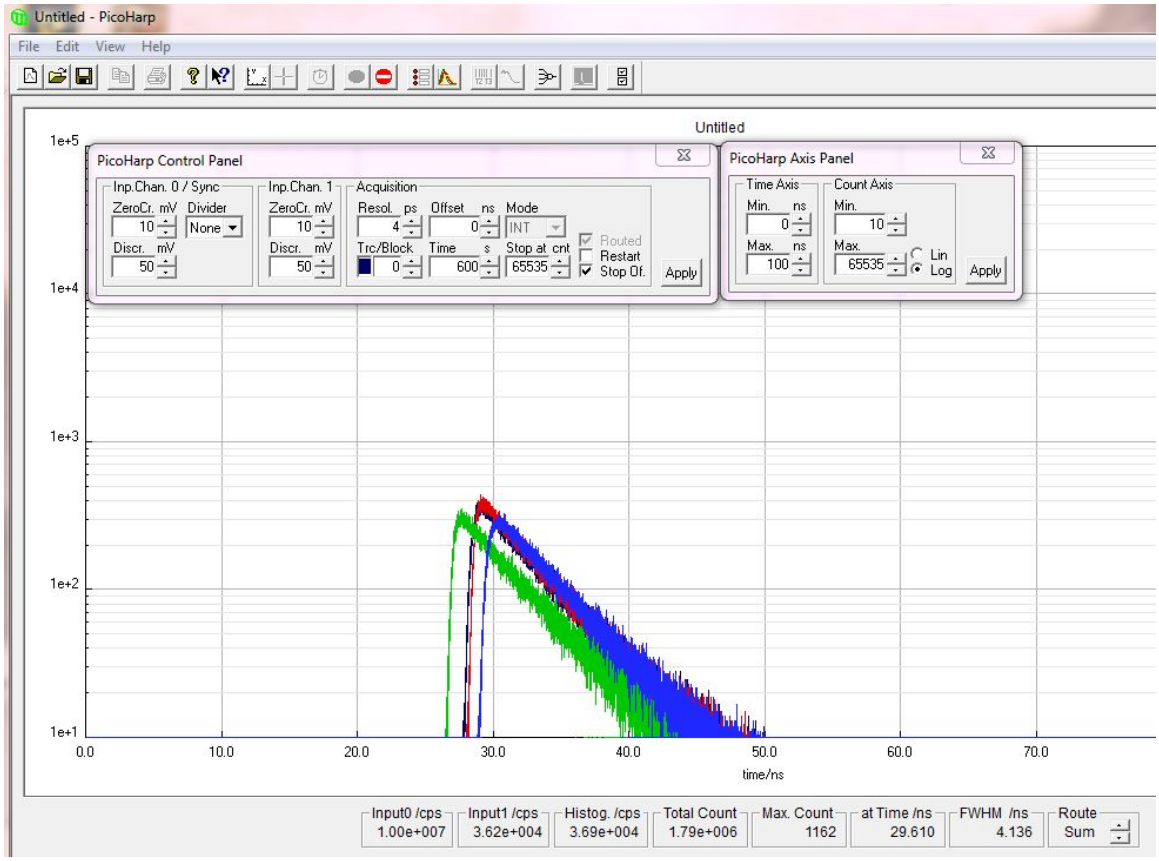

Figure 50. PicoHarp settings for fluorescence lifetime measurement

C. Data collection

(C.1) In PicoHarp software, click on TTTR (it takes a few seconds for initialization) and set time to 3 hours. Make sure the resolution is 128ps.

(C.2) Turn on the piezo stage. Open LabVIEW tracking software, go to imaging mode and set all coordinates to 0. Ensure the server and the client are connected (if not, the ip address settings are probably wrong). Start the Server Loop first, then the Client Loop.

(C.3) Put the DNA sample for SMT on the coverslip. The lid shouldn't be hydrated this time since glycerol in the DNA sample absorbs water.

(C.4) Ensure the LabVIEW Software has correct pre-set values on the Tracking tab (Figure 51). Update Rate determines the temporal resolution of position estimates, trigger threshold

and countdown threshold are dependent on the single particle brightness. For quenched ATTO633, they should be 5 kHz and 3.5 kHz respectively. For unquenched ATTO633, they are 7 kHz and 5 kHz.

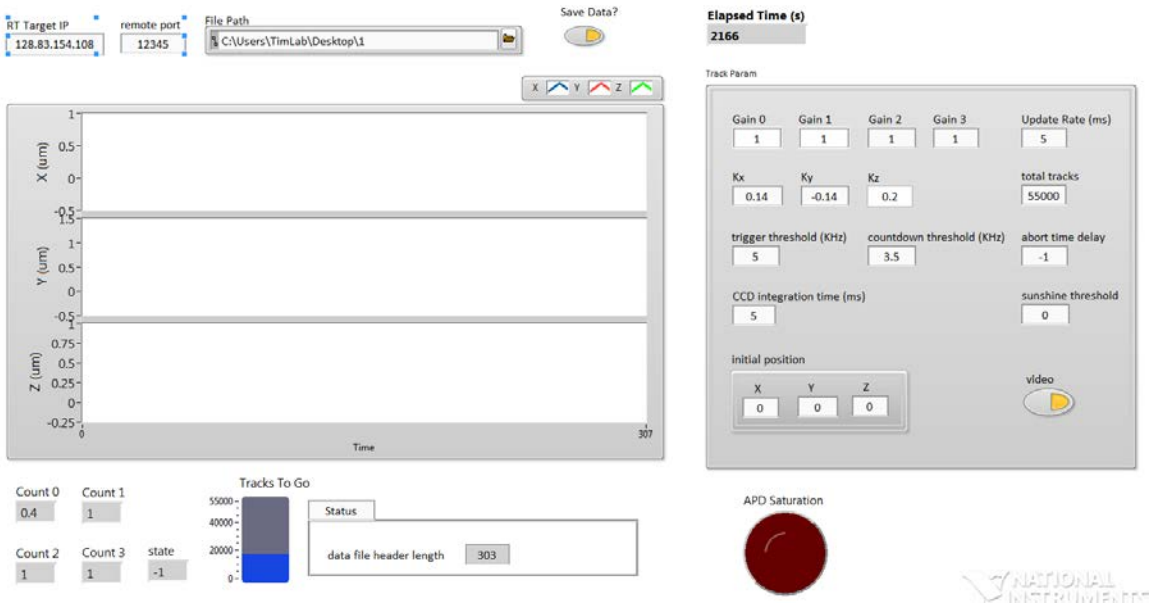

Figure 51. Client loop settings for 3D SMT

(C.5) Press run on the PicoHarp software to collect TCSPC data, and run the LabVIEW code in the Tracking Mode (server loop first, then the client loop).

(C.6) Perform SMT for an hour. Stop the LabVIEW program first, then the PicoHarp software.

D. Data processing

(D.1) Run *ExtractTrajInfo.m* to generate excel files that summarize the id (sorted by tracking duration), start time (in units of 5ms), end time, duration (in seconds) and photon count rate per channel (kHz) for each trajectory.

(D.2). Delete any abnormal trajectories (e.g. extremely long duration, high count rate, unidirectional movement) from the excel file.

(D.3) Run *SMT_GenerateHist.m* to generate fluorescence decays histograms for each trajectory. For binding kinetics analysis, select mode 0 (fixed integration time, in units of 5ms). Select mode 1 (fixed photon number) only when you want the lifetime fitting to have a constant uncertainty.

(D.4) Run *GetDelay.m* to calculate the relative time delay among the four channels (in units of 128ps). Record the numbers in a .txt file.

(D.5) Run SMT_Baseline_Lifetime.m for integrative analysis. Make sure the numbers in the .txt file are used as the variable "delay".

(D.6) Run SMT_ReadTau_Time.m for lifetime fitting. Make sure the full path of the experiment folder is correct.

E. Troubleshooting

(E.1) If the molecular trajectory seem to be periodic, stop and throw away the collected data (the piezo stage goes through random oscillation skewing any data collected). To solve, restart all the software and try again. If it still does not work, then there are two possible reasons (a) the dye concentration is too high (b) the piezo stage is not properly installed.

(E.2) If photon count rate is very low (<1 kHz), check if the laser actually illuminates the sample. The sample may also be out of focus.

(E.3) If the server cannot be connected, check the IP address setting (red arrows in Figure 52)

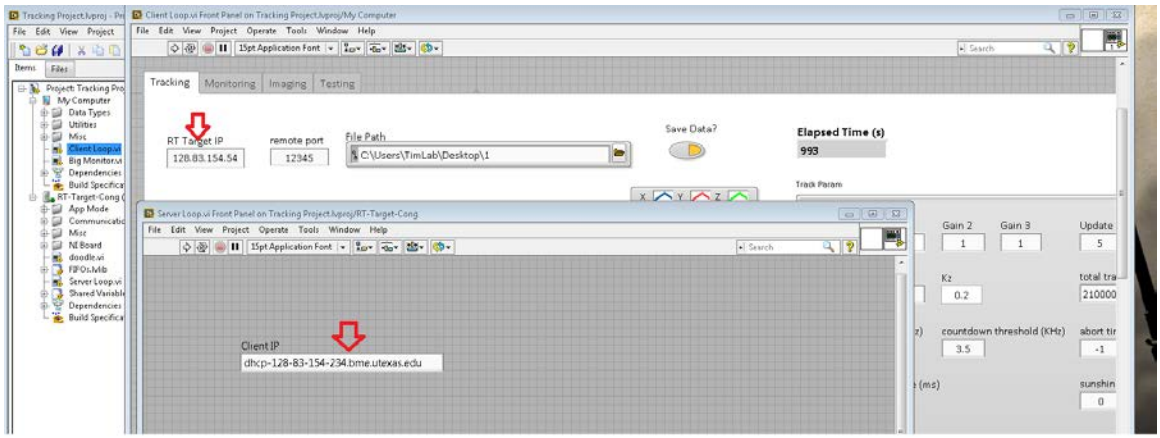

Figure 52. IP address settings in the server loop and client loop

A.4 ANTIBUNCHING MEASUREMENT

To perform antibunching measurement, Detecter 0 goes to PHR300 CHAN0, Detector 2 goes to Delay Box TRIGGER. Delay Box OUTPUT A goes to PHR300 CHAN1. An inverter and a 10dB attenuator have to be connected.

A.5 COMPENSATION OF TIME DELAYS AMONG FOUR CHANNELS

The fluorescence lifetime of tracked molecules is measured in TTTR (time-tagged time-resolved) mode with the TCSPC system PicoHarp 300 (in combination with PHR 800, synchronized with the 3D tracking system), which allows for simultaneous measurement of 4 channel signals. The photon arrival times are registered with 128 ps resolution, and post-processed by custom-written MATLAB scripts to build fluorescence decay histograms for each channel individually, with an integration time 15 ms.

To combine the 4 histograms into a single one for lifetime fitting, time delays among the four channels caused by cable length differences and misalignment have to be properly compensated by shifting the histograms along the time axis until their peaks overlap. The amount of shifts (in units of 128 ps), however, is determined by a separate experiment, in which the time delays among the 4 channels can be calibrated with a much higher resolution (4 ps) and better signal-to-noise ratio (~15 million fluorescence photons). In that experiment, the fluorescence decay histograms (one for each channel) of 50 nM ATTO633 labeled ssDNA are obtained with the same TCSPC setup (integration time 600 seconds, resolution 4ps, laser power 0.25 μW), and the relative time delays T_i (i=1-4) of peaks in the four histograms are measured. For all the following single-molecule experiments, a fixed amount of shift $-T_i$ is then applied to the i-th channel histogram.

A.6 FLUORESCENCE LIFETIME FITTING

We use maximum likelihood estimation (MLE) to fit the fluorescence lifetime. It has been shown that 100 detected photons are sufficient to determine a single exponential decay by MLE.

In time-correlated single-photon counting, assume S signal counts are accumulated in k bins, where n_i is the number of detected photon in i-*th* bin. f is the number of fitted parameters. The fluorescence lifetime pattern C is generated by the convolution of the instrument response function (IRF) with a single exponential decay $e^{-t/\tau}$ (Equation A.6-1). IRF is obtained from laser light scattered by ludox (20 wt % suspension in water).

$$c_i(\tau, s) = \mathrm{IRF} \otimes (e^{-t/\tau}) \qquad \text{A.6-1}$$

Taking a fraction γ^2 of constant background into consideration, Equation A.6-2 gives m_i, the probability of that a photon will fall into channel i for a certain fluorescence lifetime pattern.

$$m_i(\tau, s, \gamma) = \frac{\gamma^2}{k} + (1-\gamma^2)\frac{c_i(\tau, s)}{\sum c_i(\tau, s)} \qquad \text{A.6-2}$$

Normalization of $2I^*$ by the degree of freedom $(k-1-f)$ leads to reduced $2I_r^*$, which is 1 for an optimal fit.

$$2I_r^* = \frac{2}{k-1-f}\sum_{i=1}^{k} n_i \ln\left(\frac{n_i}{S m_i(\tau, s, \gamma)}\right) \qquad \text{A.6-3}$$

To determine the background fraction γ^2 and the shift s of the IRF with respect to the fluorescence decay, we add up fluorescence decays of all single-molecules tracked. This integration analysis will ensure good signal-to-noise ratio. s and γ were first allowed to vary freely with τ. The values of s and γ giving a minimal $2I_r^*$ were kept constant in the further analysis of individual single-molecule fluorescence decays, *i.e.* the

only remaining adjustable variable is the parameter of interest τ. It doesn't matter which IRF of the four channels you are using for lifetime fit, because the results are almost identical.

A.7 SINGLE-MOLECULE TRACKING SOFTWARE DESIGN

The LabVIEW tracking software consists of two major parts: the client loop and the server loop. The server loop runs on LabVIEW Real-Time Target (LabVIEW RT Operating System) and the client loop runs on a local Windows PC. The client takes in the tracking parameters (stage update rate, photon count threshold and so on) and sends them to the server when the tracking is initialized. During the SMT, the client writes the data (photon count rate, 3D trajectory and "state") received from the server via TCP/IP to its hard drive with a binary format. Although there may be concerns that HD access is not as fast as RAM and therefore it's not the best storage media for real-time application, in reality, we haven't encountered any data overflow problem. The continuous data writes (<50MB/hour) on HD make sure that the experiment can be performed for hours. The format of the binary file is custom designed. The binary file has a header showing time stamp and important tracking parameters. The MATLAB program automatically skips the header and only looks at the actual data. Since the data structure of the binary file is custom designed (Figure 53), you need to synchronize the LabVIEW software that generates the file and MATLAB code that reads the file whenever the data structure is modified.

The client loop has 4 modes: Tracking, Monitoring, Imaging, and Testing. The Monitoring mode is essentially the same with Tracking except that it disables feedback control of the piezo stage. It is useful for flow-through analysis and alignment. Imaging mode is used for collection efficiency function (CEF) scanning. It can be used to find a specific target for tracking as well, but pixel-by-pixel scanning is inherently a slow process. Testing mode is a duplicate of Tracking that allows you to develop and test new features. In the server loop, there are 3 tracking algorithms that you can choose: "Search Actively" (even if state < 0, we still keep tracking the current target until state < -10. Piezo stage goes back to the origin point once the target is lost), "Wait for Luck" (if state < -5, the piezo

stage stays where it is and waits for the next triggering) and “Enjoy the Sunshine” (when photon count rate is really high, the piezo stage doesn’t respond to error signals and just stays where it is). “Search Actively” is the default algorithm.

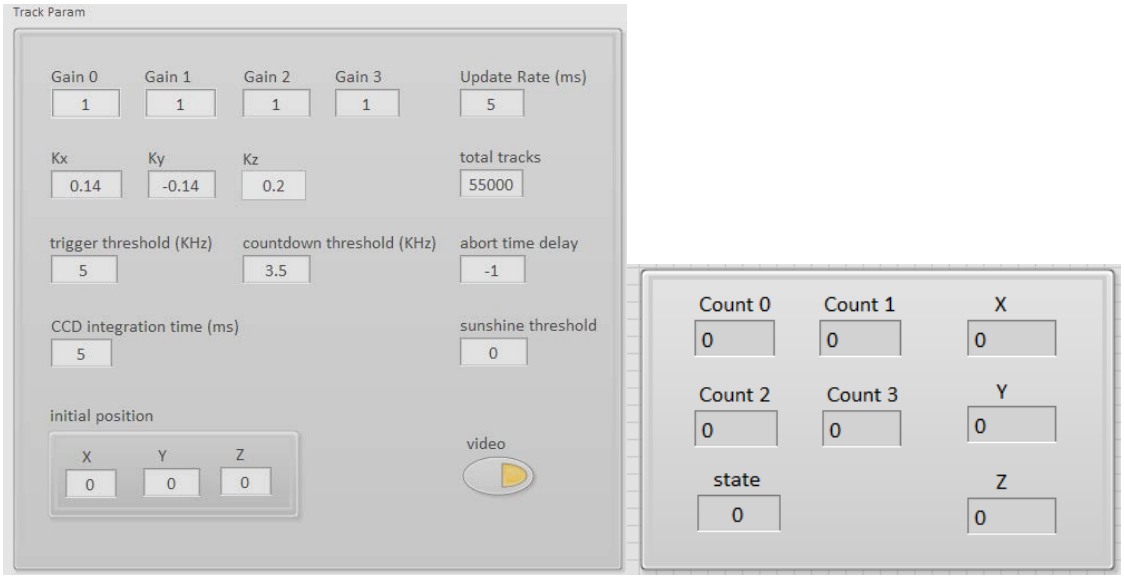

Figure 53. FIFO queues in the tracking software (**Left**): Track Param, defined by user in the client loop (**Right**): Track Data, real experimental data collected by the server loop.

Typically the stage update rate is 200 Hz. A 200 Hz pulse train is generated by PCI-6602 using its internal 20 MHz clock, and sent to PCI-6731 and PicoHarp 300 respectively for synchronization. The cable connections and channel specification (Figure 54) has to be consistent. PCI-6602 also generates a pulse train to trigger the camera (gated mode).

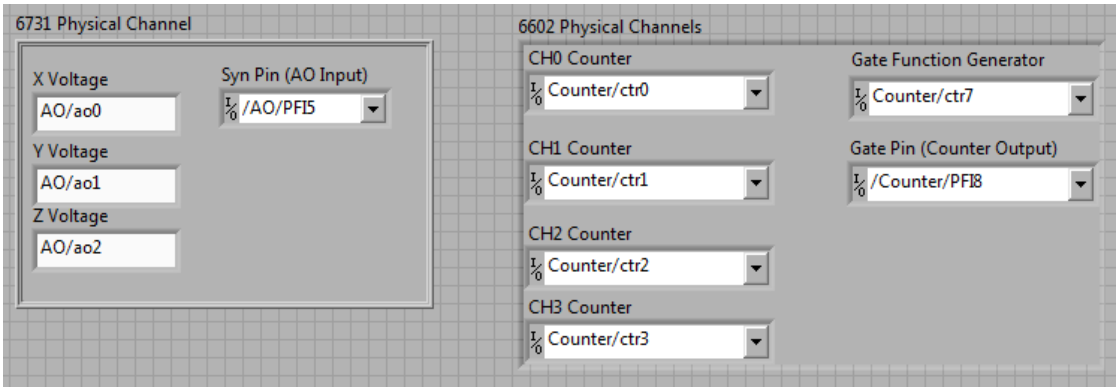

Figure 54. Physical channel specifications in Tracking Loop (under Server Loop) NI PCI-6602 is an 8-channel counter for photon counting, PCI-6731 is the analog output that drives piezo stage movement.

A.8 BUILDING A TOTAL INTERNAL REFLECTION FLUORESCENCE MICROSCOPE

We have built a TIRF microscope as a complementary method to for single-molecule detection. The system layout of the TIRF microscope is shown in Figure 55. The design allows us to continuesly swtich between the eip-fluorescence mode and TIRF mode with a 1D translation stage. We have compared the image contrast in the epi-fluorescence mode and TIRF mode (Figure 56) to confirm that the TIRF is achieved.

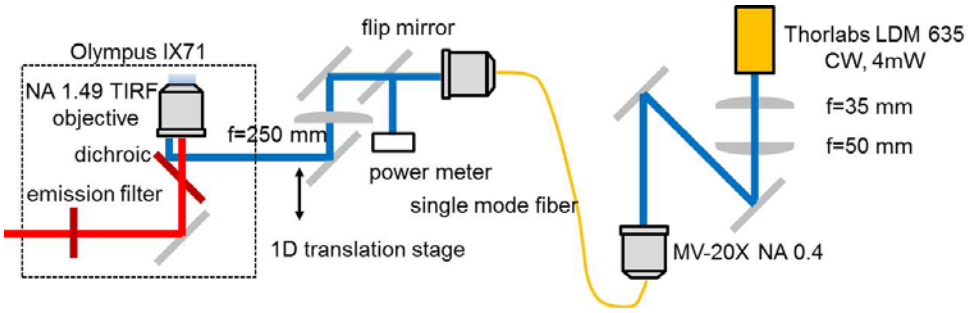

Figure 55. System layout of home-built TIRF microscope

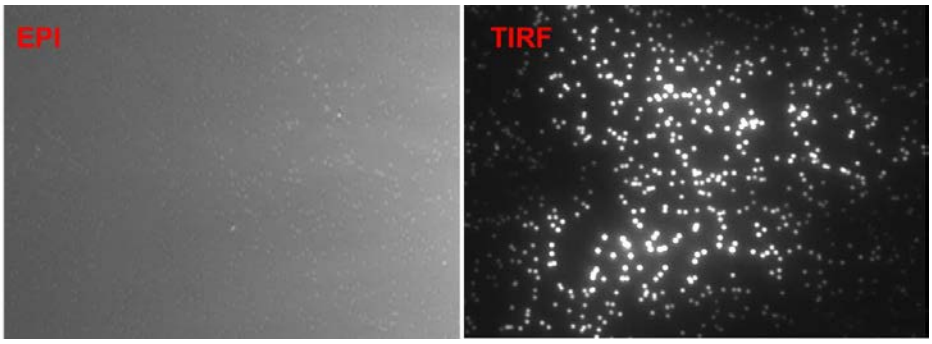

Figure 56. Comparison of image contrast for epi-fluorescence and TIRF imaging. Integration time is 200 ms, and the image contrast is auto adjusted. The F8807 (LOT1654398) carboxylate-modified 0.2μm FluoSpheres in diluted by 1:400 ratio.

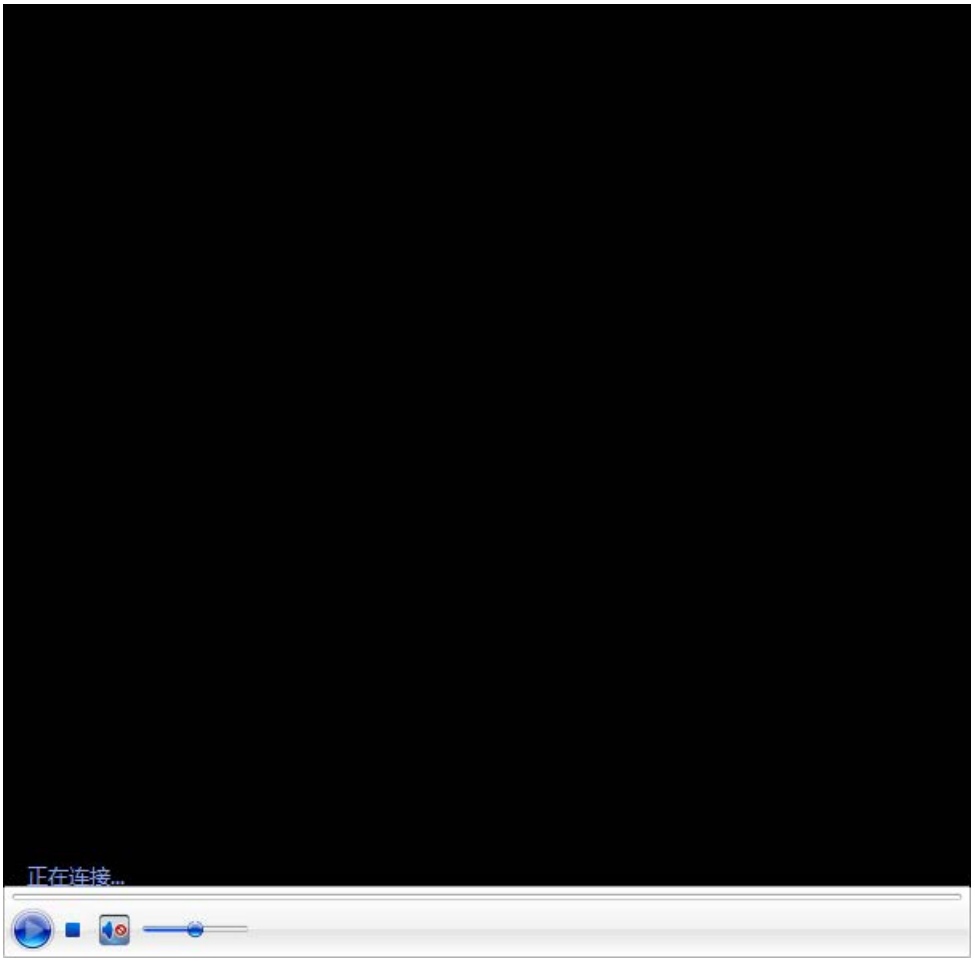

Figure 57. Fluorescent beads brightness before and after TIR occurs. This is a video that can be played within Microsoft Word.

A.9 SINGLE DYE BRIGHTNESS MEASURED BY FCS

dye	laser power (μW)	brightness (kHz)
Cy5	100 (640 nm)	19
ATTO647N, ATTO633	100 (640 nm)	16
Alexa Fluor 647	100 (640 nm)	6

A.10 DNA INVENTORY FOR QUENCHING EFFICIENCY CHARACTERIZATION

Table 7: ATTO633 - Iowa Black® FQ quenching efficiency characterization

Lifetime (ns)	donor-quencher spacing	DNA duplex schematic	DNA duplex ID	Vendor ID
0.98	2 nt		ATTO633_FQ_2nt	FQ1111
1.18	4 nt		ATTO633_FQ_4nt	FQ1112
1.38	6 nt		ATTO633_FQ_6nt	FQ1113
2.01	8 nt	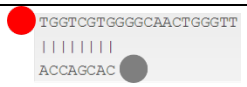	ATTO633_FQ_8nt	FQ1116
2.96	10 nt		ATTO633_FQ_10nt	FQ1115
3.85	14 nt		ATTO633_FQ_14nt	FQ1114
4.16	No quencher		/	ATTO633N_Origami_21nt

ID	Strand 1	Strand 2	Base pairs	# of LNA
ATTO633_FQ_2nt	ATTO633_21nt	3'FQ_23nt	21	0
ATTO633_FQ_4nt	ATTO633_21nt	3'FQ_25nt	21	0
ATTO633_FQ_6nt	ATTO633_21nt	3'FQ_27nt	21	0
ATTO633_FQ_8nt	ATTO633_21nt	FQ_5LNA_8nt	8	5
ATTO633_FQ_10nt	ATTO633_21nt	FQ_5LNA_10nt	10	5
ATTO633_FQ_14nt	ATTO633_21nt	FQ_3LNA_14nt	14	3

ID	Sequence	Vendor ID
ATTO633_21nt	/5ATTO633N/TGG TCG TGG GGC AAC TGG GTT	ATTO633N_Origami_21nt
3'FQ_23nt	AAC CCA GTT GCC CCA CGA CCA TT/3AIABkFQ/	Origami_23nt_FQ
3'FQ_25nt	AAC CCA GTT GCC CCA CGA CCA TTT T/3AIBkFQ/	Origami_25nt_FQ
3'FQ_27nt	AAC CCA GTT GCC CCA CGA CCA TTT TTT/3AIBFQ/	Origami_27nt_FQ
FQ_5LNA_8nt	/5IABkFQ/**C**A**C** **GAC** CA	5'FQ_5LNA_8nt
FQ_5LNA_10nt	/5IABkFQ/**CC**C A**C**G **AC**C A	5'FQ_5LNA_10nt
FQ_3LNA_14nt	/5IABkFQ/**T**TG CC**C** CAC GA**C** CA	5'FQ_3LNA_14nt

Table 8: ATTO647N - Iowa Black® RQ quenching efficiency characterization

Lifetime (ns)	donor-quencher spacing	DNA duplex schematic	DNA duplex ID
0.66	1	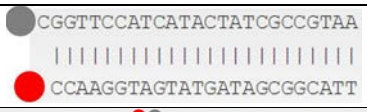	ATTO647N_RQ_1nt
1.61	5		ATTO647N_RQ_5nt
1.64	8		ATTO647N_RQ_8nt
2.41	11		ATTO647N_RQ_11nt
2.96	14	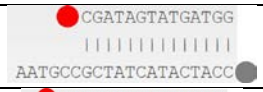	ATTO647N_RQ_14nt
3.58	17		ATTO647N_RQ_17nt

ID	Strand 1	Strand 2	Strand 3	Vendor ID
ATTO647N_RQ_1nt	ATTO647N_24nt	RQ_25nt	/	#1120
ATTO647N_RQ_5nt	ATTO647N_24nt	RQ_60nt	Bridge_5sp	#1122
ATTO647N_RQ_8nt	ATTO647N_24nt	RQ_60nt	Bridge_8sp	#1123
ATTO647N_RQ_11nt	ATTO647N_24nt	RQ_60nt	Bridge_11sp	#1124
ATTO647N_RQ_14nt	ATTO647N_14nt	RQ_6LNA_20nt	/	#1125
ATTO647N_RQ_17nt	ATTO647N_17nt	RQ_6LNA_20nt	/	#1126

ID	Sequence	Vendor ID
ATTO647N_24nt	TTACGGCGATAGTATGATGGAACC /3ATTO647NN/	24nt-2112
ATTO647N_17nt	/5ATTO647NN/ CGG CGA TAG TAT GAT GG	17nt-2112
ATTO647N_14nt	/5ATTO647NN/ CGA TAG TAT GAT GG	14nt-2112
RQ_25nt	/5IAbRQ/CGG TTC CAT CAT ACT ATC GCC GTA A	Iowa_24nt_FQ_1sp
RQ_60nt	/5IAbRQ/CATACAACGAATGTCATGCGGATCCAGTC AAG GCT GAT TCG GTCATTCGCGTTAAACAAT	BHQ2B
Bridge_5sp	GGAT CCG CAT GAC ATT CGT TGT ATG TGA CTG GTT CCA TCA TAC TAT CGC CGT AAG CGATT	A_5sp_FQ
Bridge_8sp	GGAT CCG CAT GAC ATT CGT TGT ATG TGA CT CGA G GTT CCA TCA TAC TAT CGC CGT AAG TT	A_8sp_FQ
Bridge_11sp	GGAT CCG CAT GAC ATT CGT TGT ATG TGA CT CGA GTT GGT TCC ATC ATA CTA TCG CCG TAA	A_11sp_FQ
RQ_6LNA_20nt	/5IAbRQ/ C+C+AT+CA+TA+C+TATCGCCGTAA	LNA Probe A

The DNA duplexes were hybridized in-house in 100 mM pH 8.0 Tris-HCl buffer.

Table 9: ATTO647N - Iowa Black® FQ quenching efficiency characterization

Lifetime (ns)	donor-quencher spacing	DNA duplex schematic	DNA duplex ID
1.22	0	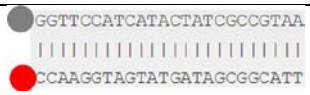	ATTO647N_FQ_0nt
0.712	1	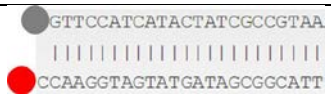	ATTO647N_FQ_1nt

Duplex ID	Strand 1	Strand 2	Vendor ID
ATTO647N_FQ_0nt	ATTO647N_24nt	5'FQ_24nt	#1134
ATTO647N_FQ_1nt	ATTO647N_24nt	5'FQ_23nt	#1135

ID	Sequence	Vendor ID
ATTO647N_24nt	TTACGGCGATAGTATGATGGAACC/3ATTO647NN/	24nt-2112
5'FQ_24nt	/5IAbkFQ/ GGT TCC ATC ATA CTA TCG CCG TAA	IowaFQ_24nt
5'FQ_23nt	/5IAbkFQ/ GTT CCA TCA TAC TAT CGC CGT AA	IowaFQ_23nt

Table 10: No fluorescence quenching by proximal G-bases

Lifetime (ns)	Duplex ID	DNA duplex schematic	Vendor ID
4.47	ATTO647N_PROX_24nt		#1129
4.48	ATTO647N_PROX_30nt		#1130
4.32	ATTO647N_PROX_comp_30nt	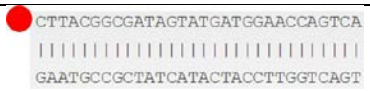	#1132

duplex ID	Strand 1	Strand 2
ATTO647N_PROX_24nt	ATTO647N_24nt	Bridge_5sp
ATTO647N_PROX_30nt	ATTO647N_30nt	Bridge_5sp
ATTO647N_PROX_comp_30nt	ATTO647N_30nt	30nt-comp

ID	Sequence	Vendor ID
ATTO647N_30nt	/5ATTO647N/ CTT ACG GCG ATA GTA TGA TGG AAC CAG TCA	30nt-2112
ATTO647N_24nt	TTACGGCGATAGTATGATGGAACC/3ATTO647NN/	24nt-2112
Bridge_5sp	GGAT CCG CAT GAC ATT CGT TGT ATG TGA CTG GTT CCA TCA TAC TAT CGC CGT AAG CGATT	A_5sp_FQ
30nt-comp	TGA CTG GTT CCA TCA TAC TAT CGC CGT AAG	30nt-comp

Bibliography

(1) Lu, H. P.; Xun, L.; Xie, X. S., Single-molecule enzymatic dynamics. *Science* **1998,** *282* (5395), 1877-1882.

(2) van Oijen, A. M.; Blainey, P. C.; Crampton, D. J., et al., Single-molecule kinetics of λ exonuclease reveal base dependence and dynamic disorder. *Science* **2003,** *301* (5637), 1235-1238.

(3) Cai, L.; Friedman, N.; Xie, X. S., Stochastic protein expression in individual cells at the single molecule level. *Nature* **2006,** *440* (7082), 358-362.

(4) Elf, J.; Li, G.-W.; Xie, X. S., Probing transcription factor dynamics at the single-molecule level in a living cell. *Science* **2007,** *316* (5828), 1191-1194.

(5) Chung, H. S.; McHale, K.; Louis, J. M., et al., Single-molecule fluorescence experiments determine protein folding transition path times. *Science* **2012,** *335* (6071), 981-984.

(6) Chung, H. S.; Louis, J. M.; Eaton, W. A., Experimental determination of upper bound for transition path times in protein folding from single-molecule photon-by-photon trajectories. *Proceedings of the National Academy of Sciences* **2009,** *106* (29), 11837-11844.

(7) Sako, Y.; Minoghchi, S.; Yanagida, T., Single-molecule imaging of EGFR signalling on the surface of living cells. *Nature Cell Biology* **2000,** *2* (3), 168-172.

(8) Teramura, Y.; Ichinose, J.; Takagi, H., et al., Single-molecule analysis of epidermal growth factor binding on the surface of living cells. *The EMBO Journal* **2006,** *25* (18), 4215-4222.

(9) Liu, S.-L.; Zhang, Z.-L.; Tian, Z.-Q., et al., Effectively and efficiently dissecting the infection of influenza virus by quantum-dot-based single-particle tracking. *ACS Nano* **2011,** *6* (1), 141-150.

(10) Joo, K.-I.; Fang, Y.; Liu, Y., et al., Enhanced real-time monitoring of adeno-associated virus trafficking by virus–quantum dot conjugates. *ACS Nano* **2011,** *5* (5), 3523-3535.

(11) Lipman, E. A.; Schuler, B.; Bakajin, O., et al., Single-molecule measurement of protein folding kinetics. *Science* **2003,** *301* (5637), 1233-1235.

(12) Ha, T.; Ting, A. Y.; Liang, J., et al., Single-molecule fluorescence spectroscopy of enzyme conformational dynamics and cleavage mechanism. *Proceedings of the National Academy of Sciences* **1999,** *96* (3), 893-898.

(13) Zander, C.; Keller, R. R.; Enderlein, J., *Single molecule detection in solution*. Wiley Online Library: 2002; Vol. 43.

(14) Laurence, T. A.; Weiss, S., How to detect weak pairs. *Science* **2003,** *299* (5607), 667-668.

(15) Kapanidis, A. N.; Lee, N. K.; Laurence, T. A., et al., Fluorescence-aided molecule sorting: analysis of structure and interactions by alternating-laser excitation of single molecules. *Proceedings of the National Academy of Sciences of the United States of America* **2004,** *101* (24), 8936-8941.

(16) Prummer, M.; Hübner, C. G.; Sick, B., et al., Single-molecule identification by spectrally and time-resolved fluorescence detection. *Analytical Chemistry* **2000,** *72* (3), 443-447.
(17) Schaffer, J.; Volkmer, A.; Eggeling, C., et al., Identification of single molecules in aqueous solution by time-resolved fluorescence anisotropy. *The Journal of Physical Chemistry A* **1999,** *103* (3), 331-336.
(18) Müller, R.; Zander, C.; Sauer, M., et al., Time-resolved identification of single molecules in solution with a pulsed semiconductor diode laser. *Chemical Physics Letters* **1996,** *262* (6), 716-722.
(19) Myong, S.; Rasnik, I.; Joo, C., et al., Repetitive shuttling of a motor protein on DNA. *Nature* **2005,** *437* (7063), 1321-1325.
(20) Cisse, I. I.; Kim, H.; Ha, T., A rule of seven in Watson-Crick base-pairing of mismatched sequences. *Nature Structural & Molecular Biology* **2012,** *19* (6), 623-627.
(21) Kuzmenkina, E. V.; Heyes, C. D.; Nienhaus, G. U., Single-molecule Förster resonance energy transfer study of protein dynamics under denaturing conditions. *Proceedings of the National Academy of Sciences* **2005,** *102* (43), 15471-15476.
(22) Luo, G.; Wang, M.; Konigsberg, W. H., et al., Single-molecule and ensemble fluorescence assays for a functionally important conformational change in T7 DNA polymerase. *Proceedings of the National Academy of Sciences* **2007,** *104* (31), 12610-12615.
(23) McKinney, S. A.; Déclais, A.-C.; Lilley, D. M., et al., Structural dynamics of individual Holliday junctions. *Nature Structural & Molecular Biology* **2003,** *10* (2), 93-97.
(24) Kusumi, A.; Shirai, Y. M.; Koyama-Honda, I., et al., Hierarchical organization of the plasma membrane: Investigations by single‐molecule tracking vs. fluorescence correlation spectroscopy. *Febs Letters* **2010,** *584* (9), 1814-1823.
(25) Kusumi, A.; Suzuki, K. G.; Kasai, R. S., et al., Hierarchical mesoscale domain organization of the plasma membrane. *Trends in Biochemical Sciences* **2011,** *36* (11), 604-615.
(26) Kasai, R. S.; Suzuki, K. G.; Prossnitz, E. R., et al., Full characterization of GPCR monomer–dimer dynamic equilibrium by single molecule imaging. *The Journal of Cell Biology* **2011,** *192* (3), 463-480.
(27) Hern, J. A.; Baig, A. H.; Mashanov, G. I., et al., Formation and dissociation of M1 muscarinic receptor dimers seen by total internal reflection fluorescence imaging of single molecules. *Proceedings of the National Academy of Sciences* **2010,** *107* (6), 2693-2698.
(28) Yildiz, A.; Forkey, J. N.; McKinney, S. A., et al., Myosin V walks hand-over-hand: single fluorophore imaging with 1.5-nm localization. *Science* **2003,** *300* (5628), 2061-2065.
(29) Lowe, A. R.; Siegel, J. J.; Kalab, P., et al., Selectivity mechanism of the nuclear pore complex characterized by single cargo tracking. *Nature* **2010,** *467* (7315), 600-603.
(30) Tokunaga, M.; Imamoto, N.; Sakata-Sogawa, K., Highly inclined thin illumination enables clear single-molecule imaging in cells. *Nature Methods* **2008,** *5* (2), 159-161.

(31) Gao, L.; Shao, L.; Chen, B.-C., et al., 3D live fluorescence imaging of cellular dynamics using Bessel beam plane illumination microscopy. *Nature Protocols* **2014,** *9* (5), 1083-1101.
(32) Liu, Z.; Legant, W. R.; Chen, B.-C., et al., 3D imaging of Sox2 enhancer clusters in embryonic stem cells. *Elife* **2014,** *3*, e04236.
(33) Dietrich, C.; Yang, B.; Fujiwara, T., et al., Relationship of lipid rafts to transient confinement zones detected by single particle tracking. *Biophysical Journal* **2002,** *82* (1), 274-284.
(34) Kasai, R. S.; Kusumi, A., Single-molecule imaging revealed dynamic GPCR dimerization. *Current Opinion in Cell Biology* **2014,** *27*, 78-86.
(35) Kusumi, A.; Ike, H.; Nakada, C., et al. In *Single-molecule tracking of membrane molecules: plasma membrane compartmentalization and dynamic assembly of raft-philic signaling molecules*, Seminars in Immunology, Elsevier: 2005; pp 3-21.
(36) Ahrens, M. B.; Orger, M. B.; Robson, D. N., et al., Whole-brain functional imaging at cellular resolution using light-sheet microscopy. *Nature Methods* **2013,** *10* (5), 413-420.
(37) Li, Y.; Hu, Y.; Cang, H., Light sheet microscopy for tracking single molecules on the apical surface of living cells. *The Journal of Physical Chemistry B* **2013,** *117* (49), 15503-15511.
(38) Ritter, J. G.; Veith, R.; Veenendaal, A., et al., Light sheet microscopy for single molecule tracking in living tissue. *PLoS One* **2010,** *5* (7), e11639.
(39) Chen, K.; Wang, B.; Granick, S., Memoryless self-reinforcing directionality in endosomal active transport within living cells. *Nature Materials* **2015,** *14* (6), 589-593.
(40) Wang, B.; Kuo, J.; Granick, S., Bursts of active transport in living cells. *Physical Review Letters* **2013,** *111* (20), 208102.
(41) Robin, F. B.; McFadden, W. M.; Yao, B., et al., Single-molecule analysis of cell surface dynamics in Caenorhabditis elegans embryos. *Nature Methods* **2014,** *11* (6), 677-682.
(42) Ritter, J. G.; Veith, R.; Siebrasse, J.-P., et al., High-contrast single-particle tracking by selective focal plane illumination microscopy. *Optics Express* **2008,** *16* (10), 7142-7152.
(43) Planchon, T. A.; Gao, L.; Milkie, D. E., et al., Rapid three-dimensional isotropic imaging of living cells using Bessel beam plane illumination. *Nature Methods* **2011,** *8* (5), 417-423.
(44) Kao, H. P.; Verkman, A., Tracking of single fluorescent particles in three dimensions: use of cylindrical optics to encode particle position. *Biophysical Journal* **1994,** *67* (3), 1291-1300.
(45) Yajima, J.; Mizutani, K.; Nishizaka, T., A torque component present in mitotic kinesin Eg5 revealed by three-dimensional tracking. *Nature structural & molecular biology* **2008,** *15* (10), 1119-1121.
(46) Thompson, M. A.; Casolari, J. M.; Badieirostami, M., et al., Three-dimensional tracking of single mRNA particles in Saccharomyces cerevisiae using a double-helix point spread function. *Proceedings of the National Academy of Sciences* **2010,** *107* (42), 17864-17871.

(47) Gahlmann, A.; Ptacin, J. L.; Grover, G., et al., Quantitative multicolor subdiffraction imaging of bacterial protein ultrastructures in three dimensions. *Nano Letters* **2013,** *13* (3), 987-993.
(48) Shechtman, Y.; Weiss, L. E.; Backer, A. S., et al., Precise three-dimensional scan-free multiple-particle tracking over large axial ranges with tetrapod point spread functions. *Nano Letters* **2015,** *15* (6), 4194-4199.
(49) Jia, S.; Vaughan, J. C.; Zhuang, X., Isotropic three-dimensional super-resolution imaging with a self-bending point spread function. *Nature Photonics* **2014,** *8* (4), 302-306.
(50) Wells, N. P.; Lessard, G. A.; Goodwin, P. M., et al., Time-resolved three-dimensional molecular tracking in live cells. *Nano Letters* **2010,** *10* (11), 4732-4737.
(51) Welsher, K.; Yang, H., Multi-resolution 3D visualization of the early stages of cellular uptake of peptide-coated nanoparticles. *Nature Nanotechnology* **2014,** *9* (3), 198-203.
(52) McHale, K.; Berglund, A. J.; Mabuchi, H., Quantum dot photon statistics measured by three-dimensional particle tracking. *Nano Letters* **2007,** *7* (11), 3535-3539.
(53) Lessard, G. A.; Goodwin, P. M.; Werner, J. H., Three-dimensional tracking of individual quantum dots. *Applied Physics Letters* **2007,** *91* (22), 224106.
(54) Juette, M. F.; Bewersdorf, J., Three-dimensional tracking of single fluorescent particles with submillisecond temporal resolution. *Nano Letters* **2010,** *10* (11), 4657-4663.
(55) Katayama, Y.; Burkacky, O.; Meyer, M., et al., Real‐Time Nanomicroscopy via Three‐Dimensional Single‐Particle Tracking. *ChemPhysChem* **2009,** *10* (14), 2458-2464.
(56) Levi, V.; Gratton, E., Three-dimensional particle tracking in a laser scanning fluorescence microscope. *Single Particle Tracking and Single Molecule Energy Transfer* **2009**, 1-24.
(57) Levi, V.; Ruan, Q.; Gratton, E., 3-D particle tracking in a two-photon microscope: application to the study of molecular dynamics in cells. *Biophysical Journal* **2005,** *88* (4), 2919-2928.
(58) Levi, V.; Ruan, Q.; Kis-Petikova, K., et al., Scanning FCS, a novel method for three-dimensional particle tracking. *Biochemical Society Transactions* **2003**.
(59) Berglund, A. J.; Mabuchi, H., Tracking-FCS: Fluorescence correlation spectroscopy of individual particles. *Optics Express* **2005,** *13* (20), 8069-8082.
(60) Berglund, A. J.; McHale, K.; Mabuchi, H., Feedback localization of freely diffusing fluorescent particles near the optical shot-noise limit. *Optics Letters* **2007,** *32* (2), 145-147.
(61) Xu, C. S.; Cang, H.; Montiel, D., et al., Rapid and quantitative sizing of nanoparticles using three-dimensional single-particle tracking. *The Journal of Physical Chemistry C* **2007,** *111* (1), 32-35.
(62) Perillo, E. P.; Liu, Y.-L.; Huynh, K., et al., Deep and high-resolution three-dimensional tracking of single particles using nonlinear and multiplexed illumination. *Nature communications* **2015,** *6*.
(63) Liu, C.; Liu, Y.-L.; Perillo, E., et al., Improving z-tracking accuracy in the two-photon single-particle tracking microscope. *Applied Physics Letters* **2015,** *107* (15), 153701.

(64) Perillo, E.; Liu, Y.-L.; Liu, C., et al. In *Single particle tracking through highly scattering media with multiplexed two-photon excitation*, SPIE BiOS, International Society for Optics and Photonics: 2015; pp 933107-933107-8.
(65) Ram, S.; Prabhat, P.; Chao, J., et al., High accuracy 3D quantum dot tracking with multifocal plane microscopy for the study of fast intracellular dynamics in live cells. *Biophysical Journal* **2008,** *95* (12), 6025-6043.
(66) Toprak, E.; Balci, H.; Blehm, B. H., et al., Three-dimensional particle tracking via bifocal imaging. *Nano Letters* **2007,** *7* (7), 2043-2045.
(67) Huang, B.; Wang, W.; Bates, M., et al., Three-dimensional super-resolution imaging by stochastic optical reconstruction microscopy. *Science* **2008,** *319* (5864), 810-813.
(68) Pavani, S. R. P.; Thompson, M. A.; Biteen, J. S., et al., Three-dimensional, single-molecule fluorescence imaging beyond the diffraction limit by using a double-helix point spread function. *Proceedings of the National Academy of Sciences* **2009,** *106* (9), 2995-2999.
(69) Berg, H. C., How to track bacteria. *Review of Scientific Instruments* **1971,** *42* (6), 868-871.
(70) Yang, A. H.; Moore, S. D.; Schmidt, B. S., et al., Optical manipulation of nanoparticles and biomolecules in sub-wavelength slot waveguides. *Nature* **2009,** *457* (7225), 71-75.
(71) Cohen, A. E.; Moerner, W., Suppressing Brownian motion of individual biomolecules in solution. *Proceedings of the National Academy of Sciences of the United States of America* **2006,** *103* (12), 4362-4365.
(72) Wang, Q.; Moerner, W., Single-molecule motions enable direct visualization of biomolecular interactions in solution. *Nature Methods* **2014,** *11* (5), 555-558.
(73) Toomre, D.; Bewersdorf, J., A new wave of cellular imaging. *Annual Review of Cell and Developmental Biology* **2010,** *26*, 285-314.
(74) Betzig, E.; Patterson, G. H.; Sougrat, R., et al., Imaging intracellular fluorescent proteins at nanometer resolution. *Science* **2006,** *313* (5793), 1642-1645.
(75) Rust, M. J.; Bates, M.; Zhuang, X., Sub-diffraction-limit imaging by stochastic optical reconstruction microscopy (STORM). *Nature Methods* **2006,** *3* (10), 793-796.
(76) Hess, S. T.; Girirajan, T. P.; Mason, M. D., Ultra-high resolution imaging by fluorescence photoactivation localization microscopy. *Biophysical Journal* **2006,** *91* (11), 4258-4272.
(77) Heilemann, M.; Van De Linde, S.; Schüttpelz, M., et al., Subdiffraction‐resolution fluorescence imaging with conventional fluorescent probes. *Angewandte Chemie International Edition* **2008,** *47* (33), 6172-6176.
(78) Jaqaman, K.; Loerke, D.; Mettlen, M., et al., Robust single-particle tracking in live-cell time-lapse sequences. *Nature Methods* **2008,** *5* (8), 695-702.
(79) Chenouard, N.; Smal, I.; De Chaumont, F., et al., Objective comparison of particle tracking methods. *Nature Methods* **2014,** *11* (3), 281-289.
(80) Meijering, E.; Smal, I.; Danuser, G., Tracking in molecular bioimaging. *IEEE Signal Processing Magazine* **2006,** *23* (3), 46-53.

(81) Kalaidzidis, Y., Intracellular objects tracking. *European Journal of Cell Biology* **2007,** *86* (9), 569-578.
(82) Cheezum, M. K.; Walker, W. F.; Guilford, W. H., Quantitative comparison of algorithms for tracking single fluorescent particles. *Biophysical Journal* **2001,** *81* (4), 2378-2388.
(83) Manley, S.; Gillette, J. M.; Patterson, G. H., et al., High-density mapping of single-molecule trajectories with photoactivated localization microscopy. *Nature Methods* **2008,** *5* (2), 155-157.
(84) Ewers, H.; Smith, A. E.; Sbalzarini, I. F., et al., Single-particle tracking of murine polyoma virus-like particles on live cells and artificial membranes. *Proceedings of the National Academy of Sciences of the United States of America* **2005,** *102* (42), 15110-15115.
(85) Ott, M.; Shai, Y.; Haran, G., Single-particle tracking reveals switching of the HIV fusion peptide between two diffusive modes in membranes. *The Journal of Physical Chemistry B* **2013,** *117* (42), 13308-13321.
(86) English, B. P.; Hauryliuk, V.; Sanamrad, A., et al., Single-molecule investigations of the stringent response machinery in living bacterial cells. *Proceedings of the National Academy of Sciences* **2011,** *108* (31), E365-E373.
(87) Shcherbakova, I.; Hoskins, A. A.; Friedman, L. J., et al., Alternative spliceosome assembly pathways revealed by single-molecule fluorescence microscopy. *Cell Reports* **2013,** *5* (1), 151-165.
(88) Crawford, D. J.; Hoskins, A. A.; Friedman, L. J., et al., Visualizing the splicing of single pre-mRNA molecules in whole cell extract. *RNA* **2008,** *14* (1), 170-179.
(89) Crawford, D. J.; Hoskins, A. A.; Friedman, L. J., et al., Single-molecule colocalization FRET evidence that spliceosome activation precedes stable approach of 5′ splice site and branch site. *Proceedings of the National Academy of Sciences* **2013,** *110* (17), 6783-6788.
(90) Chen, B.-C.; Legant, W. R.; Wang, K., et al., Lattice light-sheet microscopy: Imaging molecules to embryos at high spatiotemporal resolution. *Science* **2014,** *346* (6208), 1257998.
(91) Huang, B.; Jones, S. A.; Brandenburg, B., et al., Whole-cell 3D STORM reveals interactions between cellular structures with nanometer-scale resolution. *Nature Methods* **2008,** *5* (12), 1047-1052.
(92) Liu, S.; Kromann, E. B.; Krueger, W. D., et al., Three dimensional single molecule localization using a phase retrieved pupil function. *Optics Express* **2013,** *21* (24), 29462-29487.
(93) Bosse, J. B.; Hogue, I. B.; Feric, M., et al., Remodeling nuclear architecture allows efficient transport of herpesvirus capsids by diffusion. *Proceedings of the National Academy of Sciences* **2015,** *112* (42), E5725-E5733.
(94) Gebhardt, J. C. M.; Suter, D. M.; Roy, R., et al., Single-molecule imaging of transcription factor binding to DNA in live mammalian cells. *Nature Methods* **2013,** *10* (5), 421-426.

(95) Huisken, J.; Swoger, J.; Del Bene, F., et al., Optical sectioning deep inside live embryos by selective plane illumination microscopy. *Science* **2004,** *305* (5686), 1007-1009.
(96) Greger, K.; Swoger, J.; Stelzer, E., Basic building units and properties of a fluorescence single plane illumination microscope. *Review of Scientific Instruments* **2007,** *78* (2), 023705.
(97) Zanacchi, F. C.; Lavagnino, Z.; Donnorso, M. P., et al., Live-cell 3D super-resolution imaging in thick biological samples. *Nature Methods* **2011,** *8* (12), 1047-1049.
(98) Friedrich, M.; Nozadze, R.; Gan, Q., et al., Detection of single quantum dots in model organisms with sheet illumination microscopy. *Biochemical and Biophysical Research Communications* **2009,** *390* (3), 722-727.
(99) Tomer, R.; Khairy, K.; Amat, F., et al., Quantitative high-speed imaging of entire developing embryos with simultaneous multiview light-sheet microscopy. *Nature Methods* **2012,** *9* (7), 755-763.
(100) Keller, P. J.; Schmidt, A. D.; Wittbrodt, J., et al., Reconstruction of zebrafish early embryonic development by scanned light sheet microscopy. *Science* **2008,** *322* (5904), 1065-1069.
(101) Keller, P. J.; Schmidt, A. D.; Santella, A., et al., Fast, high-contrast imaging of animal development with scanned light sheet-based structured-illumination microscopy. *Nature Methods* **2010,** *7* (8), 637-642.
(102) Saleh, B. E.; Teich, M. C.; Saleh, B. E., *Fundamentals of photonics*. Wiley New York: 1991; Vol. 22.
(103) Gräf, R.; Rietdorf, J.; Zimmermann, T., Live cell spinning disk microscopy. In *Microscopy Techniques*, Springer: 2005; pp 57-75.
(104) Stelzer, E. H., Light-sheet fluorescence microscopy for quantitative biology. *Nature Methods* **2015,** *12* (1), 23-28.
(105) Galland, R.; Grenci, G.; Aravind, A., et al., 3D high-and super-resolution imaging using single-objective SPIM. *Nature Methods* **2015,** *12* (7), 641-644.
(106) Holtzer, L.; Meckel, T.; Schmidt, T., Nanometric three-dimensional tracking of individual quantum dots in cells. *Applied Physics Letters* **2007,** *90* (5), 053902.
(107) Ram, S.; Chao, J.; Prabhat, P., et al. In *A novel approach to determining the three-dimensional location of microscopic objects with applications to 3D particle tracking*, Biomedical Optics (BiOS) 2007, International Society for Optics and Photonics: 2007; pp 64430D-64430D-7.
(108) Prabhat, P.; Ram, S.; Ward, E. S., et al., Simultaneous imaging of different focal planes in fluorescence microscopy for the study of cellular dynamics in three dimensions. *IEEE transactions on nanobioscience* **2004,** *3* (4), 237-242.
(109) Abrahamsson, S.; Chen, J.; Hajj, B., et al., Fast multicolor 3D imaging using aberration-corrected multifocus microscopy. *Nature Methods* **2013,** *10* (1), 60-63.
(110) Chen, J.; Zhang, Z.; Li, L., et al., Single-molecule dynamics of enhanceosome assembly in embryonic stem cells. *Cell* **2014,** *156* (6), 1274-1285.
(111) Smith, C. S.; Preibisch, S.; Joseph, A., et al., Nuclear accessibility of β-actin mRNA is measured by 3D single-molecule real-time tracking. *J Cell Biol* **2015,** *209* (4), 609-619.

(112) Knight, S. C.; Xie, L.; Deng, W., et al., Dynamics of CRISPR-Cas9 genome interrogation in living cells. *Science* **2015,** *350* (6262), 823-826.
(113) Wisniewski, J.; Hajj, B.; Chen, J., et al., Imaging the fate of histone Cse4 reveals de novo replacement in S phase and subsequent stable residence at centromeres. *Elife* **2014,** *3*, e02203.
(114) Hajj, B.; Wisniewski, J.; El Beheiry, M., et al., Whole-cell, multicolor superresolution imaging using volumetric multifocus microscopy. *Proceedings of the National Academy of Sciences* **2014,** *111* (49), 17480-17485.
(115) Hell, S. W.; Lindek, S.; Stelzer, E. H., Enhancing the axial resolution in far-field light microscopy: two-photon 4Pi confocal fluorescence microscopy. *Journal of Modern Optics* **1994,** *41* (4).
(116) Ito, S.; Taga, Y.; Hiratsuka, K., et al., Restricted diffusion of guest molecules in polymer thin films on solid substrates as revealed by three-dimensional single-molecule tracking. *Chemical Communications* **2015,** *51* (72), 13756-13759.
(117) Spille, J.-H.; Kaminski, T. P.; Scherer, K., et al., Direct observation of mobility state transitions in RNA trajectories by sensitive single molecule feedback tracking. *Nucleic Acids Research* **2014**, gku1194.
(118) Lien, C.-H.; Lin, C.-Y.; Chen, S.-J., et al., Dynamic particle tracking via temporal focusing multiphoton microscopy with astigmatism imaging. *Optics Express* **2014,** *22* (22), 27290-27299.
(119) Izeddin, I.; El Beheiry, M.; Andilla, J., et al., PSF shaping using adaptive optics for three-dimensional single-molecule super-resolution imaging and tracking. *Optics Express* **2012,** *20* (5), 4957-4967.
(120) Jones, S. A.; Shim, S.-H.; He, J., et al., Fast, three-dimensional super-resolution imaging of live cells. *Nature Methods* **2011,** *8* (6), 499-505.
(121) Lew, M. D.; Lee, S. F.; Badieirostami, M., et al., Corkscrew point spread function for far-field three-dimensional nanoscale localization of pointlike objects. *Optics Letters* **2011,** *36* (2), 202-204.
(122) Backer, A. S.; Backlund, M. P.; von Diezmann, A. R., et al., A bisected pupil for studying single-molecule orientational dynamics and its application to three-dimensional super-resolution microscopy. *Applied Physics Letters* **2014,** *104* (19), 193701.
(123) Thompson, M. A.; Lew, M. D.; Badieirostami, M., et al., Localizing and tracking single nanoscale emitters in three dimensions with high spatiotemporal resolution using a double-helix point spread function. *Nano Letters* **2009,** *10* (1), 211-218.
(124) Backlund, M. P.; Lew, M. D.; Backer, A. S., et al., Simultaneous, accurate measurement of the 3D position and orientation of single molecules. *Proceedings of the National Academy of Sciences* **2012,** *109* (47), 19087-19092.
(125) Shechtman, Y.; Sahl, S. J.; Backer, A. S., et al., Optimal point spread function design for 3D imaging. *Physical Review Letters* **2014,** *113* (13), 133902.
(126) Ghosh, S.; Preza, C., Characterization of a three-dimensional double-helix point-spread function for fluorescence microscopy in the presence of spherical aberration. *Journal of Biomedical Optics* **2013,** *18* (3), 036010-036010.

(127) Lakadamyali, M.; Rust, M. J.; Babcock, H. P., et al., Visualizing infection of individual influenza viruses. *Proceedings of the National Academy of Sciences* **2003,** *100* (16), 9280-9285.
(128) Courty, S.; Luccardini, C.; Bellaiche, Y., et al., Tracking individual kinesin motors in living cells using single quantum-dot imaging. *Nano Letters* **2006,** *6* (7), 1491-1495.
(129) Izeddin, I.; Récamier, V.; Bosanac, L., et al., Single-molecule tracking in live cells reveals distinct target-search strategies of transcription factors in the nucleus. *Elife* **2014,** *3*, e02230.
(130) Saxton, M. J.; Jacobson, K., Single-particle tracking: applications to membrane dynamics. *Annual Review of Biophysics and Biomolecular Structure* **1997,** *26* (1), 373-399.
(131) Berglund, A. J.; Mabuchi, H., Performance bounds on single-particle tracking by fluorescence modulation. *Applied Physics B: Lasers and Optics* **2006,** *83* (1), 127-133.
(132) Annibale, P.; Dvornikov, A.; Gratton, E., Electrically tunable lens speeds up 3D orbital tracking. *Biomedical Optics Express* **2015,** *6* (6), 2181-2190.
(133) Cang, H.; Xu, C. S.; Montiel, D., et al., Guiding a confocal microscope by single fluorescent nanoparticles. *Optics Letters* **2007,** *32* (18), 2729-2731.
(134) Han, J. J.; Kiss, C.; Bradbury, A. R., et al., Time-resolved, confocal single-molecule tracking of individual organic dyes and fluorescent proteins in three dimensions. *ACS Nano* **2012,** *6* (10), 8922-8932.
(135) Wells, N. P.; Lessard, G. A.; Werner, J. H., Confocal, three-dimensional tracking of individual quantum dots in high-background environments. *Analytical Chemistry* **2008,** *80* (24), 9830-9834.
(136) DeVore, M. S.; Stich, D. G.; Keller, A. M., et al. In *Three dimensional time-gated tracking of non-blinking quantum dots in live cells*, SPIE BiOS, International Society for Optics and Photonics: 2015; pp 933812-933812-15.
(137) Juette, M. F.; Gould, T. J.; Lessard, M. D., et al., Three-dimensional sub–100 nm resolution fluorescence microscopy of thick samples. *Nature Methods* **2008,** *5* (6), 527-529.
(138) Campos, L. A.; Liu, J.; Wang, X., et al., A photoprotection strategy for microsecond-resolution single-molecule fluorescence spectroscopy. *Nature Methods* **2011,** *8* (2), 143-146.
(139) Richards, B.; Wolf, E. In *Electromagnetic diffraction in optical systems. II. Structure of the image field in an aplanatic system*, Proceedings of the Royal Society of London A: Mathematical, Physical and Engineering Sciences, The Royal Society: 1959; pp 358-379.
(140) Qian, H.; Elson, E. L., Analysis of confocal laser-microscope optics for 3-D fluorescence correlation spectroscopy. *Applied Optics* **1991,** *30* (10), 1185-1195.
(141) Berg, H. C., *Random walks in biology*. Princeton University Press: 1993.
(142) Widengren, J.; Mets, U.; Rigler, R., Fluorescence correlation spectroscopy of triplet states in solution: a theoretical and experimental study. *The Journal of Physical Chemistry* **1995,** *99* (36), 13368-13379.

(143) Mortensen, K. I.; Churchman, L. S.; Spudich, J. A., et al., Optimized localization analysis for single-molecule tracking and super-resolution microscopy. *Nature Methods* **2010,** *7* (5), 377-381.
(144) Hell, S.; Stelzer, E. H., Properties of a 4Pi confocal fluorescence microscope. *JOSA A* **1992,** *9* (12), 2159-2166.
(145) Schmidt, R.; Wurm, C. A.; Jakobs, S., et al., Spherical nanosized focal spot unravels the interior of cells. *Nature Methods* **2008,** *5* (6), 539-544.
(146) Cheng, N.-S., Formula for the viscosity of a glycerol-water mixture. *Industrial & Engineering Chemistry Research* **2008,** *47* (9), 3285-3288.
(147) Michalet, X., Mean square displacement analysis of single-particle trajectories with localization error: Brownian motion in an isotropic medium. *Physical Review E* **2010,** *82* (4), 041914.
(148) Saxton, M. J., Anomalous diffusion due to obstacles: a Monte Carlo study. *Biophysical Journal* **1994,** *66* (2 Pt 1), 394.
(149) Michalet, X.; Berglund, A. J., Optimal diffusion coefficient estimation in single-particle tracking. *Physical Review E* **2012,** *85* (6), 061916.
(150) Lounis, B.; Moerner, W. E., Single photons on demand from a single molecule at room temperature. *Nature* **2000,** *407* (6803), 491-493.
(151) Lounis, B.; Bechtel, H.; Gerion, D., et al., Photon antibunching in single CdSe/ZnS quantum dot fluorescence. *Chemical Physics Letters* **2000,** *329* (5), 399-404.
(152) Zhang, T.; Lu, G.; Shen, H., et al., Photoluminescence of a single complex plasmonic nanoparticle. *Scientific reports* **2014,** *4*, 3867.
(153) Yin, P.; Choi, H. M.; Calvert, C. R., et al., Programming biomolecular self-assembly pathways. *Nature* **2008,** *451* (7176), 318-322.
(154) Rothemund, P. W., Folding DNA to create nanoscale shapes and patterns. *Nature* **2006,** *440* (7082), 297-302.
(155) Fu, J.; Yan, H., Controlled drug release by a nanorobot. *Nature Biotechnology* **2012,** *30* (5), 407.
(156) Liang, L.; Li, J.; Li, Q., et al., Single‐Particle Tracking and Modulation of Cell Entry Pathways of a Tetrahedral DNA Nanostructure in Live Cells. *Angewandte Chemie International Edition* **2014,** *53* (30), 7745-7750.
(157) Wang, Q.; Moerner, W., An Adaptive Anti-Brownian ELectrokinetic trap with real-time information on single-molecule diffusivity and mobility. *ACS Nano* **2011,** *5* (7), 5792-5799.
(158) Sorokin, V.; Gladchenko, G.; Valeev, V., et al., Effect of salt and organic solvents on DNA thermal stability and structure. *Journal of Molecular Structure* **1997,** *408*, 237-240.
(159) Gu, X.-B.; Nakano, S.-i.; Sugimoto, N. In *The effect of the structure of cosolutes on the DNA duplex formation*, Nucleic Acids Symposium Series, Oxford Univ Press: 2006; pp 205-206.
(160) Bonner, G.; Klibanov, A. M., Structural stability of DNA in nonaqueous solvents. *Biotechnology and Bioengineering* **2000,** *68* (3), 339-344.

(161) Wetmur, J. G., Acceleration of DNA renaturation rates. *Biopolymers* **1975,** *14* (12), 2517-2524.
(162) Kim, J.-Y.; Kim, C.; Lee, N. K., Real-time submillisecond single-molecule FRET dynamics of freely diffusing molecules with liposome tethering. *Nature Communications* **2015,** *6*.
(163) Kim, J.-Y.; Choi, B.-K.; Choi, M.-G., et al., Solution single-vesicle assay reveals PIP2 ‐ mediated sequential actions of synaptotagmin-1 on SNAREs. *The EMBO Journal* **2012,** *31* (9), 2144-2155.
(164) Rasnik, I.; McKinney, S. A.; Ha, T., Nonblinking and long-lasting single-molecule fluorescence imaging. *Nature Methods* **2006,** *3* (11), 891.
(165) Aitken, C. E.; Marshall, R. A.; Puglisi, J. D., An oxygen scavenging system for improvement of dye stability in single-molecule fluorescence experiments. *Biophysical Journal* **2008,** *94* (5), 1826-1835.
(166) Sprague, B. L.; McNally, J. G., FRAP analysis of binding: proper and fitting. *Trends in Cell Biology* **2005,** *15* (2), 84-91.
(167) Sprague, B. L.; Pego, R. L.; Stavreva, D. A., et al., Analysis of binding reactions by fluorescence recovery after photobleaching. *Biophysical Journal* **2004,** *86* (6), 3473-3495.
(168) Medina, M. A.; Schwille, P., Fluorescence correlation spectroscopy for the detection and study of single molecules in biology. *Bioessays* **2002,** *24* (8), 758-764.
(169) Patel, R. C.; Kumar, U.; Lamb, D. C., et al., Ligand binding to somatostatin receptors induces receptor-specific oligomer formation in live cells. *Proceedings of the National Academy of Sciences* **2002,** *99* (5), 3294-3299.
(170) Amediek, A.; Haustein, E.; Scherfeld, D., et al., Scanning Dual ‐ Color Cross ‐ Correlation Analysis for Dynamic Co ‐ Localization Studies of Immobile Molecules. *Single Molecules* **2002,** *3* (4), 201-210.
(171) Heinze, K. G.; Rarbach, M.; Jahnz, M., et al., Two-photon fluorescence coincidence analysis: rapid measurements of enzyme kinetics. *Biophysical Journal* **2002,** *83* (3), 1671-1681.
(172) Baudendistel, N.; Müller, G.; Waldeck, W., et al., Two ‐ Hybrid Fluorescence Cross ‐ Correlation Spectroscopy Detects Protein ‐ Protein Interactions In Vivo. *ChemPhysChem* **2005,** *6* (5), 984-990.
(173) Weidemann, T.; Wachsmuth, M.; Tewes, M., et al., Analysis of ligand binding by two-colour fluorescence cross-correlation spectroscopy. *Single Molecules* **2002,** *3* (1), 49-61.
(174) Manzo, C.; Garcia-Parajo, M. F., A review of progress in single particle tracking: from methods to biophysical insights. *Reports on Progress in Physics* **2015,** *78* (12), 124601.
(175) Patterson, G. H.; Piston, D. W., Photobleaching in two-photon excitation microscopy. *Biophysical Journal* **2000,** *78* (4), 2159-2162.

(176) Dittrich, P.; Schwille, P., Photobleaching and stabilization of. fluorophores used for single-molecule analysis. with one-and two-photon excitation. *Applied Physics B: Lasers and Optics* **2001,** *73* (8), 829-837.
(177) Thiel, A. J.; Frutos, A. G.; Jordan, C. E., et al., In situ surface plasmon resonance imaging detection of DNA hybridization to oligonucleotide arrays on gold surfaces. *Analytical Chemistry* **1997,** *69* (24), 4948-4956.
(178) Nelson, B. P.; Grimsrud, T. E.; Liles, M. R., et al., Surface plasmon resonance imaging measurements of DNA and RNA hybridization adsorption onto DNA microarrays. *Analytical Chemistry* **2001,** *73* (1), 1-7.
(179) Walter, N. G.; Burke, J. M., Real-time monitoring of hairpin ribozyme kinetics through base-specific quenching of fluorescein-labeled substrates. *RNA* **1997,** *3* (4), 392-404.
(180) Tsourkas, A.; Behlke, M. A.; Rose, S. D., et al., Hybridization kinetics and thermodynamics of molecular beacons. *Nucleic Acids Research* **2003,** *31* (4), 1319-1330.
(181) Zhang, D. Y.; Winfree, E., Control of DNA strand displacement kinetics using toehold exchange. *Journal of the American Chemical Society* **2009,** *131* (47), 17303-17314.
(182) Hilbers, C.; Haasnoot, C.; De Bruin, S., et al., Hairpin formation in synthetic oligonucleotides. *Biochimie* **1985,** *67* (7-8), 685-695.
(183) Ambrose, W. P.; Goodwin, P. M.; Jett, J. H., et al., Single molecule fluorescence spectroscopy at ambient temperature. *Chemical Reviews* **1999,** *99* (10), 2929-2956.
(184) Park, H. Y.; Lim, H.; Yoon, Y. J., et al., Visualization of dynamics of single endogenous mRNA labeled in live mouse. *Science* **2014,** *343* (6169), 422-424.
(185) Suzuki, K. G.; Kasai, R. S.; Hirosawa, K. M., et al., Transient GPI-anchored protein homodimers are units for raft organization and function. *Nature Chemical Biology* **2012,** *8* (9), 774-783.
(186) Trabesinger, W.; Schütz, G. J.; Gruber, H. J., et al., Detection of individual oligonucleotide pairing by single-molecule microscopy. *Analytical Chemistry* **1999,** *71* (1), 279-283.
(187) Nagata, K. O.; Nakada, C.; Kasai, R. S., et al., ABCA1 dimer–monomer interconversion during HDL generation revealed by single-molecule imaging. *Proceedings of the National Academy of Sciences* **2013,** *110* (13), 5034-5039.
(188) Suzuki, K. G.; Fujiwara, T. K.; Sanematsu, F., et al., GPI-anchored receptor clusters transiently recruit Lyn and Gα for temporary cluster immobilization and Lyn activation: single-molecule tracking study 1. *The Journal of Cell Biology* **2007,** *177* (4), 717-730.
(189) Low-Nam, S. T.; Lidke, K. A.; Cutler, P. J., et al., ErbB1 dimerization is promoted by domain co-confinement and stabilized by ligand binding. *Nature Structural & Molecular Biology* **2011,** *18* (11), 1244-1249.
(190) Suzuki, K. G.; Fujiwara, T. K.; Edidin, M., et al., Dynamic recruitment of phospholipase Cγ at transiently immobilized GPI-anchored receptor clusters induces IP3–Ca2+ signaling: single-molecule tracking study 2. *The Journal of Cell Biology* **2007,** *177* (4), 731-742.

(191) Murakoshi, H.; Iino, R.; Kobayashi, T., et al., Single-molecule imaging analysis of Ras activation in living cells. *Proceedings of the National Academy of Sciences of the United States of America* **2004,** *101* (19), 7317-7322.
(192) Groeneweg, F. L.; van Royen, M. E.; Fenz, S., et al., Quantitation of glucocorticoid receptor DNA-binding dynamics by single-molecule microscopy and FRAP. *PLoS One* **2014,** *9* (3), e90532.
(193) Semrau, S.; Schmidt, T., Particle image correlation spectroscopy (PICS): retrieving nanometer-scale correlations from high-density single-molecule position data. *Biophysical Journal* **2007,** *92* (2), 613-621.
(194) Chung, I.; Akita, R.; Vandlen, R., et al., Spatial control of EGF receptor activation by reversible dimerization on living cells. *Nature* **2010,** *464* (7289), 783-787.
(195) Milenkovic, L.; Weiss, L. E.; Yoon, J., et al., Single-molecule imaging of Hedgehog pathway protein Smoothened in primary cilia reveals binding events regulated by Patched1. *Proceedings of the National Academy of Sciences* **2015,** *112* (27), 8320-8325.
(196) Stracy, M.; Lesterlin, C.; de Leon, F. G., et al., Live-cell superresolution microscopy reveals the organization of RNA polymerase in the bacterial nucleoid. *Proceedings of the National Academy of Sciences* **2015,** *112* (32), E4390-E4399.
(197) Morisaki, T.; Müller, W. G.; Golob, N., et al., Single-molecule analysis of transcription factor binding at transcription sites in live cells. *Nature Communications* **2014,** *5*.
(198) Persson, F.; Lindén, M.; Unoson, C., et al., Extracting intracellular diffusive states and transition rates from single-molecule tracking data. *Nature Methods* **2013,** *10* (3), 265-269.
(199) Meseth, U.; Wohland, T.; Rigler, R., et al., Resolution of fluorescence correlation measurements. *Biophysical Journal* **1999,** *76* (3), 1619-1631.
(200) Müller, J. D.; Chen, Y.; Gratton, E., Resolving heterogeneity on the single molecular level with the photon-counting histogram. *Biophysical Journal* **2000,** *78* (1), 474-486.
(201) Savin, T.; Doyle, P. S., Static and dynamic errors in particle tracking microrheology. *Biophysical Journal* **2005,** *88* (1), 623-638.
(202) Sahl, S. J.; Leutenegger, M.; Hell, S. W., et al., High‐Resolution Tracking of Single‐Molecule Diffusion in Membranes by Confocalized and Spatially Differentiated Fluorescence Photon Stream Recording. *ChemPhysChem* **2014,** *15* (4), 771-783.
(203) Sunney Xie, X., Single-molecule approach to dispersed kinetics and dynamic disorder: Probing conformational fluctuation and enzymatic dynamics. *The Journal of Chemical Physics* **2002,** *117* (24), 11024-11032.
(204) Lu, H. P.; Xie, S. X., Single-molecule spectral fluctuations at room temperature. *Nature* **1997,** *385* (6612), 143.
(205) Welch, P., The use of fast Fourier transform for the estimation of power spectra: a method based on time averaging over short, modified periodograms. *IEEE Transactions on audio and electroacoustics* **1967,** *15* (2), 70-73.

(206) Das, R.; Cairo, C. W.; Coombs, D., A hidden Markov model for single particle tracks quantifies dynamic interactions between LFA-1 and the actin cytoskeleton. *PLOS Computational Biology* **2009,** *5* (11), e1000556.
(207) Zander, C.; Brand, L.; Eggeling, C., et al. In *Single-molecule detection by two-photon excitation of fluorescence*, BiOS'97, Part of Photonics West, International Society for Optics and Photonics: 1997; pp 552-558.
(208) Brand, L.; Eggeling, C.; Zander, C., et al., Single-molecule identification of Coumarin-120 by time-resolved fluorescence detection: Comparison of one-and two-photon excitation in solution. *The Journal of Physical Chemistry A* **1997,** *101* (24), 4313-4321.
(209) van de Meent, J.-W.; Bronson, J. E.; Wiggins, C. H., et al., Empirical Bayes methods enable advanced population-level analyses of single-molecule FRET experiments. *Biophysical Journal* **2014,** *106* (6), 1327-1337.
(210) Suhling, K.; Siegel, J.; Phillips, D., et al., Imaging the environment of green fluorescent protein. *Biophysical Journal* **2002,** *83* (6), 3589-3595.
(211) Tregidgo, C.; Levitt, J. A.; Suhling, K., Effect of refractive index on the fluorescence lifetime of green fluorescent protein. *Journal of Biomedical Optics* **2008,** *13* (3), 031218-031218-8.
(212) Hannestad, J. K.; Brune, R.; Czolkos, I., et al., Kinetics of diffusion-mediated DNA hybridization in lipid monolayer films determined by single-molecule fluorescence spectroscopy. *ACS Nano* **2012,** *7* (1), 308-315.
(213) Dupuis, N. F.; Holmstrom, E. D.; Nesbitt, D. J., Single-molecule kinetics reveal cation-promoted DNA duplex formation through ordering of single-stranded helices. *Biophysical Journal* **2013,** *105* (3), 756-766.
(214) Peterson, E. M.; Manhart, M. W.; Harris, J. M., Single-Molecule Fluorescence Imaging of Interfacial DNA Hybridization Kinetics at Selective Capture Surfaces. *Analytical Chemistry* **2016,** *88* (2), 1345-1354.
(215) Jungmann, R.; Steinhauer, C.; Scheible, M., et al., Single-molecule kinetics and super-resolution microscopy by fluorescence imaging of transient binding on DNA origami. *Nano Letters* **2010,** *10* (11), 4756-4761.
(216) McKinney, S. A.; Joo, C.; Ha, T., Analysis of single-molecule FRET trajectories using hidden Markov modeling. *Biophysical Journal* **2006,** *91* (5), 1941-1951.
(217) Bronson, J. E.; Fei, J.; Hofman, J. M., et al., Learning rates and states from biophysical time series: a Bayesian approach to model selection and single-molecule FRET data. *Biophysical Journal* **2009,** *97* (12), 3196-3205.
(218) Nicolai, C.; Sachs, F., Solving ion channel kinetics with the QuB software. *Biophysical Reviews and Letters* **2013,** *8* (03n04), 191-211.
(219) Schildkraut, C.; Lifson, S., Dependence of the melting temperature of DNA on salt concentration. *Biopolymers* **1965,** *3* (2), 195-208.
(220) Tan, Z.-J.; Chen, S.-J., Nucleic acid helix stability: effects of salt concentration, cation valence and size, and chain length. *Biophysical Journal* **2006,** *90* (4), 1175-1190.

(221) Hwang, H.; Kim, H.; Myong, S., Protein induced fluorescence enhancement as a single molecule assay with short distance sensitivity. *Proceedings of the National Academy of Sciences* **2011,** *108* (18), 7414-7418.
(222) Sanborn, M. E.; Connolly, B. K.; Gurunathan, K., et al., Fluorescence properties and photophysics of the sulfoindocyanine Cy3 linked covalently to DNA. *The Journal of Physical Chemistry B* **2007,** *111* (37), 11064-11074.
(223) Aramendia, P. F.; Negri, R. M.; Sanroman, E., Temperature-dependence of fluorescence and photoisomerization in symmetrical carbocyanines-influence of medium viscosity and molecular-structure. *Journal of Physical Chemistry* **1994,** *98* (12), 3165-3173.
(224) Morten, M. J.; Peregrina, J. R.; Figueira-Gonzalez, M., et al., Binding dynamics of a monomeric SSB protein to DNA: a single-molecule multi-process approach. *Nucleic Acids Research* **2015,** *43* (22), 10907-10924.
(225) Widengren, J.; Kudryavtsev, V.; Antonik, M., et al., Single-molecule detection and identification of multiple species by multiparameter fluorescence detection. *Analytical Chemistry* **2006,** *78* (6), 2039-2050.
(226) Berezin, M. Y.; Achilefu, S., Fluorescence lifetime measurements and biological imaging. *Chemical Reviews* **2010,** *110* (5), 2641-2684.
(227) Becker, W., Fluorescence lifetime imaging–techniques and applications. *Journal of Microscopy* **2012,** *247* (2), 119-136.
(228) Werner, J. H.; Cai, H.; Goodwin, P. M., et al. In *Current status of DNA sequencing by single molecule detection*, BiOS'99 International Biomedical Optics Symposium, International Society for Optics and Photonics: 1999; pp 355-366.
(229) Van Orden, A.; Machara, N. P.; Goodwin, P. M., et al., Single-molecule identification in flowing sample streams by fluorescence burst size and intraburst fluorescence decay rate. *Analytical Chemistry* **1998,** *70* (7), 1444-1451.
(230) Enderlein, J.; Goodwin, P. M.; Van Orden, A., et al., A maximum likelihood estimator to distinguish single molecules by their fluorescence decays. *Chemical Physics Letters* **1997,** *270* (5-6), 464-470.
(231) Enderlein, J.; Sauer, M., Optimal algorithm for single-molecule identification with time-correlated single-photon counting. *The Journal of Physical Chemistry A* **2001,** *105* (1), 48-53.
(232) Zander, C.; Sauer, M.; Drexhage, K., et al., Detection and characterization of single molecules in aqueous solution. *Applied Physics B: Lasers and Optics* **1996,** *63* (5), 517-523.
(233) Fries, J. R.; Brand, L.; Eggeling, C., et al., Quantitative identification of different single molecules by selective time-resolved confocal fluorescence spectroscopy. *The Journal of Physical Chemistry A* **1998,** *102* (33), 6601-6613.
(234) Braslavsky, I.; Hebert, B.; Kartalov, E., et al., Sequence information can be obtained from single DNA molecules. *Proceedings of the National Academy of Sciences* **2003,** *100* (7), 3960-3964.
(235) Soper, S. A.; Davis, L. M.; Shera, E. B., Detection and identification of single molecules in solution. *JOSA B* **1992,** *9* (10), 1761-1769.

(236) Shi, C.; Eshleman, S. H.; Jones, D., et al., LigAmp for sensitive detection of single-nucleotide differences. *Nature Methods* **2004,** *1* (2), 141-147.
(237) Hall, P.; Selinger, B., Better estimates of exponential decay parameters. *The Journal of Physical Chemistry* **1981,** *85* (20), 2941-2946.